

LONG WAVELENGTH GaInNAs AND GaInNAsSb LASERS ON GaAs

A DISSERTATION

SUBMITTED TO THE DEPARTMENT OF ELECTRICAL ENGINEERING

AND THE COMMITTEE ON GRADUATE STUDIES

OF STANFORD UNIVERSITY

IN PARTIAL FULFILLMENT OF THE REQUIREMENTS

FOR THE DEGREE OF

DOCTOR OF PHILOSOPHY

Wonill Ha

December 2002

i



□ Copyright by Wonill Ha 2003  
All Rights Reserved

I certify that I have read this dissertation and that in my opinion it is fully adequate, in scope and quality, as dissertation for the degree of Doctor of Philosophy.

---

James Harris  
(Principal Advisor)

I certify that I have read this dissertation and that in my opinion it is fully adequate, in scope and quality, as dissertation for the degree of Doctor of Philosophy.

---

Olav Solgaard  
(Associate Advisor)

I certify that I have read this dissertation and that in my opinion it is fully adequate, in scope and quality, as dissertation for the degree of Doctor of Philosophy.

---

Glenn Solomon

Approved for the University Committee on Graduate Studies

---

## ABSTRACT

The boom in fiber optic communications has created a high demand for lower cost lasers in the 1.3-1.6  $\mu\text{m}$  wavelength range for both vertical-cavity surface-emitting lasers (VCSELs) and high-power Raman pumps. This has led to the introduction of dilute nitrogen as an alloy constituent into GaInAs to reduce the bandgap sufficiently, resulting in a new long wavelength material grown on GaAs. This new material will provide a new platform for low cost and high-speed directly-modulated lasers that are essential for the rapid expansion of optical wide area networks (WANs), metro area networks (MANs), and local area networks (LANs). The requirements for these lasers are a broad operating temperature range (-10 to 90°C) and moderate output power (~10 mW) in the fundamental mode. There is also a growing interest in higher power lasers at similar wavelengths, as pumps for Raman amplifiers to expand the available bandwidth and increase power budgets. Hitherto, InP-based lasers have provided the sources for all of these applications but suffer shortcomings that greatly hinder their ability to cover the complete 1.3-1.6  $\mu\text{m}$  wavelength range<sup>1</sup>. Research has shown that GaInNAs can be coherently lattice matched to GaAs while providing the proper bandgap energy<sup>2,3,8</sup> for 1.3 ~ 1.6  $\mu\text{m}$  emission. These GaAs-based lasers with dilute N can take advantage of the well-developed GaAs processing techniques and superior distributed Bragg Reflector (DBR) mirror technology for VCSELs<sup>3,34</sup>. Laser diodes with GaInNAs active layers have already shown prospective characteristics, including low threshold current density, high temperature continuous wave (CW) operation, and high characteristic temperature ( $T_0$ ) in the wavelength range of 1.1  $\mu\text{m}$  to 1.3  $\mu\text{m}$ <sup>2,3,8</sup>.

This thesis presents new structures utilizing GaNAs barriers and a new quantum well material, GaInNAsSb, to achieve long-wavelength optical emission in post-annealed material. Unfortunately, this increase is accompanied by a blue-shift in the badgap energy. As a result, the distinct challenge of this material system is to achieve high quality material with sufficiently long wavelength emission. Introduction of nitrogen into

the barriers reduces the blue-shift of luminescence by suppressing nitrogen out-diffusion from the quantum wells and decreasing carrier confinement in the quantum wells.

We utilize antimony, both incorporated into the crystal and used as a surfactant, to enable higher indium incorporation. GaNAs or GaNAsSb barriers also reduce the overall strain of the device layers because high indium mole fraction quantum wells, GaInNAs and GaInNAsSb, are compressively strained and the GaNAs barriers are tensely strained.

The Molecular Beam Epitaxial (MBE) growth and demonstration of high-efficiency long-wavelength multiple quantum well (MQW) GaInNAs(Sb) ridge-waveguide laser diodes using GaNAs(Sb) barriers on GaAs substrate and longer wavelength photoluminescence are described in this work. The wide wavelength range coverage and high output power of GaInNAs and GaInNAsSb lasers grown on GaAs developed in this thesis make these great candidates for both transmitters and optical amplifiers for telecommunications.

## ACKNOWLEDGMENTS

First of all, I would like to deeply thank my Lord for my birth, growing up, and leading me to one of the most prestigious university, Stanford. Without His grace, I will not be here and would not be blessed with all luxurious surroundings I am enjoying now. My special appreciation goes to my father, Young-Soo Ha, and my mother, Jung-Soon Park, who devoted their lives for me. Nothing would have been achieved without their sacrificial deed. My brother, Sang-Yoo Ha, has been my best friend ever since he was born. I will never forget his encouragement and sincere care for me. I also would like to devote this work to my late grandmother, Saeng-I Roh. She was almost a second mother when I was young. Her inspiration and soft care are still remembered in my heart and her portrait is buried deep inside me. My father-in-law, Hak-Suh Koo, deserves great gratitude from me. His diligence and righteousness became my model of life. He showed the discipline by his deeds not by empty dialogue. My mother-in-law, Myung-Sook Yang has always cheered me up and feel alive throughout my graduate life. I had so much fun with my brothers-in-law, Moon-Hoe Koo and Youl-Hoe Koo and the time with them relieved my stress.

My special thanks should go to my advisor, Professor James S. Harris, Jr. He was very supportive during the first phase of my graduate life and helped me get through a most difficult period. He has nourished me economically and intellectually for 5 years at Stanford. I was truly impressed by his instinct on science and his enthusiasm on teaching and research. I benefited from his broad knowledge on almost everything not limited by technology and science. I also thank Professor Olav Solggard and Glenn Solomon for many precious discussions as well as for being my thesis committee. I also would like to extend my gratitude to Professor Umran Inan for chairing my thesis committee.

I cannot pass this section without mentioning all my “academy brothers.” Erji Mao who taught me many necessary processing skills to survive as a electrical engineer, Hong Liu, who had many fruitful discussion, Vijit Sabnis, who introduced me many new technologies, Chien Chung Lin, who I learn the real meaning of patience and endurance,

Vincent Gambin, who sometimes spent more time with me than my wife in the MBE laboratory, Mark Wistey, who showed me what the scientist should be, Seth Bank, who read and corrected all grammatical errors of all papers published including my thesis and became my precious friend, Homan Yuen, who gave lots of advice on material science, Evan Thrush and Rafael Aldaz who shared lots of good memory and useful and un-useful discussion. Other MBE gurus will be certainly remembered; Chris Coldren, Sylvia Spruytte, Thierry Pinguet, Xian Liu, Junxian Fu, Tim Gugov, David Jackrel, Xiaojun Yu, and Qing Tang.

I also want to appreciate for the people in Novlax Inc. for their kind help. Dr. Aram Mooradian, Dr. Alan Lewis, Dr. Glen Carey, Mr. Rene Lujan, Mr. James Peterson, and Mr. Thu Do.

I would like to thank Gail Chun-Creech for her helpful administrative support, which made my life run a lot more smoothly.

My Korean friends should be named too. Dr. Chang-Hoon Choi, Dr. Hyun-Jin Cho, Dr. Kwang-Hoon Oh, Ki-Young Nam, Hyun-Soo Yang, Tae-Young Oh, and Young-Kwan Park. I shared my precious lunch time with these guys and learned a lot of technical and non-technical stuff from these people.

My very special and deep-from-my-heart appreciation goes to my wife, Yun-Hoe Koo. She comforted, boosted, encouraged, and even flattered me throughout my graduate life. She endured small stipends and the bad husband who spends most of the time in the lab. I will do my best to make her happy forever...

## **DEDICATION**

*The author wishes to dedicate this dissertation to his wife, Yunwhe.*

## LIST OF TABLES

<i>Table Number</i>	<i>Page</i>
Table 1: Gigabit Ethernet Standard according to IEEE 802.3z .....	21
Table 2: Comparison of laser materials in the 1.2-1.6 $\mu$ m wavelength range.....	27
Table 3: Properties of nitrogen and arsenic .....	53
Table 4: Properties of nitrides and arsenides .....	53
Table 5: Interaction parameters for various III-V ternary alloy systems .....	58
Table 6: Summary of photoluminescence result from GaInNAs/GaAs, GaInNAs /GaNAs, GaInNAsSb/GaAs, and GaInNAsSb/GaNAsSb structures .....	90
Table 7: Important semiconductor parameters .....	111
Table 8: Binary material properties.....	119
Table 9: Bowing parameters for ternary alloy materials .....	119
Table 10: Growth structure of ridge waveguide emitting lasers.....	124

# LIST OF FIGURES

<i>Figure Number</i>	<i>Page</i>
Figure 1: Bandgap energy vs. lattice constant for materials relevant to telecommunications .....	2
Figure 2: Transmission loss in conventional optical fiber.....	4
Figure 3: Interaction between electrons and photons.....	6
Figure 4: The common semiconductor laser structure .....	7
Figure 5: A semiconductor laser diode structure with mirrors at both ends.....	8
Figure 6: Energy levels in quantum well structure .....	9
Figure 7: Semiconductor optical amplifier .....	11
Figure 8: Erbium doped fiber amplifier diagram .....	13
Figure 9: Physical picture behind Raman scattering .....	15
Figure 10: Raman gain curve versus wavelength offset between pump and source laser .....	16
Figure 11: Schematic of Raman amplifier system .....	16
Figure 12: Mach-Zehnder modulator with LiNbO <sub>3</sub> crystal .....	18
Figure 13: Schematic of photodetector .....	19
Figure 14: Transmission distance versus data transmission speed for various optical communication lasers.....	20
Figure 15: A schematic of VCSEL .....	22
Figure 16: Schematic of MBE growth mechanism.....	32
Figure 17: Schematic of MBE growth chamber and its parts.....	34
Figure 18: Arsenic pressure transition under opening and closing of mechanical valve ..	36
Figure 19: Diagram of the nitrogen plasma source configuration .....	38
Figure 20: Nitrogen, Hydrogen, Oxygen, Carbon, and Boron concentration profile measured by SIMS .....	40
Figure 21: Emission spectrum of the rf plasma .....	41

Figure 22: Illustration of the mechanism for RHEED spot oscillations during growth of a monolayer .....	44
Figure 23: Illustration of the setup to measure surface normal reflectance of a sample post epitaxial growth.....	46
Figure 24: Group III growth rate versus nitrogen concentration .....	55
Figure 25: Miscibility gap calculation of free-standing $\text{GaN}_x\text{As}_{1-x}$ alloy .....	56
Figure 26: Schematic of RTA system for this study .....	64
Figure 27: Room temperature PL of $\text{Ga}_{0.7}\text{In}_{0.3}\text{N}_{0.01}\text{As}_{0.99}/\text{GaAs}$ .....	64
Figure 28: PL peak intensity, wavelength, FWHM dependent on annealing temperature for $\text{Ga}_{0.7}\text{In}_{0.3}\text{N}_{0.015}\text{As}_{0.985}/\text{GaAs}$ .....	66
Figure 29: PL peak intensity increase and peak wavelength blue shift upon annealing for $\text{GaN}_{0.024}\text{As}_{0.976}/\text{GaAs}$ .....	67
Figure 30: SIMS profiles of nitrogen counts for GaInNAs/GaAs for as-grown and annealed sample.....	68
Figure 31: SIMS profiles of indium counts for GaInAs/GaAs for as-grown and annealed sample.....	69
Figure 32: SIMS profiles of nitrogen counts for GaInNAs/GaNAs for as-grown and annealed sample.....	69
Figure 33: PL comparison between GaAs and GaNAs barrier structures.....	70
Figure 34: Schematic of strained structure .....	71
Figure 35: GaNAs air bridge structure .....	71
Figure 36: TEM images of a nine quantum well sample and a higher magnification image of the top quantum well .....	72
Figure 37: PL intensity comparison for different numbers of quantum wells.....	73
Figure 38: Simulation of configurations surrounding nitrogen atom for different indium concentration during growth.....	74
Figure 39: The probable configuration change around nitrogen atom during annealing process.....	75

Figure 40: Super-cell simulation results of the conduction band structure of $\text{Ga}_{1-y}\text{In}_y\text{N}_x\text{As}_{1-x}$ for various nitrogen neighbor environments of the nitrogen center .....	75
Figure 41: PL spectroscopy measurement setup.....	79
Figure 42: Basic theory on band diagram and luminescence .....	81
Figure 43: Spontaneous emission spectrum for direct band semiconductor .....	83
Figure 44: PL sample growth sequence.....	84
Figure 45: Photoluminescence System response .....	86
Figure 46: Typical photoluminescence result dependent on annealing temperature from GaInNAs sample .....	87
Figure 47: PL of various GaInNAs(Sb) samples normalized to the highest 1.3 $\mu\text{m}$ PL intensity from three quantum wells.....	88
Figure 48: Deriving Bragg's Law using the reflection geometry and applying trigonometry .....	92
Figure 49: HRXRD result on GaInNAs/GaNAs and GaInNAsSb/GaNAsSb.....	94
Figure 50: Comparison between HRXRD experimental result and dynamical simulation .....	95
Figure 51: Various signals obtained by the electron irradiation of specimen surface and the signal detection depth .....	96
Figure 52: Schematic diagram of CL spectrometer .....	97
Figure 53: CL measurement result on various samples.....	98
Figure 54: CL spectrum of GaInNAs sample at 4K.....	99
Figure 55: CL on GaInNAs samples .....	99
Figure 56: AFM images of GaInNAs and GaInNAsSb.....	100
Figure 57: Sputtering effects of SIMS.....	101
Figure 58: SIMS spectra on GaInNAsSb sample before and after annealing .....	103
Figure 59: Calculation of square quantum well .....	106
Figure 60: A quantum well with a width $L$ and a finite barrier height $V_0$ .....	107
Figure 61: A graphical solution for the attenuation constant $a$ and wave number $k$ of a quantum well with finite barrier .....	108

Figure 62: The electron density of states for a two-dimensional quantum well structure compared with the three-dimensional density of states.....	110
Figure 63: Schematic conduction band diagram of a strained GaInAs quantum well with GaAs barriers .....	112
Figure 64: Critical thickness vs. In concentration in GaAs/In <sub>x</sub> Ga <sub>1-x</sub> As/GaAs single quantum well .....	114
Figure 65: Absorption measurement from GaN <sub>0.017</sub> As <sub>0.983</sub> and GaN <sub>0.03</sub> As <sub>0.97</sub> .....	116
Figure 66: Photoluminescence result from GaN <sub>0.02</sub> As <sub>0.98</sub> .....	117
Figure 67: Bandgap engineering method of GaInNAs/GaAs.....	121
Figure 68: Ridge waveguide laser structure .....	123
Figure 69: SEM images of ridge waveguide structure .....	126
Figure 70: Optical spectrum of Ga <sub>0.68</sub> In <sub>0.32</sub> N <sub>0.015</sub> As <sub>0.985</sub> /GaAs <sub>0.98</sub> N <sub>0.02</sub> laser .....	128
Figure 71: L-I-V of Ga <sub>0.68</sub> In <sub>0.32</sub> N <sub>0.015</sub> As <sub>0.985</sub> /GaAs <sub>0.98</sub> N <sub>0.02</sub> laser .....	129
Figure 72: Comparison chart on threshold current density vs. emission wavelength between this work and those from other research institutes.....	130
Figure 73: Cavity length dependent inverse differential quantum efficiency of Ga <sub>0.68</sub> In <sub>0.32</sub> N <sub>0.015</sub> As <sub>0.985</sub> /GaAs <sub>0.98</sub> N <sub>0.02</sub> laser .....	130
Figure 74: Temperature dependent device operation of Ga <sub>0.68</sub> In <sub>0.32</sub> N <sub>0.015</sub> As <sub>0.985</sub> /GaAs <sub>0.98</sub> N <sub>0.02</sub> .....	131
Figure 75: Maximum power of 350 mW from Ga <sub>0.68</sub> In <sub>0.32</sub> N <sub>0.015</sub> As <sub>0.985</sub> /GaAs <sub>0.98</sub> N <sub>0.02</sub> laser .....	132
Figure 76: L-I for the laser diode with Ga <sub>0.65</sub> In <sub>0.35</sub> N <sub>0.017</sub> As <sub>0.983</sub> /GaAs <sub>0.978</sub> N <sub>0.022</sub> .....	132
Figure 77: Emission spectrum of Ga <sub>0.65</sub> In <sub>0.35</sub> N <sub>0.017</sub> As <sub>0.983</sub> /GaAs <sub>0.978</sub> N <sub>0.022</sub> at 1.39 μm.....	133
Figure 78: Laser emission at 1.4 μm at room temperature .....	134
Figure 79: L-I curve of a GaInNAsSb/GaNAsSb ridge waveguide laser .....	135
Figure 80: Optical spectrum of a GaInNAsSb/GaNAsSb ridge waveguide laser with peak emission at 1.465 μm.....	135
Figure 81: L-I curve and optical spectrum for a GaInNAsSb/GaNAsSb ridge waveguide laser with peak emission at 1.49 μm .....	136

# TABLE OF CONTENTS

Abstract .....	iv
Acknowledgment .....	vi
Dedication.....	vii
List of tables.....	ix
List of figures .....	x
Chapter 1: Introduction.....	1
1.1 Motivation .....	1
1.2 Optical Fiber Communication Fundamentals .....	3
1.2.1 Optical Fibers.....	4
1.2.2 Sources of Light.....	5
1.2.3 Optical Amplifiers.....	10
1.2.3.1 Semiconductor Optical Amplifiers.....	11
1.2.3.2 Erbium-Doped Fiber Amplifier.....	12
1.2.3.3 Raman Amplifier.....	14
1.2.4 Fast Switches .....	17
1.2.5 Photodetector .....	18
1.3 Long Wavelength Lasers .....	20
1.3.1 Optical Communication Lasers .....	20
1.3.2 The Advantages of VCSEL .....	22
1.3.3 History of Long Wavelength VCSELs.....	24
1.4 Material Choices for Long-Wavelength Lasers .....	26
1.5 History of Dilute Nitride Compound Semiconductor for Lasers .....	28
1.6 Outline of the Dissertation .....	29
Chapter 2: Molecular Beam Epitaxy of GaInNAs and GaInNAsSb.....	31
2.1 Solid Source Molecular Beam Epitaxy (SSMBE).....	31
2.1.1 Introduction .....	31

2.1.2	Fundamental Background of MBE .....	32
2.1.3	Solid Source MBE Configuration for this work .....	33
2.2	MBE Materials .....	35
2.2.1	Elemental Sources.....	35
2.2.2	Arsenic Valved Cracker .....	36
2.2.3	Radio Frequency (rf) Nitrogen Plasma Source.....	37
2.2.4	Antimony Source .....	41
2.3	<i>In-situ</i> Monitoring in MBE .....	42
2.3.1	Introduction .....	42
2.3.2	Reflection High-Energy Electron Diffraction (RHEED).....	42
2.3.3	RHEED Intensity Oscillation .....	44
2.3.4	Normal Incidence Reflectivity Oscillations .....	45
2.3.5	Beam Equivalent Pressure (BEP) .....	47
2.4	Sample Preparation .....	48
2.5	Epitaxial Growth of GaAs based Material .....	49
2.6	GaInNAs and GaInNAsSb growth .....	53
2.6.1	Nitrogen Concentration .....	54
2.6.2	Miscibility Gap in Dilute Nitride Material.....	55
2.6.3	Antimony as a Surfactant .....	58
Chapter 3:	Thermal Annealing Effect on GaInNAs and GaInNAsSb quantum well .....	63
3.1.	Photoluminescence Improvements by Thermal Annealing .....	63
3.2.	Photoluminescence Peak Blue-Shift during Post Growth Annealing.....	67
3.2.1	Nitrogen Out-Diffusion .....	68
3.2.2	Nearest Atom Rearrangement.....	73
Chapter 4:	Characterization .....	78
4.1	Photoluminescence (PL) Spectroscopy Measurement.....	78
4.1.1	Introduction .....	78
4.1.2	Theoretical Background .....	80
4.1.3	Photoluminescence Sample Growth .....	84
4.1.4	Photoluminescence Experimental Setup and Results .....	85

4.2 X-ray Diffraction (XRD) .....	91
4.3 Cathodoluminescence (CL).....	96
4.4 Secondary Ion Mass Spectrometry (SIMS).....	101
Chapter 5: GaInNAs and GaInNAsSb Ridge Waveguide Edge Emitting Laser .....	105
5.1 Quantum Well Modeling .....	105
5.2 Electron Energy Levels in Strained Quantum Wells.....	110
5.3 Band Gap Energy Calculations of Dilute Nitride Materials .....	115
5.3.1 Bandgap Calculation of GaNAs .....	115
5.3.2 Bandgap Calculation of GaInNAs and GaInNAsSb.....	119
5.4 Fabrication and Characterization of GaInNAs and GaInNAsSb Lasers.....	122
5.4.1 Laser Structure Growth .....	123
5.4.2 Laser Structure Fabrication .....	126
5.5 Laser Results .....	128
5.5.1 1.3 $\mu$ m GaInNAs/GaNAs Lasers .....	128
Chapter 6: Conclusion and Future Improvement.....	137
Bibliography .....	140

## CHAPTER 1: Introduction

The goal of this work is to develop a new material, GaInNAs and GaInNAsSb for optical fiber communication. In comparison to the current material system utilized for these applications, this novel material will provide the opportunity for inexpensive, easy-to-handle, and mass-production-suitable communication devices. These communication devices will be the platform to replace copper based coaxial cable with inexpensive and long lasting optical fiber in local and metro networks.

### 1.1 Motivation

There is now a very high demand for low cost, 1.3-1.6  $\mu\text{m}$  lasers that are essential for the rapid expansion of optical storage area networks (SANs), local area networks (LANs), metro area networks (MANs), and wide area networks (WANs). The requirements for these lasers are broad operating temperature range (-10 to 90°C) without cooling, moderate power (>10 mW) in the fundamental mode, inexpensive platform, high speed capability, and high volume producibility. There is also a growing interest in higher power lasers, at similar wavelengths, as pumps for Raman amplifiers to extend the available bandwidth.

InP-based lasers have provided the sources for all these applications to date, but they suffer shortcomings that greatly hinder their ability to produce low cost vertical-cavity surface-emitting lasers (VCSELs)<sup>1</sup> and high-power Raman pump lasers. Research has shown that GaInNAs can be coherently lattice matched to GaAs<sup>2,3,4,5,6</sup> while providing the proper bandgap energy (Figure 1). Additionally, GaAs-based lasers with dilute nitrogen active layers can take advantage of the well-developed GaAs processing technologies and the superior distributed Bragg reflector (DBR) mirror technology for VCSELs<sup>7,8</sup>. Laser diodes with GaInNAs active layers have shown prospective

characteristics, including low threshold current density, high temperature CW operation, and high  $T_0$  in the wavelength range of 1.1  $\mu\text{m}$  to 1.3  $\mu\text{m}$ .

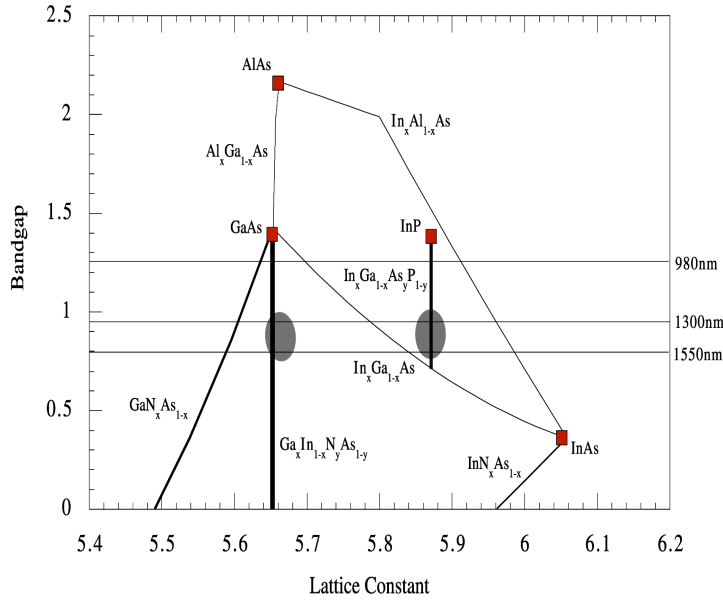


Figure 1. Bandgap energy vs. lattice constant for materials relevant to telecommunications.

One challenge in achieving longer wavelength ( $>1.3 \mu\text{m}$ ) GaInNAs occurs during the annealing process which must be done to improve the material quality<sup>9</sup>. One of the main reasons for this wavelength blue-shift during high temperature annealing (700-900°C) is that nitrogen out-diffuses from the quantum wells, resulting in a shift of the emission spectrum to shorter wavelengths. Additionally, there is evidence that the nitrogen nearest neighbors (Ga or In) change during anneals. It is possible that increasing number of In nearest neighbors around N decreases the local lattice spacing which may increase the bandgap and contributes to the luminescence blue-shift. So far, most attempts to achieve laser emission beyond 1.3  $\mu\text{m}$  with low threshold current densities have been unsuccessful in post-annealed GaInNAs material. New structures utilizing GaNAs barriers and a new quantum well material, with antimony, to achieve post-annealed long-wavelength optical emission are presented in this work. The structures with nitrogen in the barriers reduce the blue-shift of luminescence by suppressing nitrogen out-diffusion from the quantum wells and decreasing carrier confinement between the barriers and quantum wells<sup>5</sup>. The addition of antimony, both incorporated

into the crystal and used as a surfactant, enables higher indium incorporation and longer wavelength emission than 1.5  $\mu\text{m}$ . GaNAs barriers also reduce the overall strain of the active region because the high indium mole fraction quantum wells are compressively strained and the GaNAs barriers are tensely strained. Strain compensation allows a greater number of quantum wells which is necessary for high output power in-plane lasers and vertical cavity surface emitting lasers.

The MBE growth and fabrication and characterization of high efficiency long wavelength multiple quantum well (MQW) GaInNAs(Sb) ridge-waveguide laser diodes using GaNAs(Sb) barriers and longer wavelength photoluminescence are described in this work. The wide wavelength range coverage and high output power of these GaAs-based lasers makes them ideally suited for transmission and amplification.

## **1.2 Optical Fiber Communication Fundamentals**

The fundamentals of digital optical communication are straightforward. To send data as simple as a phone message or as complicated as a picture, the data is digitized into a series of binary bits which are transmitted bit-by-bit, decoded at the receiving end, and re-created into the original message or picture. The ones and zeroes are encoded by turning the signal source on or off. In the past, the signals have been electrical, mostly through copper wire, but increasingly it is composed of light pulses. Optical fiber communication uses a laser to produce the light, and the information is encoded using either direct-modulation of the laser or an external modulator. This modulated optical signal is transmitted through optical fibers, amplified as needed, received with a photodetector and re-created into the original data with a demodulator.

An optical signal in an optical fiber is superior to an electrical one in copper wire because of less attenuation, higher switching speeds, and greater data capacity (higher bandwidth). The physics of an optical communication system involves such fundamental concepts as light scattering, superposition of waves, and optical excitations of electrons in semiconductor crystals and in glasses. The complex state of modern optical communications can be simplified to five key components: optical fibers, light sources,

optical amplifiers, optical switches, and photodetectors. In this chapter, a brief introduction of each component will be presented.

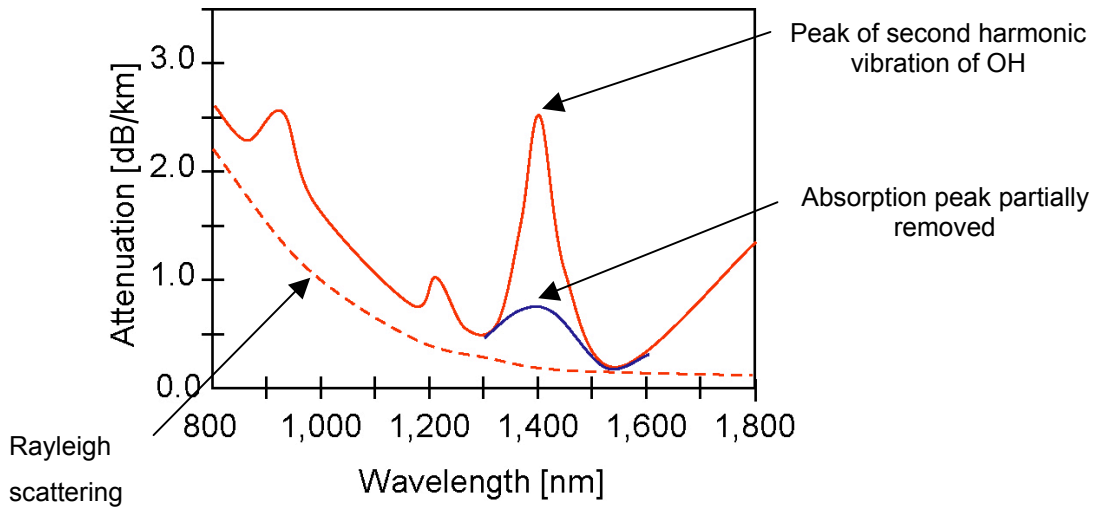


Figure 2. Transmission loss in conventional optical fiber.

### 1.2.1 Optical Fibers

The amount of loss of the transmitting medium is the most important factor in determining the practicality of optical communications. The remarkable development of SiO<sub>2</sub> glass fiber over the past 30 years has made possible the powerful modern optical fiber communication networks. Figure 2 shows the optical loss as a function of wavelength for a standard optical fiber. Loss is expressed as a number of decibels (dB) per kilometer. The fiber has minimum loss at the wavelength of 1.55 μm, where it is only about 0.2 dB/km. It is limited by Rayleigh scattering and molecular absorption.

In addition to the loss processes, dispersion (spatial spreading of a light pulse along the direction of propagation) can be an important factor limiting the amount of data that may be sent through a fiber. Unlike loss, however, the dispersion can be controlled by manipulating the distribution of dopants in the glass. When the optical fiber is made, small amounts of germanium or fluorine are added to the center of the fiber to form a core. These dopants do not change the loss, but serve to confine the light by raising the index of refraction in the center. The propagating light then preferentially travels along the core, where its speed is a bit slower, in a confinement process similar to total internal

reflection. Forming and doping the fiber to confine light and minimize dispersion requires heating the glass. Unfortunately, when a torch is used that burns  $H_2$  with  $O_2$  (and produces  $H_2O$ ), some of the resulting water gets into the fiber. The water absorbs light strongly when the constituent hydrogen and oxygen atoms vibrate in the fiber. The use of dry heat has allowed the production of new fiber without an OH peak. This allows communication systems to use all available bandwidth in the range of 1280 to 1610 nm, which corresponds to a bandwidth of 50THz. Before it is possible to implement such a wideband system, new components that are capable of operating over the entire range are needed.

### **1.2.2 Sources of Light**

Much research has been done to respond to the bandwidth challenge by developing advanced light sources that provide the needed output power and modulation rate at the required wavelength. The state-of-art multi-wavelength architecture is called dense wavelength division multiplexing (DWDM). The optical window is divided into as many closely packed wavelength bands (or channels) as possible while still preserving the information content. The optical signal in each small band should be clean and stable and have minimal chromatic content; be nearly a single wavelength and stay that way. In the existing optical backbone using DWDM, relatively few source lasers are required, hence absolute wavelength stability is essential and cost becomes relatively irrelevant. In order to expand bandwidth to SANs, LANs, MANs, and WANs, large number of lasers will be required, hence cost becomes the important criteria. The transmitting source for these new networks has to have output power of a few milli-watts, be insensitive to environmental change (temperature, humidity etc), have long life span (>10,000 hours), and still remain inexpensive. Tunability is more and more desirable as modern optical the communication architecture evolves. The basic theory behind the semiconductor laser is to excite electrons from 'a ground state' to a higher energy level, 'excited states'. In a semiconductor laser, the ground state refers to the valence band and the excited state to conduction band in n-type material and inversely in p-type material. In p-type material a conducting electron has a very short lifetime ( $\sim 10^{-9}$  second) and it will quickly relax to

the valence band. In this process, it releases its excess energy in the form of a photon.

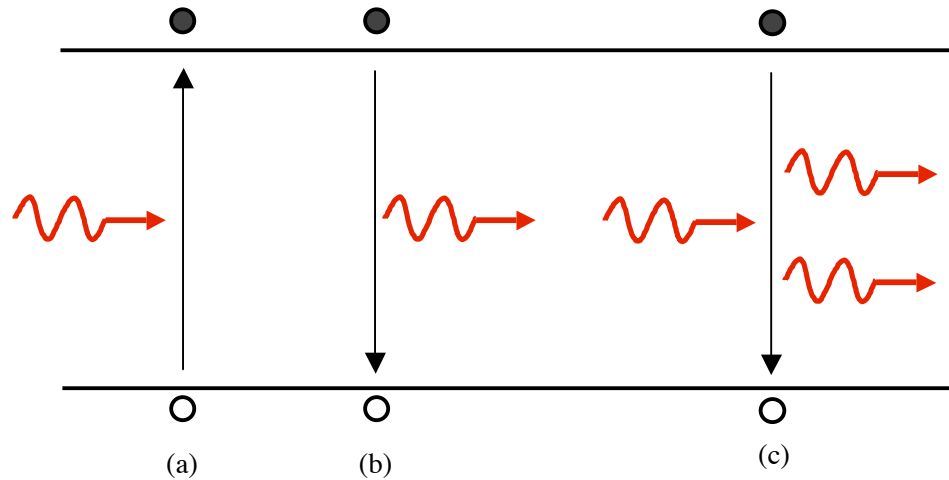


Figure 3. Interaction between electron and photon; (a)absorption, (b)spontaneous emission, (c)stimulated emission.

Since the bandgap energy ( $E_g$ ) of semiconductor materials are well-defined, only photons with distinct energies of bandgap are created by any particular semiconductor.

As shown in Figure 3, there are three basic types of interaction between electrons and photons: absorption, spontaneous emission, and stimulated emission. Absorption (Figure 3 (a)) occurs when a photon of higher energy than bandgap energy ( $E_g$ ) of semiconductor material is absorbed by an electron in the valence band and causes an electron to move up to the conduction band. Spontaneous emission (Figure 3 (b)) occurs when an excited electron spontaneously returns to the valence band, emitting a photon of random phase and direction with the same energy as bandgap energy ( $E_g$ ). However, if a photon with the same energy as  $E_g$  interacts with the crystal whose electrons are in the conduction band at the photon wavelength, it can induce the electrons to relax down to the valence band, emitting a new photon which will be in phase with the incoming photon and traveling in the same direction. This is called stimulated emission (Figure 3 (c)), and the probability of stimulated emission is proportional to the intensity of in-phase photons.

Under normal conditions, for any given transition there are many more electrons in the valence band than in the conduction band. In this case, if an excited atom emits a photon by spontaneous emission, the photon is likely to encounter another electron in the

valence band and be absorbed. Suppose the conditions are such that the number of electrons in the conduction band is greater than the holes in the valence band. This condition is called population inversion. When a conduction electron recombines with a hole, spontaneously emitting a photon, the photon is likely to interact with another conduction band electrons, stimulating the emission of another photon. These two in turn will probably encounter other excited atoms and stimulate more emissions, which will stimulate more emissions, and so on. In this sense, the medium acts as a light amplifier. The original photon has been amplified to a large number of identical photons, all in phase and traveling in the same direction. There are basically two ways to create a population inversion, which is often referred to as pumping. One is to pump electrons optically and the other is electrically. Optical pumping requires a separate light source with energy higher than  $E_g$  of the gain medium to be pumped. Photons generated by this light source are absorbed by the gain medium and excite electrons from the valence band to the conduction band. Electrical pumping is based on minority carrier injection through a  $p-n$  junction. When a diode is under forward bias, electrons move from the cathode ( $n$ -region) through the  $p-n$  junction where holes from anode ( $p$ -region) have moved by electric field. At low current densities, the process in a laser is the same as that which occurs in a light emitting diode (LED) and indeed, a laser diode produces incoherent light like an LED. At the  $p-n$  junction of a laser, electrons meet holes and recombine. At higher current densities, the number of electrons and holes are higher than that in equilibrium (population inversion) and initial spontaneous emission then sets off the cascade of stimulated emission.

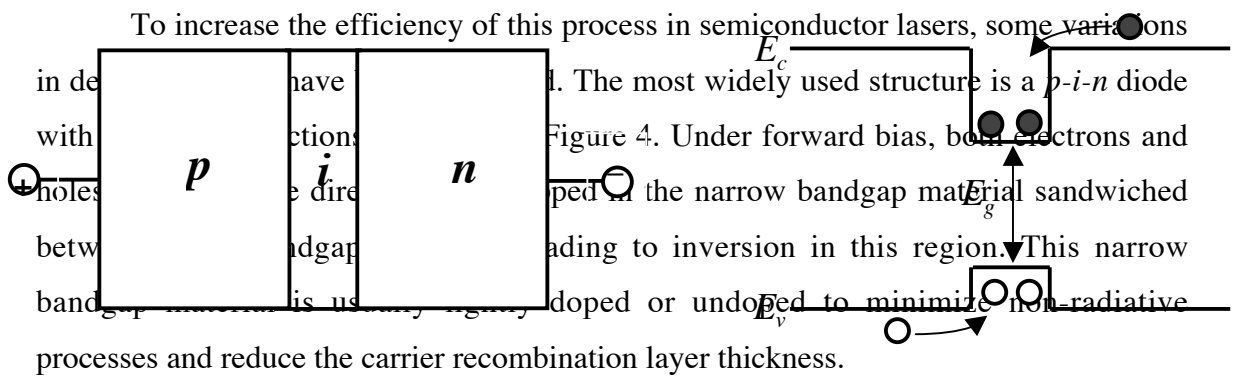


Figure 4. The common semiconductor laser structure; (a) schematic of  $p-i-n$  structure (b) energy band diagram of  $p-i-n$  heterojunction.

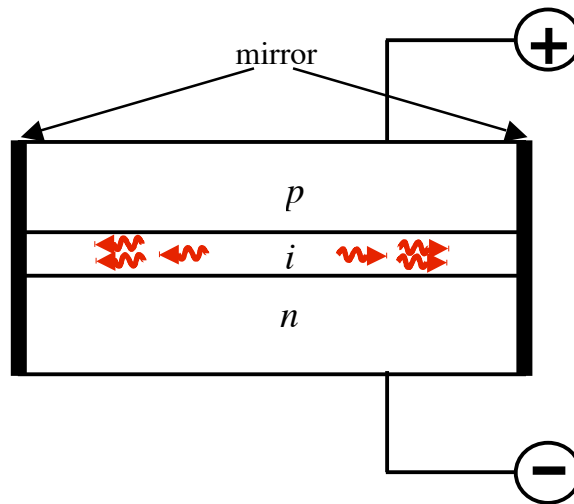


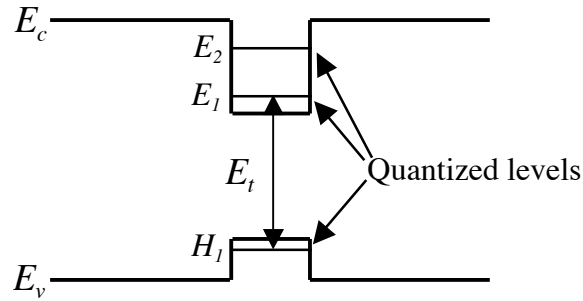
Figure 5. A semiconductor laser diode structure with mirrors at both ends.

Now suppose that such a  $p-i-n$  structure is built with mirrors at both ends, as shown in Figure 5. Applied voltage causes a current of electrons and holes to flow into the  $i$  region and recombine there. The recombination starts the emission of photons. These photons travel inside the material for a while, stimulating more emissions, until they reach a boundary of the laser. However, if one of the spontaneously emitted photons happens to be along the horizontal axis of the device, this photon and those with the same momentum will reflect off the mirrors at both ends of the rod and travel back through it, stimulating more emissions and being amplified further. These photons will bounce off the back mirror as well, and (as long as they are parallel to the axis) will continue being reflected back and forth, and will be amplified as they traverse the cavity. Now if one of the mirrors is made to be partially transmitting, then part of the light will escape out that end. This escaped light is the laser beam. Lasing occurs when the combination of material loss and escaping light is exactly balanced by the amplification. This essential optical feedback for a laser is obtained by reflecting part of the light back through the gain medium, using two mirrors to create a laser cavity. For the initial semiconductor lasers, these mirrors were formed by cleaving the semiconductor along a crystal facet and partial reflection occurs due to the refractive index difference between the semiconductor and air. The reflectivity of such a facet is around 0.32 between GaAs and air. An other type of mirror is called a distributed Bragg reflector (DBR). A DBR is a distributed mirror, in

which the reflectivity of periodically spaced elements made by different refractive index materials add coherently to produce a mirror with much higher reflectivity (>99%).

The laser light produced has several important characteristics. First, only photons traveling extremely close to parallel with the axis of the rod will be amplified enough to escape through the mirror. Hence the laser light will only exist in a narrow beam. Second, as all the photons are coming from the same transition, they have exactly the same energy and hence the same wavelength. Third, since stimulated emission produces another photon in phase with the incoming one, all the photons in the laser beam will be in phase, and thus the laser light will be coherent. These three properties are what distinguish laser light from that produced by other sources, such as LEDs or incandescent bulbs.

The most common structure for the amplification region is the quantum well structure. There are a number of reasons for utilizing a quantum well structure. One of them is the reduction of current required to achieve carrier inversion (transparent current) by reducing the size of the gain medium and the reduced density of states. Another one is reduced temperature sensitivity of threshold current density due to improved confinement of electrons and holes. The other advantages are greater frequency tuning range and higher quantum efficiency. As the middle layer of a heterojunction becomes thinner,



quantization of energy levels start to appear as shown in Figure 6<sup>10,131</sup>.

The quantum well energy levels are represented in Figure 6 as  $E_t$ . The  $E_1$  and  $H_1$  indicate the confined energy levels which electrons and holes occupying in the quantum wells during operation. Normally  $H_1$  corresponds to the first heavy hole level, HH1, rather than first light hole level, LH1 primarily because of the heavier mass. However,

*Figure 6. Energy levels in quantum well structure.*

the quantum well is usually under compressive strain and this can change the alignment. The QW breaks the degeneracy of valence band at the valence band energy peak ( $k = 0$ ). Under compressive strain, the effective mass of the hole in the heavy hole energy band decreases and the energy band pushes above that of light hole band. Electron energy levels in quantum wells are discussed in chapter 5.2. Electrons and holes are spatially confined at densities around  $10^{18} \text{ cm}^{-3}$  in the quantum well. The carriers thermalize so the electron-hole energy differences tend to be near that of the quantum well transition energy. Because of the high carrier density, the carriers begin to fill the band and the average carrier density is above the  $k = 0$  energy, so when the electrons and holes recombine, they produce light with wavelengths slightly higher than the transition energy and somewhat above the bandgap energy of the quantum well material.

In addition to confining electrical carriers, the quantum well structure also confines the emitted light along the layers, because the average refractive index of the quantum well and barrier materials is higher than that of the surrounding material. This is because the refractive index of the material is inversely proportional to the band gap of the material and the active area of a laser is made of smaller band gap material for better confinement of the carriers. This higher refractive index of the active area forms a waveguide that serves to confine the optical mode around the active layer. Some photons exit from the quantum well layer of the gain section; some get absorbed by the material, but most stimulate the emission of other photons. The chance of stimulated emission increases as more carriers are injected. Transparency occurs when material loss equals gain, and at higher pumping power the quantum well stack becomes a gain medium.

### **1.2.3 Optical Amplifiers**

Thus far, the methods of producing light and of transmitting it through fibers have been described and these elements operate over the relatively wide range of wavelengths used for optical communications shown in Figure 1. However, there is always some loss and sending an optical signal over a long distance will require some form of optical amplifier (OA). There are several types of optical amplifiers in an optical communications system. One type of OA can boost a signal inside the source, prior to

feeding it into an optical fiber by integrating an amplifier into the transmitter. Another type of OA is a pre-amplifier which boosts a signal entering into a photodetector to improve the detector operation. The last type of OA is an in-line regenerator which amplifies a signal to compensate for loss along the fiber. The key performance requirements for a wavelength division multiplexing (WDM) amplification scheme are: satisfactory amplification of small signals, a high saturation power associated with signal output, low added noise, and broad gain bandwidth. Several different amplifiers will be introduced in this chapter.

### 1.2.3.1 Semiconductor Optical Amplifiers

A semiconductor optical amplifier (SOA) is the oldest and most basic optical amplifier. It works in a similar way to a basic laser. The structure is much the same, with two specially designed slabs of semiconductor material on top of each other, with another material in between them forming the active layer. An electrical current through a n or p-layer injects electrons and holes into the active region (electrical pumping), which can then fall back to the non-excited ground state and emit photons.

There are two key differences between SOAs and lasers. In a standard laser, highly reflective mirrors at both ends are required to keep light bouncing back and forth within the cavity. With a SOA, the optical signals need to make a single pass straight through the cavity and be emitted of the far end, so light reflecting back into the cavity must be avoided. This means that anti-reflective coatings must be applied to both ends.

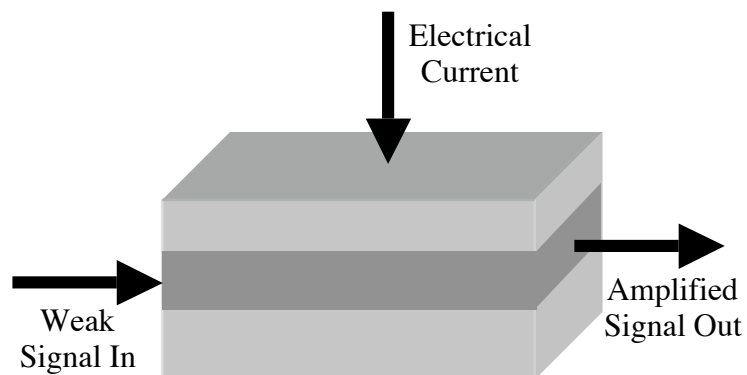


*Figure 7. Semiconductor optical amplifier*

Also, for telecommunication lasers, single mode and single wavelength operation are required and inputs are designed to be these requirements. However, in a semiconductor amplifier it is desirable to amplify light at as many different wavelengths as possible. This is because the optical network signals may be transmitting at the many different wavelengths that all need to be amplified simultaneously.

*Figure 8: Erbium doped fiber amplifier diagram*

The excited electrons in the semiconductor are now stimulated by incoming light from the optical signals to move down to their ground states. The photons produced by an electron losing energy from its excited state exactly match the photon that caused the emission in the first place just like the stimulated amplification in a laser. Therefore, there are now two photons representing one particular section of a signal where previously there was only one. Hence, the signal has now been amplified. These two photons can now cause more stimulated emission as they travel down the device, until they all exit together as a successfully amplified signal.

SOAs can be designed to be used for quite broad wavelength regions, especially around the 1300 nm transmission window. In fact, as the demand for more wavelengths grows, there will be much need for amplifiers for entire range between 1280 nm and 1600 nm and semiconductor amplifiers may have an important role to play in such systems. Unfortunately, SOAs are bulky, do not give as much amplification as erbium doped-fiber amplifiers (EDFAs) described in the next chapter around the 1550 nm region, and are more expensive than EDFA and Raman amplifiers. SOAs also have greater coupling loss than EDFA and Raman amplifier since the signal exits the fiber to enter and exit the SOA.

### 1.2.3.2 Erbium-Doped Fiber Amplifier

An erbium doped fiber amplifier (EDFA) consists of a few meters of optical fiber doped with a small fraction ( $\sim 10^{-4}$  %) of the rare earth element, erbium. An optical signal is transmitted in this fiber, along with the high power light from a special pump laser that is designed to excite the erbium ions as shown in Figure 8.

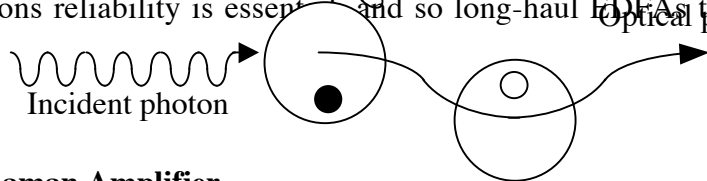
Erbium doped silica glass has several energy levels that are involved in amplification. The erbium atom can be excited with a 1480 nm pump laser into the first

excited state. These excited electrons decay to the ground state after a certain amount of time. When falling back to the ground state, the electrons have extra energy, which they give out as photons. This process is spontaneous emission because the electrons fall back to the ground state and give out photons without any catalyst. Such spontaneous emission can build up in the amplifier and is known as amplified spontaneous emission (ASE). ASE is an undesirable effect and is an inherent noise source in EDFAs.

However, if the wavelength of an optical signal is at around 1550 nm, the optical signal can cause some of those excited electrons to fall down to the ground state and give out photons. This process is stimulated emission because the signal is directly causing the photons to be emitted. The emitted photons are at the exact same wavelength as the signal and now a part of the signal. The signal now has more photons representing it than before, so it has been amplified. This process can continue throughout the length of the erbium-doped fiber, until the photon density has been increased to a desired level and hence amplified. This amplification band is fortuitously centered around 1550 nm and extends from 1530 to 1580 nm. This range of wavelengths is known as the conventional-band (C-band). EDFAs can also be designed to produce amplification between around 1580 nm and 1610 nm, which is known as the long-band (L-band). The amount of amplification at different wavelengths varies, and this causes problems since each wavelength in DWDM system will be amplified differently. There has been much effort in EDFA design to achieve similar levels of amplification at all wavelengths. The most common is gain flattening.

Another EDFA pump laser source is 980 nm pump laser. The 980 nm pump laser excites the erbium ions into a much higher state than the 1480 nm pump. However, the electrons only stay in that higher state for a very short period of time ( $\sim 10^{-9}$  second) before moving down to the next lower state. At the next lower state, the lifetime becomes much longer, around  $10^{-3}$  second, which is much longer than ions excited by the 1480 nm pump laser. The longer upper-state lifetime leads to efficient amplification. This also reduces the unwanted spontaneous emission that adds to the noise in the system. Therefore, 980 nm pump lasers give greater amplification efficiency and are the preferred pump method for EDFAs.

EDFAs are commonly used in long-haul systems where signals often have to travel thousands of miles. They can be made in compact, weather-resistance packages that will be placed every 50 miles or so along the length of the system. For such applications reliability is essential and so long-haul EDFAs tend to be of very simple design.



### 1.2.3.3 Raman Amplifier

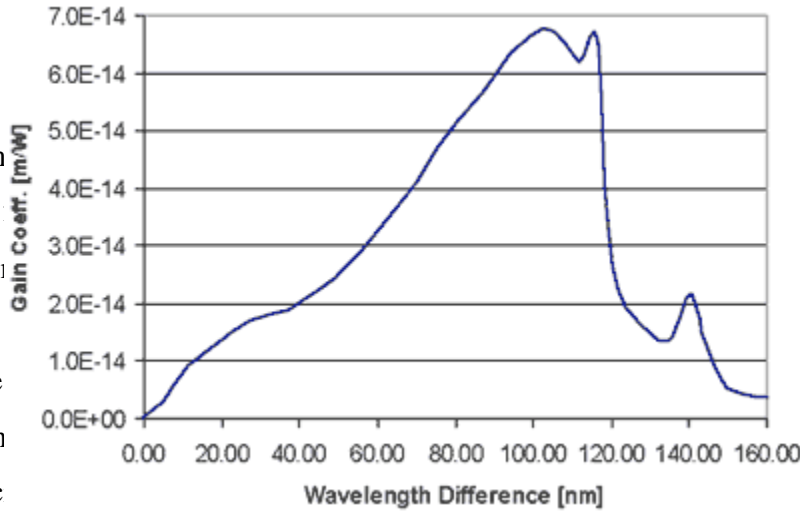
*Figure 9. Physical picture behind Raman scattering.*

The erbium doped fiber amplifier has helped produce the tremendous improvements in modern communication systems, however, they cannot provide amplification over the wide range of wavelengths needed for future generation networks.

A new candidate for producing amplification across the full bandwidth of next generation networks is the Raman amplifier. Raman amplifiers are particularly promising for future communications applications because of their great versatility. In addition to working over a wide transmission range (1200 nm ~ 1600 nm), Raman amplifiers can boost a signal in any untreated ordinary SiO<sub>2</sub> fiber. Raman amplifiers are advantageous compared to SOAs because of their lower added noise. Moreover, the Raman amplification process can actually prevent a decrease in the ratio of the signal to the noise by acting on the signal as it travels over long distances in the fiber, with the entire fiber being turned into a distributed amplification medium.

In Raman amplification, power is transferred from a laser pump beam to the signal beam through a coherent process known as stimulated Raman scattering (SRS) as shown in Figure 9. Raman scattering is the interaction between a light beam and a fluctuating charge polarization in the medium and results in an energy exchange between the incident light and the medium. In spontaneous Raman scattering, the charge polarization is a result of thermally excited inter-atomic displacements and changes in electronic density. For example, a thermal vibration of silicon and oxygen atoms in a glass fiber at a frequency  $\omega_{ph}$  (optical phonon frequency) can modulate the charge polarization. When an electromagnetic wave with frequency  $\omega$  is incident on the fiber, a band of phonons peaked at frequency  $\omega_{ph}$  is emitted or absorbed, and some of the incident light appears at both  $\omega - \omega_{ph}$  (Stokes shifted light) and  $\omega + \omega_{ph}$  (anti-Stokes shifted light).

Figure 10



In high intensity source of frequency transfers propagate of the pump by the inc

offset (the Raman shift)<sup>11</sup>. The signal light pump light source light coherently the pump beam decreasing width n so that  $\lambda_{\text{pump}} - \lambda_s$

The ability to make this choice of pump laser wavelength independent of the signal wavelength is a key advantage of Raman amplification, namely any band of signal frequencies throughout the optical fiber transmission range can be amplified via an appropriate selection of the pump laser wavelength.

The Raman amplification process has several distinct advantages compared to conventional SOAs or EDFAs. First, as shown in Figure 10, the gain bandwidth is large (about 160 nm in SiO<sub>2</sub> fibers) because the band of vibrational modes in fiber is broad. Second, the wavelength of the excitation laser determines which signal wavelengths are amplified. By using several lasers, the Raman amplifier can be made to work over the entire range of wavelengths that would be used with SiO<sub>2</sub> fibers. Thus, the amplification bandwidth would not limit the communication system bandwidth. A disadvantage of Raman amplifiers is that they require high pump powers broad bandwidth laser sources. However, this amplification method is showing a promising promise: a recent demonstration by Kawanishi et. al.<sup>12</sup> used Raman

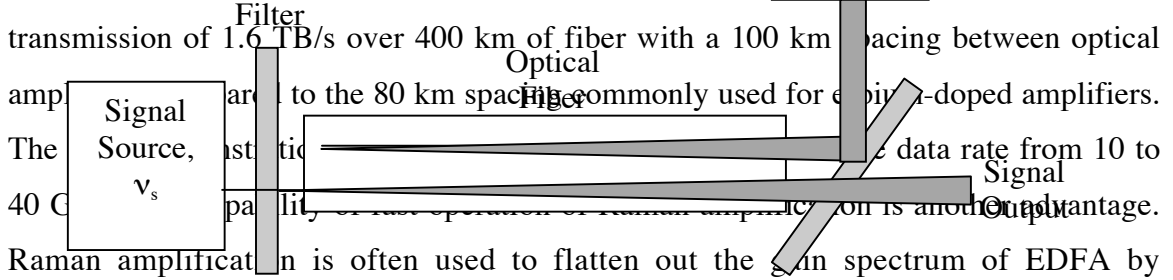


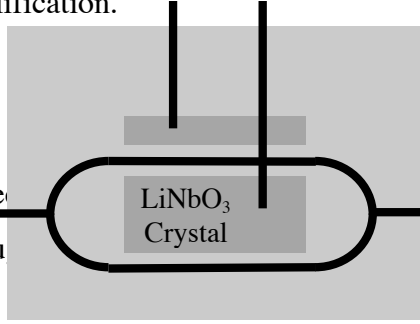
Figure 11. Schematic of Raman amplifier system.

compensating the under-amplified wavelengths with a Raman amplifier. This is called hybrid Raman-EDFA amplification.

### 1.2.4 Fast Switches

In modern high-speed networks, fast modulators are required to handle the routing of huge amounts of data to its intended destination, modulate signals, route data to its intended destination, end of the line. Traditional architectures use electronic modulators, converting the light to electrical signals, electrically modulating it, and reconvert it to light for further transmission (O-E-O connection). With the high transmission rates possible in the optical parts of the network, the slowness of this procedure is causing a data flow bottleneck. Also the electronic and optical units needed for this type of switching are more expensive than pure optical switching. Optical switching technology is capable of relieving this electronic bottleneck<sup>13</sup>. Recently, new multiplexers made of arrays of movable mirrors have been introduced to route optical signals without E-O-E conversion and have been shown to switch quickly enough.

Figure 12. Mach-Zehnder Modulator with LiNbO<sub>3</sub> Crystal



In principle, a fast optical switch can be made by using an intense optical or electrical pulse to induce a refractive index change in the medium through which the less intense optical signal is to pass. This refractive index change then modulates the transmission of the signal through the medium. A simple but effective type of electrically controlled, optically transparent modulator is the EA modulator for the light source in Figure 7. Like the gain section in of lasers, the EA modulator consists of MQW layers and, when unperturbed, it is transparent to the light signal. However, under reverse electrical bias, the quantum well and barrier energies are distorted so that absorption rises sharply at energies just above the MQW transition energy. A few volts of reverse bias applied to the structure can render the EA modulator opaque to 99% of the incident flux.<sup>14</sup>

Kang et. al. demonstrated an all optical switch using a Mach-Zehnder interferometer design<sup>15</sup>. The schematic of the Mach-Zehnder modulator with LiNbO<sub>3</sub> is shown in Figure 12. LiNbO<sub>3</sub> is the material commonly used for this structure due to its

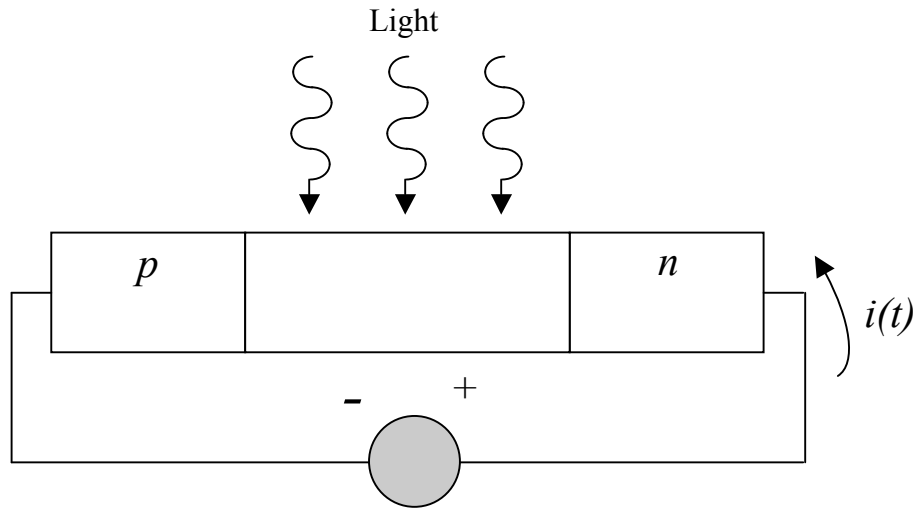
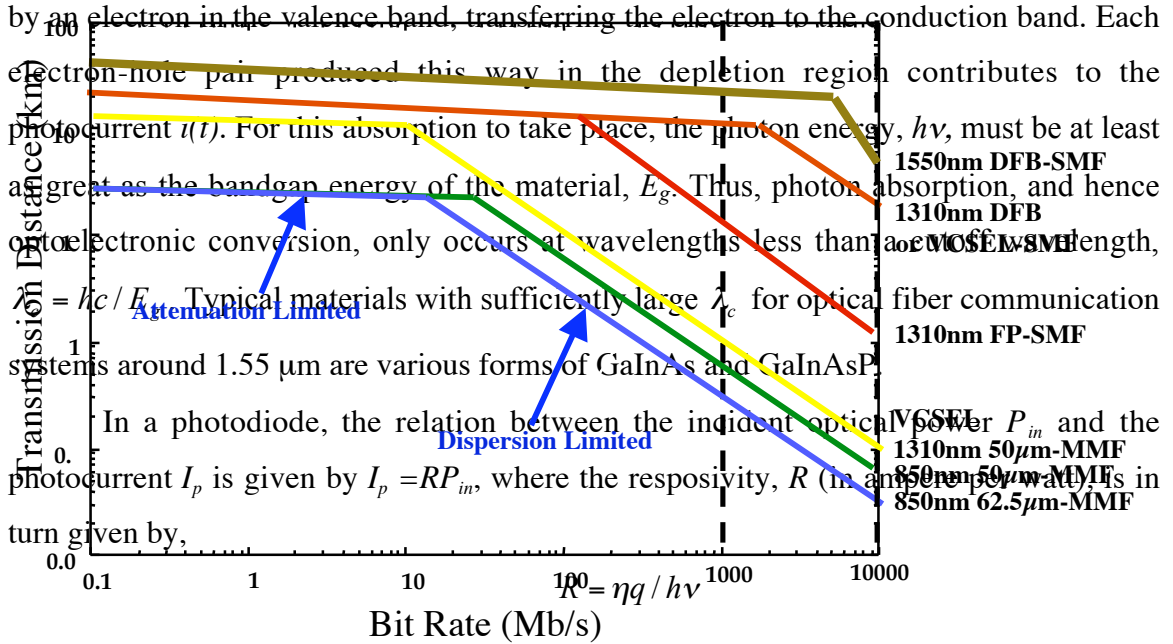


Figure 13. Schematic of photodetector.

large electro-optic coefficient. The input light is split between two paths and recombines at one output port. Electrical control pulses injected into the interferometer produce a differential phase shift between the two paths of the interferometer which results in switching of the data pulse at the output port. For the symmetric Mach–Zehnder design, the switching time depends only on the control-pulse separation and can approach sub-picosecond timescales.

### 1.2.5 Photodetector

The photodetector converts the optical signal to a photocurrent, using direct detection, and the amplifier raises the power of the photocurrent to a level sufficient for further electronic processing. In the digital signal case, this processing is primarily clock recovery, sampling, and threshold detection to extract the digital bit-stream from the received signal. The photodetector used in optical communication systems are semiconductor photodiodes. In the simplest device, the  $p$ - $n$  junction, the operation is essentially the reverse of a semiconductor optical amplifier. As shown in Figure 13, the junction is reverse biased, enlarging its depletion layer, and in the absence of an optical signal only a small, minority carrier current, called the dark current, flows. A photon impinging on the surface of the device and entering the semiconductor can be absorbed



where  $\eta$  is the quantum efficiency of the device, which depends on the fraction of incident photons absorbed. The absorption coefficient of the semiconductor materials currently in use is high enough so that a very thin slab of the material (on the order of few  $\mu\text{m}$ ) is sufficient to make  $\eta \approx 1$ .

### 1.3 Long Wavelength Lasers

As stated in chapter 1.1 and 1.2, the extension of high capacity optical communications to move local area networks will require much lower cost lasers in the wavelength range of 1.3  $\mu\text{m}$  to 1.6  $\mu\text{m}$ . In this chapter, the history, material choices for this wavelength region and suitable device structures will be discussed.

Standard	Wavelength	Fiber type (transition length)	Use
1000BASE-LX	1300nm	SMF(5km), MMF(550m)	Campus Backbone
1000BASE-LH	1300nm	SMF(10km)	
1000BASE-SX	850nm	MMF(550m)	Premise Backbone
1000BASE-T		Twisted Pair Cable(100m)	In Room

*Table 1. Gigabit Ethernet Standard according to IEEE 802.3z*

### 1.3.1 Optical Communication Lasers

Due to technical difficulties, the first generation of optical communications were at 800 nm and used multimode fibers (MMFs). The second generation was in the 1.3  $\mu\text{m}$  range, where the optical fiber has zero material dispersion and used single mode fibers (SMFs). The third generation was at 1.55  $\mu\text{m}$  with SMFs to take advantage of the lowest loss ( $\sim 0.2$  dB/km) at this wavelength. Today, long-haul data transition with a bit rate of over 1 Tbps and a distance of over 1000 km is realized using dense wavelength division multiplexing (DWDM) combined with erbium-doped fiber amplifiers (EDFAs) and Raman amplifiers in the backbone networks<sup>16,17,18</sup>.

Recently, the bit rate demands for LANs have been increasing at a rate of 10 times per 3 to 4 years. Moreover, the demand for low cost gigabit ethernet for metro area networks (MANs) and wide area networks (WANs), with link lengths of over 10 km, has been dramatically increasing. Bit rates above 1 Gbps can only be supported by optical communication. Table 1<sup>19</sup> shows the standard for 1 gigabit ethernet according to IEEE802.3z. From this table, it can be shown that a combination of an 850 nm VCSEL and a MMF is the most cost effective combination but its transmission length is limited to only 500 m. It is used for 1000BASE-SX. On the other hand, using a 1.3  $\mu\text{m}$  Fabry-Perot (FP) laser and a MMF or SMF for 1000BASE-LX and 1000BASE-LH, this -LX and -LH can support longer transmission length of 5 km or 550 m, and 10 km, respectively, which

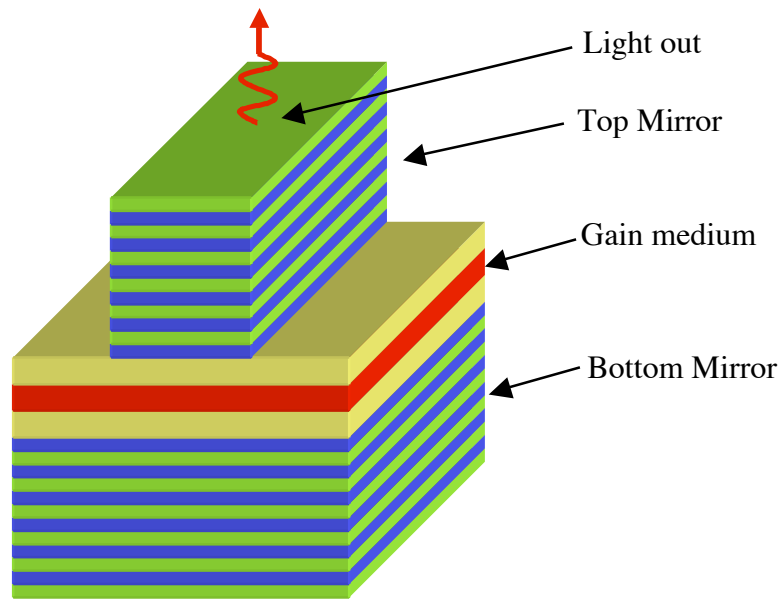


*Figure 15. A schematic of VCSEL.*

are suitable for MANs and WANs. More extensive data for various combinations of laser source and optical fiber versus transmission distance for transmission speed are shown in Figure 14<sup>20</sup>.

One of the bottlenecks to employ this high speed, high capacity, long transmission distance is the high cost of the laser source. The current laser technology is InP-based 1.3  $\mu\text{m}$  FP lasers that are high cost themselves and also require expensive temperature control systems. Thus, it is cost-effective and also volume effective if the optical transmitter can be built on a less expensive material and temperature-insensitive, so it does not require any temperature control system, typically in the temperature range from -25 to 85°C. Up to now, Fabry-Perot (FP) lasers and distributed feedback (DFB) lasers have been used for optical communications as light sources.

### **1.3.2 The Advantages of VCSEL**

Since vertical cavity surface emitting lasers (VCSEL) were first proposed by Iga of Tokyo Institute of Technology in 1977, much research has been done in laboratories

throughout the world. A typical structure of a VCSEL array is shown in Figure 15. Unlike edge emitting laser diodes, VCSELs emit light in a cylindrical beam vertically to the surface. The resonant cavity of a VCSEL is realized with multilayered-mirrors, both above and below the active layer. These multilayer mirrors are often referred as distributed Bragg reflectors (DBRs).

In general, VCSELs have high performance and low cost advantages. Other key advantages include:

1. Low threshold current and low power consumption with a small active region.
2. Feasibility of tightly packed two-dimensional integration.
3. Single longitudinal mode operation due to large mode spacing.
4. High coupling efficiency into a fiber due to a low divergence circular beam profile that matches the fiber mode.
5. Wafer-level testing before packaging.
6. High speed modulation capability due to large relaxation oscillation frequency.
7. Batch fabrication processing used in silicon technology.
8. Integration with integrated optics and circuits.

GaAs based VCSEL (compared to InP based VCSEL) has even more advantages as follows,

1. Taking advantage of  $\text{Al}_x\text{Ga}_{1-x}\text{As}/\text{GaAs}$  semiconductor DBRs.  $\text{Al}_x\text{Ga}_{1-x}\text{As}$  on a GaAs substrate has many advantages including;
  - A. One monolithic epitaxial growth of complete structure including mirrors and active layer.
    - i. Excellent yield and high quality epitaxy due to well-known growth techniques.
    - ii. Good thermal conductivity.
    - iii. Possibility of electric current injection through the AlGaAs DBR.
  - B. Relatively lower serial resistance.
  - C. Lower number of DBR pairs (less than half) required for high reflectivity due to the higher refractive index contrast in most of wavelength range.

2.  $\text{Al}_x\text{O}_y$  oxide current confinement aperture.
  - A. Easily forming a small active layer (extremely low threshold operation).
  - B. Light confinement.
  - C. Controllability of transverse mode by using multi-oxide layer (MOX).
3. Well-established process techniques.
4. Good laser temperature characteristics due to large conduction band offsets.
5. Less expensive and more physically robust substrates.
6. Monolithic epitaxial growth for mirrors and active layer.

Because of the features listed above, the unit price can be dramatically reduced, resulting in much lower priced optical components. The rapid progress of 850-980 nm range GaAs-based VCSELs for various applications has shown the commercial viability when these devices became commercially available around 1996. Long wavelength VCSELs in this range 1.2-1.6  $\mu\text{m}$  are particularly attractive for optical communications, because of low dispersion and low loss of silica optical fibers in this region. In light of these factors, a long wavelength VCSEL is expected to be an important optical source, not only for subscriber lines, but also for parallel optical communications and optical interconnects.

### **1.3.3 History of Long Wavelength VCSELs**

The first operating VCSEL was demonstrated by Soda et. al. in 1979 at 77K under pulsed conditions employing the GaInAsP material system<sup>21</sup>. The first room temperature operating AlGaAs/GaAs VCSEL was reported in 1984<sup>22</sup>. Important VCSEL technologies such as semiconductor and dielectric distributed Bragg reflector (DBR)<sup>23,24,25</sup> and quantum well<sup>26</sup> were introduced in 1985-1987. The first room temperature continuous wave (CW) operation was achieved by Koyama et. al. in 1988<sup>27</sup>. Since then, there has been an explosion of research on VCSELs. Most significant of these has been Jewell et. al. reported a very low threshold current of 1 mA by employing strained GaInAs/GaAs

quantum wells and AlAs/GaAs DBRs, and second, the use of selective oxidation of  $\text{Al}_x\text{Ga}_{1-x}\text{As}$  layer, to further reduce the threshold current was proposed<sup>28</sup> and demonstrated threshold current reduction of VCSEL<sup>29</sup>. Oxide apertures not only reduced the threshold current density but also helped confine the optical mode. An extremely low threshold current of 70 pA was reported by Hayashi et. al.<sup>30</sup> and subsequently about 10 pA was reported by Yang et. al.<sup>31</sup>. High power conversion efficiency exceeding 50%<sup>32,33</sup>, high speed modulation with a maximum bandwidth of 20 GHz<sup>34</sup> and high single mode output power of 4.8 mW<sup>35</sup> have also been realized.

Despite of great improvements made in short wavelength VCSELs, progress on long wavelength VCSEL technology has been much slower. The main problems were poor semiconductor DBRs on InP substrates and difficulty in formation of current aperture confinement structure. The first room temperature CW operation of long wavelength VCSEL was achieved in 1993 with a liquid phase epitaxy (LPE) grown VCSEL, using a buried heterostructure (BH) structure for current confinement and MgO/Si dielectric DBR, which has poor thermal conductivity. However, reproducibility problem were still unsolved due to complicated processing. In 1992, a wafer fusion technique, in which AlAs/GaAs DBRs were fused onto an InP based quantum well active region for a similar structure to GaAs VCSELs, showed optical pumped operation up to 144°C<sup>36</sup> and electrically operation at room temperature under pulsed condition in 1994<sup>37</sup>. Sub-milliamper threshold current double-fused VCSEL were reported with CW operation up to 64°C<sup>38</sup>. However, the serial resistance of devices is still high due to the fused interface and there was also a high defect density at the interface which diffused into the active layer during the fusion process. Another alternative DBR, AlAsSb/AlGaAsSb DBR on InP, has been investigated for long wavelength VCSELs<sup>39</sup>. A metamorphic growth technique with AlGaAs/GaAs top mirrors has been pursued<sup>40</sup>. In this approach, InP/GaInAsP mirrors are used for the bottom mirror and AlAs/GaAs DBRs are directly grown on top of the GaInAsP quantum well active region. All these techniques described above use InP/GaInAsP quantum well active regions, which have critical problems including,

1. Large carrier leakage from well to barrier layer due to a small conduction band offset.
2. Significant Auger non-radiative recombination which increases the threshold current density near room temperature.
3. There is a large absorption known as inter valence band absorption (IVBA) for long wavelength light. This IVBA increases the cavity losses and consequently the carrier density for lasing.
4. Inherently lower gain

The increase in threshold current and/or current density due to the factors listed above raises the device temperature, thereby increasing Auger recombination and IVBA. Because of this positive feedback, low threshold and high temperature operation of long wavelength VCSELs has been extremely difficult. Moreover, InP-based long wavelength VCSELs suffer from poor temperature characteristics, high threshold current, low output power, high power consumption, and poor reproducibility in comparison to GaAs-based VCSELs.

## 1.4 Material Choices for Long-Wavelength Lasers

There has been much research on new materials for lasers to achieve longer than 1.3  $\mu\text{m}$  emission. This effort includes InP-based materials, quantum dots (QDs), highly strained GaInAs, GaAsSb, and dilute nitrogen materials. In this part, a brief background and history of these alternative choices for long wavelength laser will be given.

(Ga)InAs quantum dot (QD) structures have been studied for zero-chirp, high modulation speeds, extremely low threshold currents and long wavelength emission. In 1994, 1.3  $\mu\text{m}$  room temperature photoluminescence of GaInAs QDs grown by MOCVD was reported. In 1996, QD VCSELs were proposed and demonstrated<sup>41,42</sup>, and achieved threshold current of 560  $\mu\text{A}$  with 7  $\mu\text{m}$  oxide aperture at wavelength of 1  $\mu\text{m}$ <sup>43</sup>, under pulsed operation. However, decreasing gain with increasing emission wavelength, which is contrary to theoretical prediction<sup>44</sup>, is a challenge and this originates from a low density

of QDs and size fluctuations of QDs. In addition, QD lasers typically suffer from poor temperature characteristics.

Material	Advantage	Disadvantage
GaInAsP/InP	<ul style="list-style-type: none"> <li>• Well established growth</li> <li>• <math>\lambda=1.3-1.6 \mu\text{m}</math> feasible</li> <li>• Low threshold current operation</li> </ul>	<ul style="list-style-type: none"> <li>• Poor <math>T_o</math></li> <li>• Poor DBR performance</li> <li>• High Cost</li> <li>• Low thermal conductivity</li> <li>• Poor performance at shorter wavelength</li> </ul>
(Ga)InAs QD	<ul style="list-style-type: none"> <li>• Low threshold current operation</li> <li>• <math>\lambda=1.3 \mu\text{m}</math> feasible</li> <li>• Small chirping</li> </ul>	<ul style="list-style-type: none"> <li>• Poor <math>T_o</math></li> <li>• No established growth technique</li> <li>• Small gain</li> <li>• Poor reproducibility</li> </ul>
GaAsSb/GaAs	<ul style="list-style-type: none"> <li>• <math>\lambda=1.3 \mu\text{m}</math> feasible</li> </ul>	<ul style="list-style-type: none"> <li>• Poor <math>T_o</math></li> <li>• No established growth technique</li> <li>• Difficult in MOCVD</li> </ul>
GaInAs/GaAs	<ul style="list-style-type: none"> <li>• Very high <math>T_o</math></li> <li>• Low threshold current density</li> <li>• High gain</li> </ul>	<ul style="list-style-type: none"> <li>• <math>\lambda &lt; 1.2 \mu\text{m}</math></li> <li>• Material degradation with high indium concentration</li> </ul>
GaInNAs/GaAs	<ul style="list-style-type: none"> <li>• Very high <math>T_o</math></li> <li>• <math>\lambda &gt; 1.3 \mu\text{m}</math> feasible</li> <li>• High gain</li> </ul>	<ul style="list-style-type: none"> <li>• High threshold current density</li> <li>• No established growth technique</li> </ul>
GaInNAsSb/GaAs	<ul style="list-style-type: none"> <li>• <math>\lambda \sim 1.55 \mu\text{m}</math> feasible</li> </ul>	<ul style="list-style-type: none"> <li>• High threshold current density</li> <li>• Complicated group V element control</li> </ul>

*Table 2. Comparison of laser materials in 1.2~1.6  $\mu\text{m}$  wavelength range*

Anan et. al. proposed GaAsSb/GaAs for long wavelength lasers in 1998 and realized 1.23  $\mu\text{m}$  CW operating VCSELs<sup>45</sup> and 1.3  $\mu\text{m}$  CW operation of edge emitting lasers<sup>46</sup>. The conduction band offset of GaAsSb/GaAs at 1.3  $\mu\text{m}$  is estimated to be only 35 meV, which is not enough to confine electrons into the quantum well and is a serious detriment to this material system.

Koyama et. al. proposed highly strained GaInAs/GaAs quantum well VCSEL with emission wavelength up to 1.2  $\mu\text{m}$ , and they predicted that the transmission

capability of a 1.2  $\mu\text{m}$  VCSEL through SMF would be better than a 1.3  $\mu\text{m}$  edge emitting lasers with MMF. However, this assumption is only valid when there is no appropriate 1.3  $\mu\text{m}$  gain material available for VCSELs.

The use of a dilute nitrogen semiconductor, either GaNAs or GaInNAs, was proposed by Kondow<sup>47</sup> in 1995. Kondow calculated the bandgap energy and band lineup of GaInNAs/GaAs based on dielectric band theory. The result predicts that 1.3  $\mu\text{m}$  emissions is possible by adding a small fraction of nitrogen into a strained GaInAs/GaAs quantum well and the conduction band offset of GaInNAs/GaAs is expected to be higher than that of InP-based material systems. They calculated the characteristic temperature,  $T_0$ , of GaInNAs/GaAs quantum well lasers to have a limit of 180 K.

Kondow et. al. realized the epitaxial growth of GaInNAs for the first time in 1997. However, the original crystal quality was relatively poor and the resulting threshold current density was as high as  $6.8 \text{ kA/cm}^2$ <sup>47</sup>. The problem in the GaInNAs/GaAs system was the lack of the well-established growth technique to obtain high quality crystalline material. The reported threshold current density of GaInNAs based lasers is higher than that of InP based lasers. A second problem was that as the material was pushed to longer wavelength, the threshold current density correspondingly increased. However, many research groups have investigated this new material, and the quality of the material has improved dramatically. The current state-of-the-art laser data shows comparable results to those of strained GaInAs/GaAs laser as will be discussed in later chapters.

In recent years, even more advanced materials with antimony were introduced by Ha et. al.<sup>4</sup> to further extend the wavelength of dilute nitride materials without a dramatic increase in threshold current density.

Among the new materials for long wavelength emission, GaInNAs and GaInNAsSb have more advantages than any other materials in realizing optical communication transmitters and Raman amplifiers to fully utilize the bandwidth of optical fiber from 1.28 to 1.61  $\mu\text{m}$ .

## 1.5 History of Dilute Nitride Compound Semiconductor for Lasers

Material properties of III-V-N type semiconductor alloys, such as GaNAs and GaNP, have been unclear because of its difficulty in crystal growth due to the large miscibility gap<sup>48</sup> caused by the large difference in the electro-negativities of nitrogen and arsenic or phosphorus. On the other hand, incorporation of nitrogen into GaP for doping purpose was well established using liquid phase epitaxy (LPE) for LEDs. In spite of the fact that GaP is an indirect bandgap material, GaP:N can emit with green light because nitrogen atoms form isoelectric traps that produce efficient radiative recombination. In the 1990's, MBE and MOCVD crystal growth techniques under highly non-equilibrium conditions were significantly improved and these techniques contributed to high quality III-V-N alloy growth. In 1992, Weyers et. al. succeeded in demonstrating MOCVD growth of GaNAs on GaAs substrate with the nitrogen composition up to 1.2%<sup>49,50</sup>. They observed a red-shift of the bandgap energy with increasing nitrogen composition by photoluminescence and absorption measurements. These results indicated that GaNAs alloys have a large bandgap bowing compared to conventional III-V semiconductors. In 1993, Sakai et. al. calculated the GaNAs bandgap energy using dielectric model<sup>51,52,53</sup> and predicted that the bowing parameter of GaNAs would be 23 eV. They also predicted large conduction band discontinuities for the GaNAs/GaAs hetero-interface. Kondow et. al. proposed the GaNAs alloy for long-wavelength optoelectronic device on Si substrate<sup>54</sup>. They also proposed GaInNAs alloys as an active layer material for thermally insensitive long-wavelength lasers<sup>55,56</sup>. Iga later proposed GaInNAs/GaAs long wavelength vertical-cavity surface-emitting lasers (VCSELs)<sup>57</sup> with the first long wavelength VCSEL demonstrated by Coldren. et. al.<sup>2</sup>.

## 1.6 Outline of the Dissertation

The outline of the dissertation following Chapter 1 is,

Chapter 2: Molecular Beam Epitaxy of GaInNAs and GaInNAsSb.

In this chapter, the growth of GaInNAs and GaInNAsSb by solid source molecular beam epitaxy (SSMBE) will be discussed. The fundamentals of the MBE system, MBE growth of basic GaAs based materials, and growth techniques for dilute nitride materials will be described. The optimum conditions for high quality material growth will also be discussed.

Chapter 3: Thermal annealing effects on GaInNAs and GaInNAs Sb quantum well.

In this chapter, the reason for the necessity of thermal annealing on dilute nitride material will be explained. Several phenomena related to thermal annealing will be presented.

Chapter 4: Characterization.

In this chapter, several methods for characterizing the new materials will be introduced. The fundamentals of these methods will be given as well as the data taken by these methods on our materials.

Chapter 5: GaInNAs and GaInNAsSb ridge waveguide edge emitting laser.

In this chapter, the fundamentals of the quantum well design and edge emitting laser will be discussed. The result of our lasers with new material will also be presented.

Chapter 6: Conclusion and Future Improvement.

In this chapter, the conclusions of this thesis will be given as well as suggestions on the future directions to improve the material quality for better performance device and exploration of additional new material systems.

## **Chapter 2: Molecular Beam Epitaxy of GaInNAs and GaInNAsSb**

**I**n this chapter, GaInNAs and GaInNAsSb growth by solid source molecular beam (SSMBE) will be discussed. First the background of molecular beam epitaxy (MBE) will be presented. This will include the nature of the elemental sources, in-situ monitoring, and growth mechanisms. Then, actual practice for the growth, including sample preparation, growth rate calibration and ordinary III-V growth including GaAs, AlGaAs, and GaInAs will be discussed. The growth challenges of GaInNAs and GaInNAsSb will be discussed. These subjects include the nitride-arsenide growth, generation of atomic nitrogen, control of nitrogen concentration, growth temperatures to avoid phase segregation, and optimization of constituent mole fractions. Then our approach to confront these issues will be introduced to achieve high quality material for optical devices.

### **2.1 Solid Source Molecular Beam Epitaxy (SSMBE)**

#### **2.1.1 Introduction**

Molecular beam epitaxy (MBE) was developed in the early 1970s as a means for growing high-purity epitaxial layers of compound semiconductors<sup>58,59</sup>. Since that time it has evolved into a popular technique for growing both elemental (Si and Ge) and III-V compound semiconductor alloys as well as several other materials. MBE can produce high-quality layers with very abrupt interfaces and good control of thickness, doping, and composition. Because of the high degree of control possible with MBE, it is an extremely valuable tool in the development and commercializing of complicated optoelectronic devices.

### 2.1.2 Fundamental Background of MBE

In MBE, the constituent elements of a semiconductor in the form of molecular beams are deposited onto a heated crystalline substrate to form epitaxial layers. This is schematically shown in Figure 16. The molecular beams are typically from thermally evaporated elemental sources, but other sources include metal-organic group III precursors (metal organic MBE or MOMBE), gaseous group V hydride or organic precursors (gas-source MBE or GSMBE), or some combination of these two (chemical beam epitaxy or CBE). To obtain high-purity epitaxial films, it is critical that the material sources be extremely pure and that the entire process be done in an ultra-high vacuum (UHV) environment, around  $10^{-9}$ ~ $10^{-11}$  Torr. Another important feature is that growth rates are typically on the order of a few Å/s and the beams can be shuttered in a fraction of a second, allowing for atomically abrupt transitions from one material to another.

Since MBE growth is carried out under high vacuum and thermodynamic non-equilibrium, this growth technique is mainly governed by the kinetics of the surface occurring when the incident beams react with the outermost atomic layers of the substrate

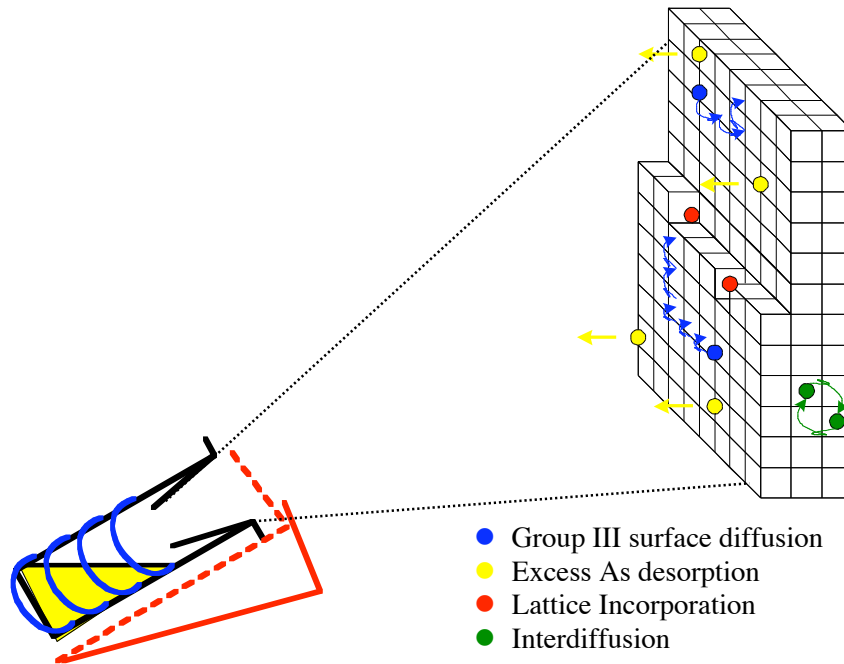


Figure 16. Schematic of MBE growth mechanisms.

crystal. A series of surface processes are involved in MBE growth. First the impinging molecules absorb on the surface through chemisorption for the group III atoms and physisorption for  $As_2$  and  $As_4$ . Under typical growth conditions, the group III atoms tend to have sticking coefficients close to unity; this allows precise control of the composition by the evaporation rate. The group III atoms migrate on the surface; a typical hopping rate is  $10^4$  hops/s. When the atoms find a low energy site, they may incorporate into the crystal lattice of the substrate. To obtain a smooth surface, the growth should occur in a layer-by-layer mode, and the ad-atoms should attach at ledges or kinks. Some of the supplied  $As_2$  will dissociate. The fact that the group V molecules are much more volatile than the group III atoms allows stoichiometric growth without precise control of the group V flux. If the substrate is sufficiently hot (typically  $\sim 600^\circ C$ ), the group V molecules will re-evaporate unless there is a group III atom with which to form the compound. Growth normally proceeds under arsenic rich conditions with V/III flux ratio of 10-25; much of  $As_2$  is desorbed from the surface. Since growth is performed at high temperature, some inter-diffusion of deposited species can occur.

### **2.1.3 Solid Source MBE Configuration for this work**

The Varian Gen II MBE system used for this work at Stanford University consists of five main vacuum chambers: a loading chamber, a buffer chamber (transition tube), a growth chamber mainly for distributed Bragg reflectors (DBRs) or cladding growth, a growth chamber mainly for dilute nitride growth, and a bake-out chamber. The loading chamber is used to bring samples in and out of the vacuum environment while maintaining the vacuum integrity of the other chambers. The buffer chamber or, so called, transition tube is used for transferring samples between two different growth chambers, storage, and *in-situ* optical measurement. The growth chamber for dilute nitrogen growth has a radio frequency nitrogen plasma source, and solid elemental sources of antimony, gallium, indium, aluminum, and both *n*-type (Si) and *p*-type (Be) doping sources. The growth chamber for DBRs or cladding growth is equipped with 2 gallium sources, 2 aluminum sources, and a  $CBr_4$  injector for high and sharp *p*-type doping and tunnel junctions. The advantage of having two growth-chambers linked by a

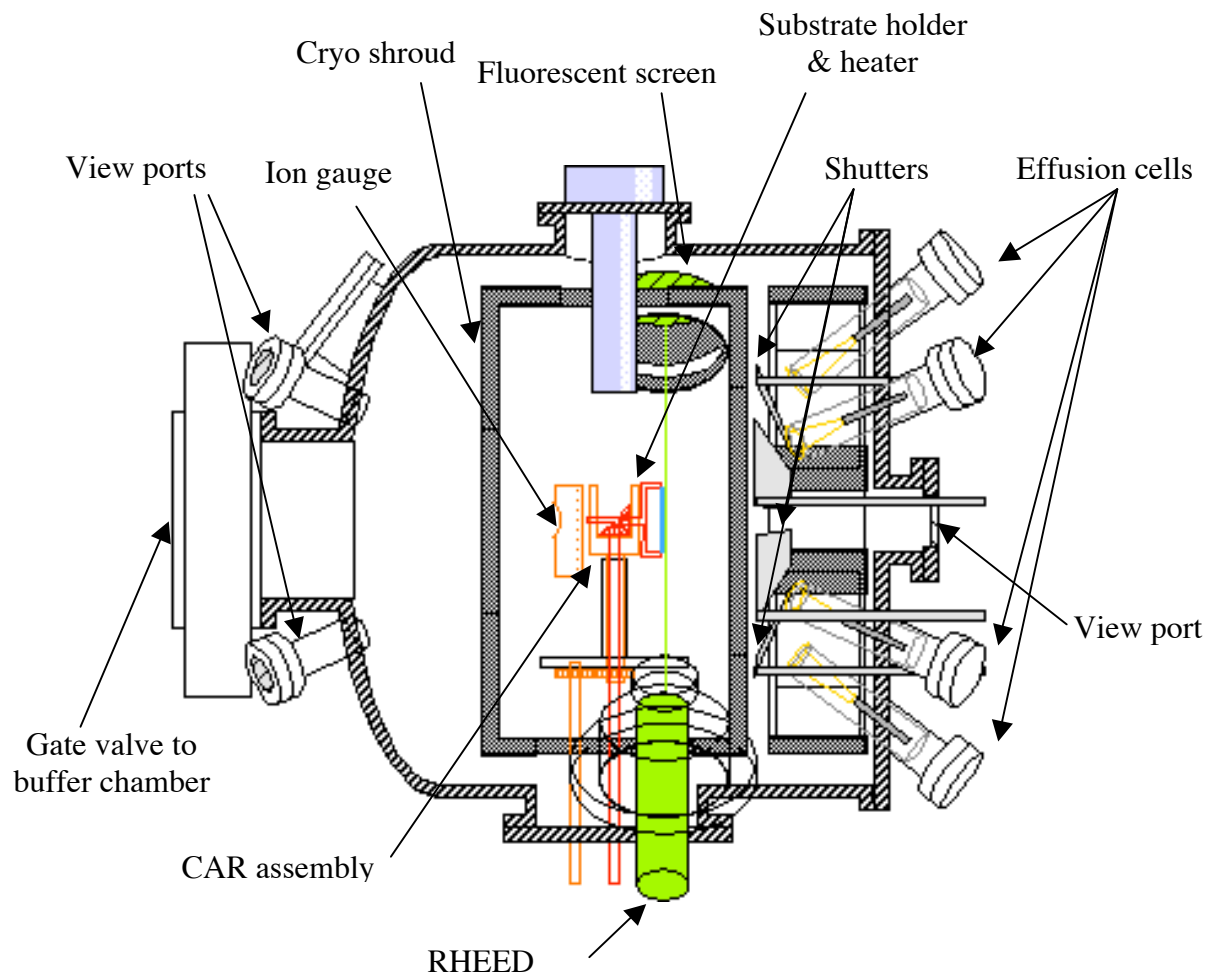


Figure 17. Schematic of MBE growth chamber and its parts.

buffer chamber under UHV is that both machines can be utilized at the same time and re-growing samples without exposing them to air.

The schematic of the growth chamber of a generic MBE system and its parts are illustrated in Figure 17. Samples are loaded onto the growth chamber sample holder/heater via a magnetically coupled transfer rod. The sample holder rotates on two axes as shown in Figure 17. Before growth, the sample holder is facing the loading position so that the ion gauge on the opposite side faces the material sources to measure beam equivalent pressure (BEP) from each elemental source to determine its growth rate. During growth, the sample holder rotates to face the sources and the ion gauge faces the buffer chamber. For improved layer uniformity, the sample holder is designed for continual azimuthal rotation (CAR) of the sample. A liquid nitrogen (77K) cooled cryo-

shroud is located between the outside chamber walls and the CAR and acts as an effective pump for many of the residual gasses in the chamber. Each growth chamber has one cryo-pump and one ion pump to remove gasses during growth. These two pumps can pump complementary species and keep the growth chamber pressure at under  $\sim 10^{-10}$  Torr. All parts that are heated are made of materials such as Ta, Mo, and pyrolytic boron nitride (PBN) which do not decompose or outgas impurities even when heated to 1600°C. To monitor the residual gasses, analyze the source beams, and check for leaks, a residual gas analyzer (RGA) is mounted in the vicinity of the CAR.

## **2.2 MBE Materials**

### **2.2.1 Elemental Sources**

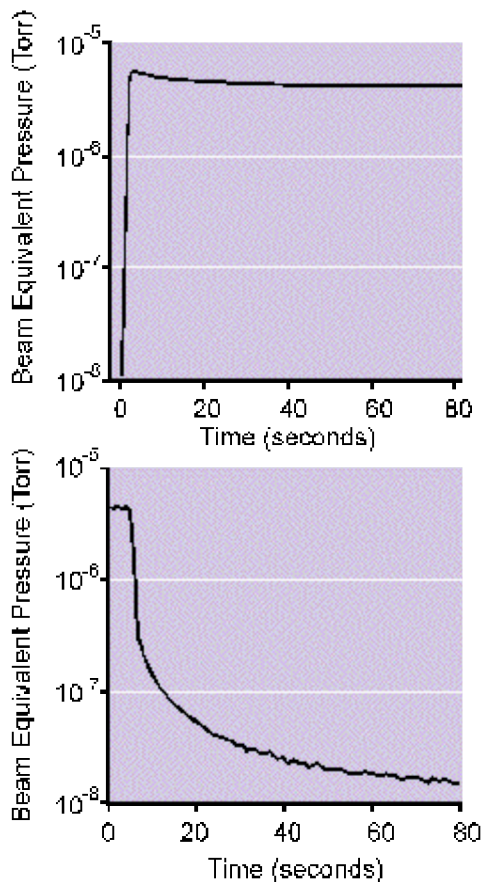
The MBE material sources, or effusions cells, are independently heated until the desired material flux is achieved. Changes in the temperature of a cell as small as 0.5°C can lead to flux changes on the order of one percent. To control thickness to better than 1%, highly stable control loops with Tungsten-Rhenium thermocouples and proportion, integral, and derivative (PID) controllers are used as well as a chilled source flange separating the cells to prevent thermal cross-talk. Computer controlled shutters are positioned in front of each of the effusion cells to be able to shutter the flux reaching the sample within a fraction of a second. Since conventional metal shutters in front of the effusion cells reflect some of the power back into the cell, opening the shutters is known to cause flux transients on the order of a few percent with a time constant of several minutes<sup>60,61</sup>. These transients are difficult to measure and depend on cell and system-specific factors such as the shutter type and location, heater element design, and thermocouple placement. To prevent these transient problems from affecting the growth, PBN shutters, which are transparent to heat, are used in our system. This PBN shutter is especially useful for the nitrogen plasma source since RF power can couple with a metal shutter and the shutter transients can cause plasma source instability.

The sources, except the nitrogen plasma source, are located approximately 10 cm from the sample in the growth position. The nitrogen plasma source is kept further from

the sample for improved uniformity. In production systems, which are designed for larger wafers and greater uniformity, this distance would be larger.

### 2.2.2 Arsenic Valved Cracker

As discussed previously, the sources in our systems are arranged specifically to grow arsenic containing compound semiconductors and dilute nitride materials. Because all the arsenic containing III-V materials are grown with 15 times arsenic over pressure and dilute nitride materials are grown under 20 times arsenic over pressure, the arsenic source should be much larger than other cells. As a result, it takes several hours for such a large arsenic source to reach the desired stable temperature. For that reason, the arsenic source used in our system is a valved-cracker<sup>62</sup>. The arsenic crucible and cracking zone are kept at high temperature and the flux is solely controlled by a mechanical valve, which eliminates the need of heating and cooling of the source for every growth. In our



system, the arsenic crucible is kept at 385°C, which provides, with full mechanical valve opening, more than 10<sup>-5</sup> Torr. With the mechanical valve closed, the arsenic flux drops under 10<sup>-11</sup> Torr, which lowers background pressures in the growth chamber and reduces coating of chamber walls and components. Figure 18<sup>63</sup> shows the arsenic pressure transition upon opening and closing the mechanical valve and the more important transition, mechanical valve opening, is fast enough to accommodate MBE growth. Since our MBE growth always needs arsenic flux, the rather slow closing transition is not a crucial problem. After passing through the mechanical valve, the arsenic flux moves through a cracking zone which converts the molecular species from

Figure 18. As pressure transition under opening and closing of mechanical valve.

As<sub>4</sub> to As<sub>2</sub>. One of the primary reasons for using As<sub>2</sub> instead of As<sub>4</sub>, is to reduce the consumption of As, which results in cost savings and less frequent refills, since As<sub>2</sub> incorporates more efficiently into arsenic containing material. It has also been suggested that using As<sub>2</sub> should result in better crystal growth since the incorporation mechanism is simpler than for As<sub>4</sub><sup>64</sup>. However, As<sub>2</sub>-grown layers also exhibit higher levels of shallow donors and are frequently intrinsically n-type. In order to determine the optimum cracking tube temperature, the mass spectra are recorded for As<sub>2</sub> (150 atomic mass unit) and As<sub>3</sub> (225 atomic mass unit). As<sub>4</sub> cannot be measured directly by mass-spectrometer because it is beyond the mass range of the mass spectrometer. The optimum cracking set point is chosen to be the temperature at which the As<sub>2</sub> to As<sub>3</sub> ratio no longer increases with increasing temperature. From the manufacturer's (Applied EPI) manual, the optimum cracking zone temperature corresponding to this point is 850°C. On an earlier cracker design, which used a hot filament, it was seen that higher cracker temperatures degrade the low temperature photoluminescence spectra from quantum wells, presumably because of increased impurities from the cracking filament. For the newer cracker design, which uses a heater element encapsulated in pyrolytic boron nitride (PBN), there is no significant degradation, either broadening or decreased intensity, in quantum wells except for samples grown with cracker set points above ~1000 °C.

### **2.2.3 Radio Frequency (rf) Nitrogen Plasma Source**

One of the most important sources in our MBE machine for the dilute nitride material growth is the nitrogen source. The details of the dilute nitrogen material growth will be discussed later. Several issues need to be considered for rf (13.56MHz) plasma cell. First, the equilibrium bulk solubility of nitrogen in GaAs is very low and nitrogen containing reagents are very stable. To allow the nitrogen to react and incorporate into the epitaxial layer, it is necessary to supply a very reactive nitrogen specie: atomic nitrogen. Atomic nitrogen is generated by rf plasma to minimize ion damage to the surface of the growth film<sup>65</sup>. The rf plasma source for this work was manufactured by SVT and originally designed to grow GaN at high nitrogen flow rates. Therefore, the exit aperture made of PBN of this source has been modified to allow plasma operation at low

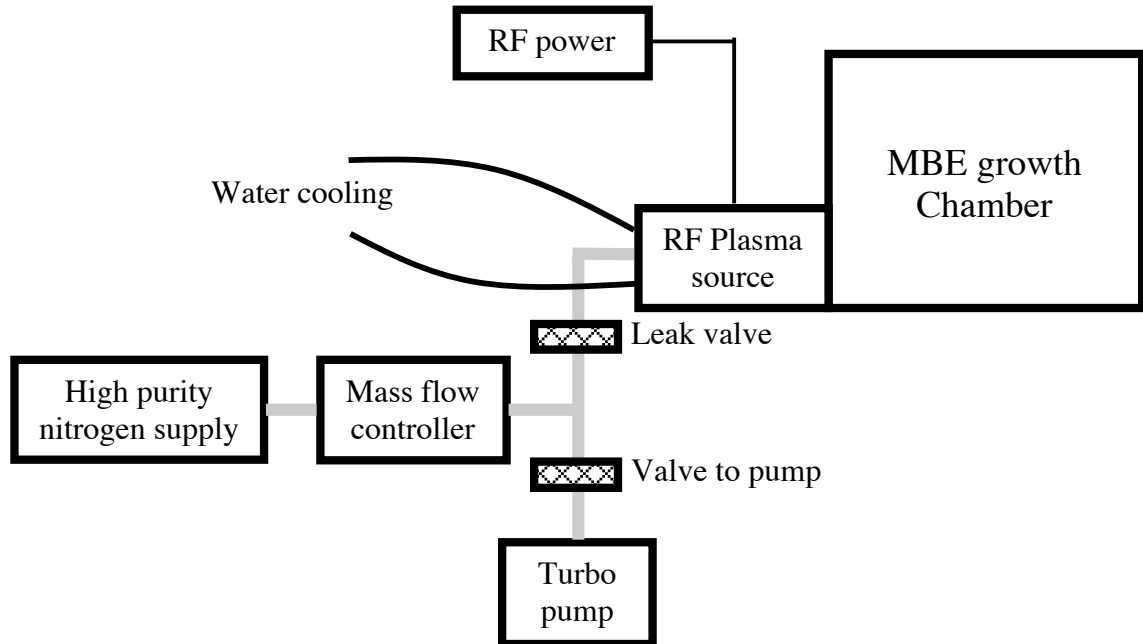


Figure 19. Diagram of the nitrogen plasma source configuration.

nitrogen flow rates (0.1-1 sccm) required to obtain nitride-arsenide with only a few percent of nitrogen. The size and number of holes in the aperture are based on the desired conductance to achieve enough pressure in the cell to ignite the plasma. The original plasma source had a PBN cover with nine  $\square=0.25$  mm holes and we found that 35% of incorporated nitrogen existed at interstitial sites<sup>67</sup>. This interstitial nitrogen caused excessive nitrogen out-diffusion from the quantum well and a blue-shift of emission after post-growth annealing. To reduce the interstitial nitrogen, the PBN cover was replaced with one with four  $\square=0.25$  mm holes. This decreased the conductance of the nitrogen flow to growth chamber and, to compensate, the injection of nitrogen flow was doubled from 0.25 sccm to 0.5 sccm. This plasma condition change increased the pressure inside the nitrogen plasma source and also decreased the mean free path of the ion and radical nitrogen, which in turn decrease the crystal damage. As a result, the interstitial nitrogen composition of total nitrogen concentration dropped to 4% and the material quality was improved<sup>66</sup>.

A nitrogen gas supply system has been built to control the flow of nitrogen into the MBE growth chamber as shown in Figure 19. The nitrogen mass flow controller, the valve to the turbo pump, and the leak valve to the MBE growth chamber control the

nitrogen flow into the growth chamber. The plasma operation is done in the following steps:

1. The nitrogen gas line to the mass flow controller is always open.
2. Start the backing pump (Tribodyne) for turbo pump.
3. When the pressure of the line between the backing pump and turbo reaches to 3 mTorr, open the valve between the turbo and backing pump and start the turbo.
4. Wait until the turbo reaches its maximum speed. This usually takes 20 minutes.
5. Open the valve to the turbo and open the mass flow controller.
6. Keep the nitrogen line purging through the turbo pump until plasma ignition.
7. Close the ion pump valve. The ion pump is not effective at pumping nitrogen and high nitrogen pressure in the growth chamber can shorten the pump life.
8. When the flow is stable, ramp the RF power slowly to 300 W. Using the matching box, control the reflected power to approximately 20 W.
9. Open the leak valve and close the valve to the turbo pump. Now all the supplied nitrogen flows into the growth chamber. When the pressure in the growth chamber is around  $10^{-5}$  Torr, the plasma ignites. However, because the pressure in the plasma source is high ( $\sim 10$  mTorr), the mean free path of the species is short and they do not have enough energy to form atomic nitrogen (low intensity plasma mode).
10. Decreasing the nitrogen flow to 0.1 sccm causes a sudden increase in the plasma intensity (high intensity plasma mode). Slowly increase the flow to 0.5 sccm with keeping the plasma at high intensity mode. Adjust the reflected power to 5-6 W. At this stage, the pressure in the plasma source is low enough and the mean free path of the nitrogen species is long enough to create atomic nitrogen. The pressure in the chamber drops.

This start-up procedure results in a peak profile for the nitrogen in the MBE chamber with the highest pressure when the plasma is ignited. The peak in the nitrogen pressure

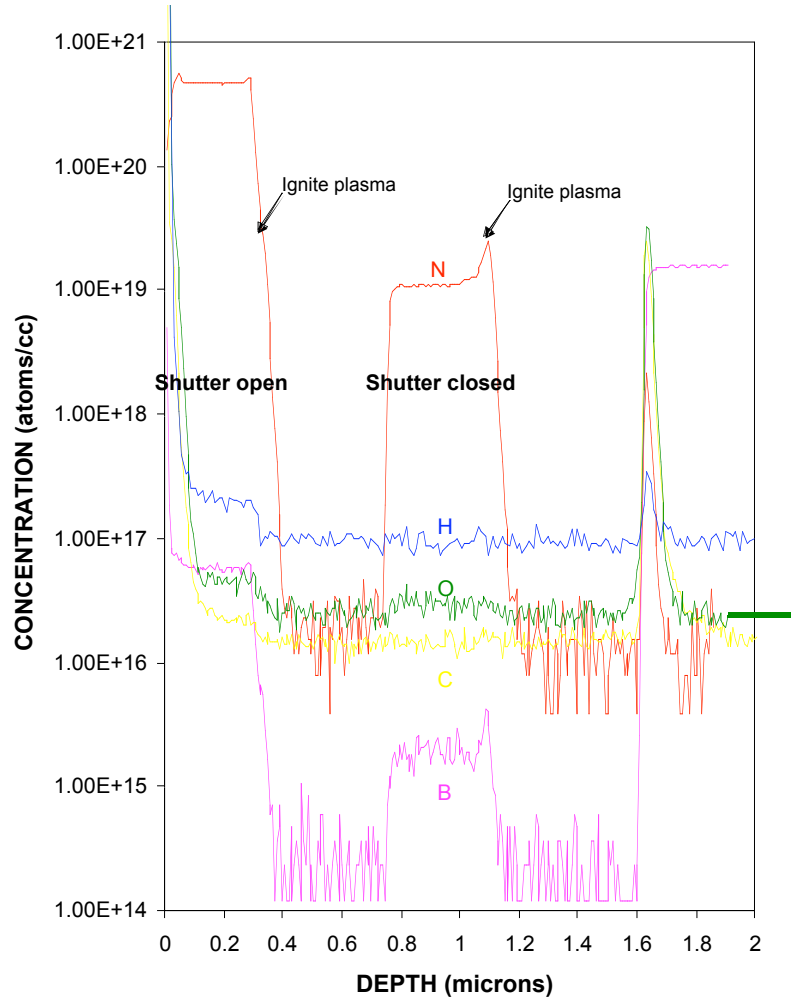


Figure 20. Nitrogen, Hydrogen, Oxygen, Carbon, and Boron concentration profiles measured by SIMS. The sample structure consist of a GaAs substrate, GaAs buffer layer, GaNAs layer grown with RF plasma running but the shutter in front of the source is closed, GaAs buffer layer, and GaNAs layer grown with RF plasma running and the shutter in front of the source is open.

results in a peak in the nitrogen concentration in the epitaxial film and this peak can be found from secondary ion mass spectrometry measurement (SIMS) (Figure 20).

The operation of the RF plasma has been optimized to maximize the generation of atomic nitrogen within the limits of stable plasma operation. The plasma conditions that maximize the amount of atomic nitrogen versus molecular nitrogen are determined using the emission spectrum of the plasma as shown in Figure 21<sup>67</sup>. The amount of molecular nitrogen is determined from the intensity of the first set of bands at approximately 550, 580, and 650 nm; the intensity in the bands at 740, 820, and 840 nm is proportional to the

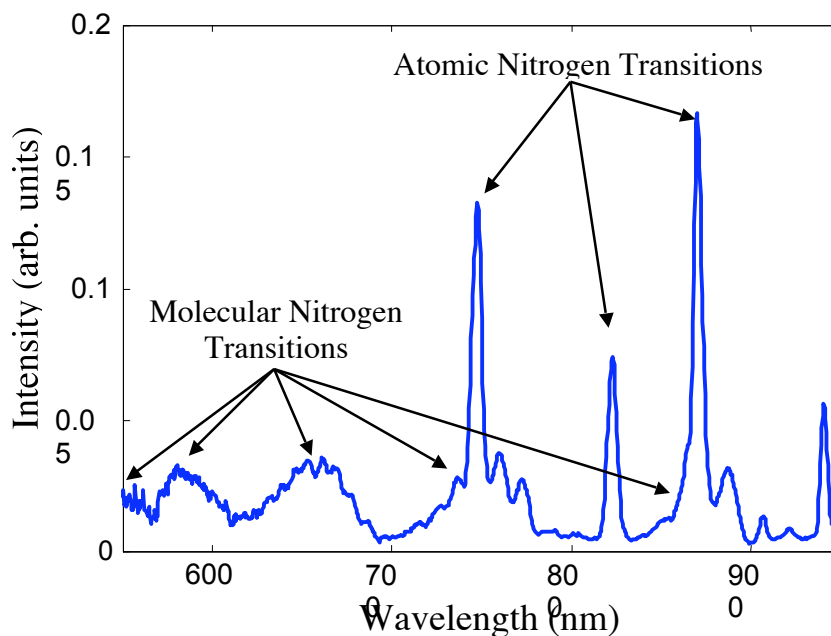


Figure 21. Emission spectrum of the RF plasma.<sup>65</sup>

amount of atomic nitrogen present in the plasma<sup>68</sup>. Hence the ratio of the peak intensity caused by an atomic nitrogen transition and the peak intensity caused by molecular nitrogen is proportional to the ratio of the amount of atomic versus the amount of molecular nitrogen in the plasma. The total intensity integrated from 550 to 950 nm is dependent on the total amount of active nitrogen in the plasma. The nitrogen flow rate of 0.5 sccm with 300 W RF power is the optimum point where the ratio of atomic versus molecular nitrogen is large and the plasma source is stable.

#### 2.2.4 Antimony Source

The antimony source used for this work is Applied EPI's standard cracking effusion cell. Like arsenic, antimony needs to be cracked from  $Sb_2$  to Sb to be efficiently incorporated into epitaxial film. Compared to arsenic, the kinetics of antimony on surfaces is relatively unknown but the basic mechanism is same as arsenic. The detailed role of antimony in GaInNAs growth will be discussed in chapter 2.6.3. The source has two zones; one is the sublimating zone and the other is the cracking zone. The temperatures of these two zones are controlled independently to prevent thermal crosstalk. Since our source is not a valved cracker, it needs to be heated every time

antimony is needed. To prevent condensation or clogging, the cracking zone is always heated first to 850°C. This temperature gives around 30% cracking efficiency and higher temperature above 1000°C will provide close to 100% cracking efficiency. However, we do not heat the cracking zone above 850°C based on the photoluminescence (photoluminescence) results that show lower photoluminescence intensity for the one grown under higher cracking temperature. This might be due to out-gassing from the metal crucible or condensed alien materials on the cracking zone. Metal crucibles can out-gas contaminants at high temperatures unlike PBN ones. Condensation can occur because without the valve, the cracking zone is exposed to growth chamber and the only cover is the shutter in front. The sublimator temperature is decided based on the flux required. To remove the condensed material on the cracking zone and stabilize the temperature, we wait about an hour before taking antimony fluxes. The antimony pressure range used for this work was  $7 \times 10^{-8} \sim 2 \times 10^{-7}$  Torr and the corresponding sublimator temperature range was 490°C~510°C.

## **2.3 *In-situ* Monitoring in MBE**

### **2.3.1 Introduction**

The ability to monitor the growth, determine the quality of material, and measure the optical properties is very important and powerful in MBE growth. This can reduce the growth calibration time, unnecessary unloading of samples from the machine, unnecessary exposure of grown samples to air, and so on. In this section, several *in-situ* techniques will be discussed.

### **2.3.2 Reflection High-Energy Electron Diffraction (RHEED)**

One of the most useful and common tools for *in-situ* monitoring of the growth is reflection high-energy electron diffraction (RHEED). It can be used to calibrate growth rates, observe removal of oxides from the sample surface, calibrate the substrate temperature, monitor the arrangement of the surface atoms, determine the proper arsenic overpressure, give feedback about surface morphology, and provide information about

growth kinetics. The layout of the RHEED system was shown in Figure 16. The RHEED gun emits  $\sim 10$  KeV electrons which strike the surface at a shallow angle ( $\sim 0.5$ - $2$  degrees), making it a sensitive probe of the semiconductor surface. Electrons reflect from the surface and strike a phosphor screen forming a pattern consisting of a specular reflection and a diffraction pattern which is indicative of the surface crystallography. A RHEED camera monitors the screen and can record instantaneous pictures or measure the intensity of a given pixel as a function of time, which is often used to calibrate the growth rate.

The appearance of the RHEED diffraction pattern can be used to provide qualitative feedback on surface morphology. If the surface is smooth, then the RHEED diffraction patterns appear streaky. If the samples are rough, then the horizontal streaks are more 'spotty' and the diffraction pattern is not as clear. An amorphous surface, such as an oxide layer, shows a haze instead of a diffraction pattern and polycrystalline surfaces result in rings circling the straight-through beam. Such information, although only qualitative, can be a useful check of the surface condition. In our setup, we calibrate the GaAs substrate surface temperature relying on the RHEED pattern changing from a hazy pattern to a streaky pattern based on the fact that the oxide on n+ GaAs evaporates under As overpressure at  $600^{\circ}\text{C}$ . Due to the heat conductance difference, semi-insulating type substrates have approximately  $50^{\circ}\text{C}$  higher deoxidation temperature,  $650^{\circ}\text{C}$ . This temperature calibration method can be used, since the deoxidation temperature depends primarily on the surface temperature and does not rely on the quality of the contact between the thermocouple and the block. There are still some uncertainties with this method. The transition from hazy to clear diffraction pattern is subjective, and also depends to some degree on the temperature ramp rate and nature of the initial oxide including oxide thickness. Also, as some GaAs wafer manufacturers use nitrogen-filled packaging, the thickness of natural oxide is too thin to be seen in RHEED. For this case, the RHEED pattern is already streaky before the substrate temperature reaches the deoxidation temperature. Therefore, we use this temperature measurement scheme as setting a reference point and offset the thermocouple reading accordingly, realizing that

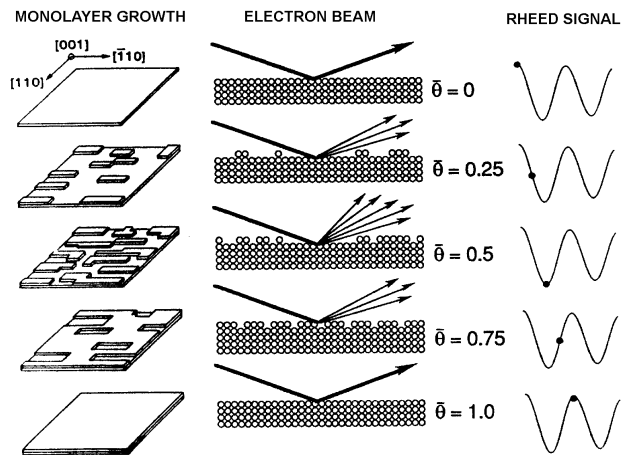


Figure 22. Illustration of the mechanism for RHEED oscillations during growth.<sup>70</sup>

although it is not completely accurate, this technique increases the repeatability of the temperature measurements.

Since we have two separate chambers for the DBR or cladding and the dilute nitrogen material, we often have to grow a sample in one chamber and transfer it to another chamber. RHEED pattern is always checked after transition and before the growth to find out the surface morphology and cleanliness.

### 2.3.3. RHEED Intensity Oscillation

RHEED intensity oscillations can be used as an accurate, quick, direct measure of the growth rates in MBE. When growth is initiated on a smooth GaAs surface, the intensity of the RHEED pattern, especially the specular reflection, starts to oscillate. The oscillation frequency corresponds to the monolayer growth rate<sup>69</sup>, where a monolayer (ML) is the thickness of one full layer of gallium and one full layer of arsenic atoms. The oscillations can be explained by a layer-by-layer growth mode as demonstrated in Figure 22<sup>70</sup>. When growth of a new layer starts, the surface is smooth and the specular spot of the RHEED pattern is bright, but as the layer nucleates, islands form on the surface, and the specular spot of the RHEED pattern dims. As the layer finishes, the islands coalesce into a flat layer, and the specular spot intensity increases. The oscillation of the specular spot intensity has been attributed to the oscillating roughness of the layers changing the diffuse scattering<sup>71</sup>, but the incident angle dependence of the oscillations<sup>72,73</sup> suggest that

interference between electrons scattering from the underlying layer and the partially grown layer contribute to these oscillations. Because the angle of the sample can vary due to wobble in the CAR, the position of the electron gun should be finely adjusted empirically to get the optimum incident angle.

There are several potential sources of inaccuracies from measuring the growth rates with RHEED. Because the RHEED oscillations damp, RHEED cannot be used for real-time growth rate monitoring, making it unable to detect changes in the growth rate during a run. In addition, RHEED must usually be done without rotating the sample. Without rotation, the growth rates are non-uniform across a sample. Measuring RHEED oscillations during rotation has been tried<sup>74</sup>, but this requires that the substrate rotate several hundred rotation per minute and complicated electronic setups are required so that the RHEED intensity is measured only when the sample is at a specific azimuthal angle. In spite of these uncertainties, the use of RHEED oscillations to measure growth rates is still very useful and can give reproducible layer thickness to within a few percent.

#### **2.3.4 Normal Incidence Reflectivity Oscillations**□

There are other *in-situ* tools capable of measuring the growth rate accurately including pyrometric interferometry<sup>75</sup>, optical flux monitoring<sup>76</sup>, ellipsometry<sup>77,78</sup>, and normal incidence reflectometry<sup>79,80</sup>. In order to get more accurate layer thicknesses normal incidence reflectometry is used. This measurement can be done both during growth and after growth. The real-time measurement system we have at Stanford is SVT's In-Situ 4000 Process Monitor model. This setup has two independent optical reflectometers using both long (950 nm) and short (470 nm) wavelengths. The measured reflectance is analyzed by software algorithms to provide thickness, growth rate, and refractive index measurement in real-time. To utilize this setup in the growth chamber, there should be a port facing the substrate, as there is in Varian Gen II systems, and a heated-viewport to prevent the viewport from getting coated. The heated viewport needs to be heated to at least 200°C. If the viewport accidentally gets coated, then heating to about 300°C for a couple hours is usually sufficient to clean it. The post growth reflectivity measurement setup is depicted in Figure 23. Light from a tungsten lamp is

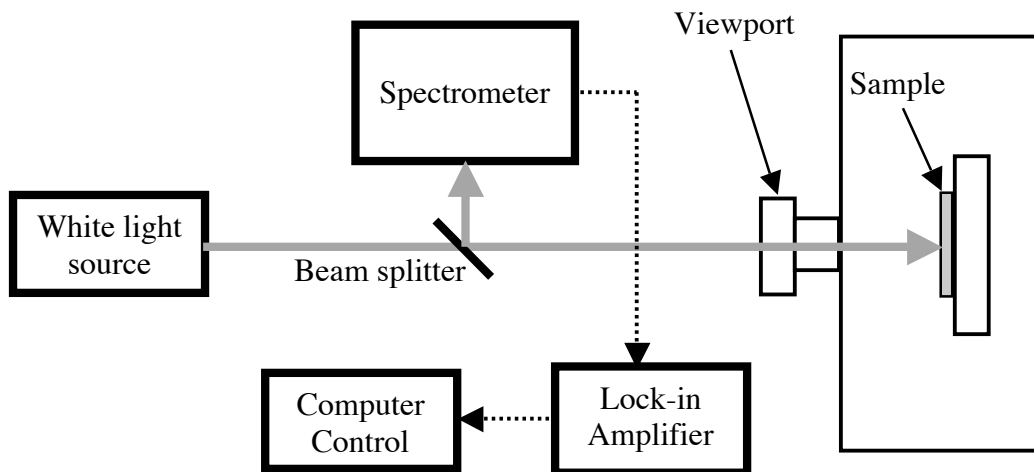


Figure 23. Illustration of the setup to measure surface normal reflectance of a sample post epitaxial growth.

directed into a fiber. A lens focuses the light and directs the light through the viewport to the sample. The distance from the lens to the sample is about 20 cm, and the spot size is about 1 cm in diameter at the sample. The reflected light passes back through the viewport and lens, into a fiber and then reflected from a 50/50 beam splitter and fed into an optical spectrometer where the photodetector is located.

Reflectometry can be used to monitor the growth if the structure contains layers of different materials. In such a case, interference from the light reflecting from different interfaces will affect to the overall reflectivity. As the layers grow, the interference conditions change, causing the sample reflectivity to oscillate with a frequency determined by the growth rate, the incident wavelength, and refractive index of the layers. Reflectometry can be used either to pre-calibrate the growth rates on a separate sample or to monitor growths in real time. Our reflectometry system has wobble filtering software, thus the problems resulting from wobbles in the CAR are not issues. Using reflectometry instead of RHEED for pre-calibration, an average growth accuracy of 0.25% is reported<sup>81</sup>, indicating that this technique can give accurate results. Much of that error is attributed to an uncertainty in the growth temperature of  $\pm 20^\circ\text{C}$ , so with good control of temperature and accurate knowledge of the indices of refraction at elevated temperatures, flux non-uniformity and long-term flux drift would be the limiting factors on the growth accuracy. However, measuring the growth rate once can take about 10-20

minutes compared to 30 seconds for RHEED oscillations. Although it is very accurate at measuring the growth rate, it is impractical to use reflectance oscillations as feedback for adjusting the growth rates to a specific value, for example to achieve a desired alloy composition.

Monitoring the post-growth sample is appealing especially for VCSEL growth, since if there is any cavity peak shift, the measurement result can be used to compensate for this unexpected error. This post growth reflectivity measurement is done after the bottom DBR growth to check the reflectivity peak of bottom DBR and, if there is error, additional layers can be grown to compensate for this offset. After the active layer and two or three pairs of DBRs, another reflectivity measurement is done to check the cavity dip wavelength, where the gain medium bandgap energy is, and the dip should be at the middle of reflectivity bandwidth, where the reflectivity is maximum. If any error is found, additional layer can be grown to compensate for it.

### **2.3.5 Beam Equivalent Pressure (BEP)**

Calibration of the growth rate is essential the MBE growth since one of the advantages over other growth techniques is accurate control over epitaxial film thickness and distinct interfaces between two different layers. Some of the *in-situ* techniques which can be used in MBE were introduced in previous chapters. Another way to measure the growth rate is to use the BEP gauge. This measurement is dependent on factors such as the geometry of the system and ionization efficiency of the material being measured, but for a given system and material, the BEP reading is proportional to the flux at the sample surface and hence the growth rate. Unlike other techniques available, BEP measurements do not require any pre-grown epitaxial layers. Growing epitaxial layers requires an approximate knowledge of the flux beforehand, so the BEP is particularly useful for effusion cells which are being used for the first time. There are limitations to this technique, however. It is not a direct measure of the growth rate, so some other *in-situ* or *ex-situ* technique must still be used to relate the BEP to a growth rate. In our system, a few samples are grown under certain BEP and the grown film thickness measured by *ex-situ* methods including spectrophotometer measurement and ellipsometry. These data sets

are recorded in a data sheet and on a computer for analysis and to be used for further growth. The ion gauge for BEP measurement in MBE can only measure the rates to within several percent. The biggest difficulty, however, is that while measuring the flux of a group III component, the ion gauge gets coated, causing a rapid loss of sensitivity in the gauge. However, the gauge sensitivity will eventually recover if it is left running under an arsenic overpressure, and after measuring the flux, all the shutters are kept closed for 10 minutes to help the ion gauge recover its sensitivity.

## **2.4 Sample Preparation**

A clean surface is an important prerequisite for epitaxial growth, since contaminants from the atmosphere or other sources can easily not only contaminate a clean GaAs wafer and cause crystal defects thereby degrading the optical and electrical characteristics of the epitaxial layer, but also the growth chamber and the elemental sources. Auger electron spectroscopy was an essential tool for determining wafer cleanliness as MBE was being developed<sup>58</sup>, but most GaAs wafer vendors currently supply ‘epi-ready’ wafers which are pre-cleaned and oxidized in a controlled environment. The oxide forms a protective layer which can be removed inside the growth chamber. The use of such epi-ready wafers has led to consistent results without the need for elaborate wafer cleaning procedures.

The new wafer holder with a sapphire heat-diffuser from Applied EPI can handle full 2” and 3” wafers and their quarter sizes respectively. A quarter-size sample is cleaved from a whole wafer and loaded into wafer holder with special inserts. These quarter size samples are particularly suitable for measurements that only require small area. All samples on wafer holders are cleaned by high-pressure nitrogen gun to remove dust from their surfaces. The mounted samples are then put into the loading chamber and baked at 200°C for several hours to remove water from substrates, holders and the transition trolley before being moved into the buffer chamber. During this initial baking, the loading chamber is pumped by a cryo pump down to  $\sim 10^{-8}$  Torr. After being moved into buffer chamber, substrates are out-gassed at 400 °C for 1 hour before they are moved

into the growth chamber. After a sample is loaded into the growth chamber and rotated to face the sources, the RHEED pattern will be hazy, which is indicative of the amorphous nature of the protective oxide. The substrate temperature is ramped up, with an arsenic overpressure of normally  $10^{-6}$  Torr, until diffraction pattern appears, showing that the protective oxide has desorbed from the surface. The temperature of the substrate is monitored using a spring-loaded thermocouple in direct contact with the molybdenum block. Since our MBE system has a heated viewport facing the sample in the back, an optical pyrometer can be used to measure the temperature. With the current setup, however, in order to get enough signal from the sample for a reliable pyrometer measurement, the substrate temperature must be  $\sim 600^{\circ}\text{C}$  or higher. After RHEED shows that the oxide is completely removed, the sample temperature is increased  $30^{\circ}\text{C}$  for 10 minutes to ensure that all traces of the oxide are removed.

## 2.5 Epitaxial Growth of GaAs based Material

During MBE growth, when molecules arrive at the substrate, they can migrate on the surface, interact with other atoms, incorporate into the crystal, or desorb as shown in Figure 16. The primary controllable factors that affect this process are the morphology of the surface, the temperature of the substrate, and the incident fluxes. At typical substrate temperatures used for growth of GaAs ( $\sim 580^{\circ}\text{C} \sim 650^{\circ}\text{C}$ ), arsenic preferentially desorbs from the surface, requiring an arsenic overpressure to prevent the surface from becoming gallium rich. It was also noticed early in the development of MBE<sup>82</sup> that the presence of gallium ad-atoms on a GaAs surface greatly increases the adsorption rate of  $\text{As}_2$ . The sticking coefficients of arsenic species are proportional to the gallium flux and approach 1 for  $\text{As}_2$  or 0.5 for  $\text{As}_4$ <sup>63</sup>. The dependence of the arsenic sticking coefficient on the presence of a group III molecule enables the films to grow stoichiometrically over a relatively large range of substrate temperatures and arsenic overpressures.

At substrate temperatures up to  $\sim 650^{\circ}\text{C}$ , the sticking coefficient of gallium on GaAs is near unity. The sticking coefficient of aluminum on  $\text{Al}_x\text{Ga}_{1-x}\text{As}$  is near unity even above  $700^{\circ}\text{C}$ . However, indium desorbs easily at high temperature, reducing the

indium concentration in the epitaxial layers for high temperature growth. Therefore, our  $\text{Ga}_x\text{In}_{1-x}\text{As}$  growth temperature is typically around  $450^\circ\text{C}$ . With unity sticking, the growth rates of each group III constituent are determined primarily by the BEP of each cell, which is directly related to the temperatures of the effusion cells. It is therefore relatively straightforward to control the growth rates and determine the alloy composition once the growth rate for each group III is calibrated well. However, if the substrate temperature during growth exceeds the unity sticking temperature range, then the sticking coefficients of the group III ad-atoms can depend on the As overpressure, the substrate temperature, and the alloy composition<sup>83,84</sup>.

The surface mobility of the group III ad-atoms plays an important role in the morphology and quality of the layers. If the ad-atoms are able to diffuse to steps on the surface, where they incorporate preferentially, then the growth surface will be nearly layer by layer. The group III surface mobility of ad-atoms is affected by the group III species, the substrate temperature, the surface on which the ad-atoms are moving, and the group V overpressure. Higher substrate temperature and lower group V (arsenic for our case) flux both result in higher surface mobility. This tendency would imply that higher substrate temperatures and lower group V fluxes should produce smoother layers as long as the group V flux is sufficient to maintain proper stoichiometry. An improvement in smoothness with increased temperature is supported, for example, by observations of improved mobility in inverted HEMTs grown at higher temperatures<sup>85</sup>. When growing GaAs, there is a large window for which there is both unity sticking and sufficient mobility. When growing ternary or quaternary compounds, the window of good growth conditions becomes significantly smaller because of the differences in the relative bond strengths of the different group III ad-atoms. Surface mobility is not the only factor important for good morphology, however. The growth of AlAs at  $600^\circ\text{C}$  is smooth and shows strong RHEED oscillations, even though the mobility of the Al ad-atoms is significantly less than the mobility of the gallium ad-atoms. Despite smooth morphology for growth with substrate temperatures of  $\sim 600^\circ\text{C}$  and  $\sim 700^\circ\text{C}$ , high Al content ( $x > 0.4$ )  $\text{Al}_x\text{Ga}_{1-x}\text{As}$  layers show increased roughness when grown in the temperature range of  $630^\circ\text{C}$ - $690^\circ\text{C}$ <sup>86</sup>. We generally grow  $\text{Al}_x\text{Ga}_{1-x}\text{As}$  at  $\sim 600^\circ\text{C}$  and  $\text{Ga}_x\text{In}_{1-x}\text{As}$  at  $\sim 450^\circ\text{C}$

(calibrated by surface oxide desorption temperature as previously discussed), because it results in good material for the entire range of compositions and maintains unity sticking conditions for the group III components.

RHEED can be used to determine the minimum amount of arsenic required to maintain the proper stoichiometry by measuring the incorporation ratio. This measurement starts with a sample at the growth temperature under an arsenic flux, ensuring that the surface is arsenic-terminated. The arsenic shutter is closed and the gallium shutter is opened for a few seconds, causing the surface to become gallium terminated and the RHEED pattern to change. The arsenic shutter is then reopened with the gallium shutter still open and the time required for the surface to recover is recorded. If the RHEED never recovers, then the arsenic flux is too low. If it changes back very quickly then the arsenic pressure is probably too high and the mobility of the group III ad-atoms will be too low. An incorporation ratio can be expressed as the total time the gallium shutter is open until the surface recovers divided by the time it takes for the surface to recover after the As shutter is reopened.

$$\frac{\boxed{\text{As}}}{\boxed{\text{Ga}}} \Big|_{\text{incop. ratio}} = \frac{t_{\text{Ga\_open}}}{t_{\text{As\_open}}}$$

Values of the incorporation ratio of 1.3 to 1.8 typically yield good results for GaAs and AlAs. The arsenic flux can then be measured with the BEP gauge, and in subsequent runs with the same substrate temperature and growth rate, the arsenic flux can quickly be set to the same BEP without needing to re-measure the incorporation ratio. The dependence on a small displacement of the filament highlights the fact that BEP measurements are system dependent and that a system independent measurement, such as an incorporation ratio, is a better absolute gauge of the growth conditions.

If a smoother morphology is desired, but the growth temperature cannot be increased, there are other ways of improving roughness. Growing the layers more slowly allows more time for the ad-atoms to move on the surface and can thus lead to smoother films at low temperatures<sup>87</sup>. Slow growth rates, however, are impractical for thick layers and will also lead to an increased background impurity concentration. For improved interface smoothness, pausing growth at the interface can be used<sup>88,89</sup>, but lengthy pauses

can be a problem at critical layers since background impurities will accumulate at the interface. Because the diffusion length of a group III ad-atom can be more than an order of magnitude larger when no arsenic overpressure is present, modulating the arsenic and group III fluxes can enhance the ad-atom mobility during epitaxial growth and has thus been termed migration enhanced epitaxy (MEE)<sup>90</sup>. In addition to MEE, which is often avoided because the rapid shuttering is hard on the effusion cell shutters, the use of substrates that are cut a few degrees off axis has been shown to improve surface morphology<sup>91</sup>. The surface of an off-axis substrate has higher density of surface steps and thus decreases the distance that ad-atoms must diffuse to reach a step edge. Because of the high density of step edges, much of the growth occurs by step propagation, which cannot be monitored by RHEED oscillations. Different crystal orientations have different growth characteristics and are of some interest, but (100) is the predominant substrate orientation for dilute nitrogen materials and other quantum well devices because it produces good quality epitaxial layers and is free from the anti-phase, twinning, and faceting defects present common in epitaxial layers grown on the (111)A, (111)B, and (110) surfaces.

At reduced substrate temperatures and/or increased arsenic overpressures, the surface becomes arsenic-rich and changes to a (2x2) reconstruction. This transition can be used to glean some useful information about the growth conditions. The specular spot on arsenic-stabilized (2x4) surfaces starts oscillating at its brightest intensity. When growth is started on an arsenic-rich (2x2) surface, the specular spot intensity is initially dim and gets brighter as the surface changes back to an arsenic-stabilized (2x4) form. Because the arsenic-rich surface is a steady-state condition and since the arsenic overpressure can be measured precisely for a given system geometry, the onset temperature of the arsenic-rich surface can be used as a precise ( $\sim 5^\circ\text{C}$ ), repeatable temperature reference that is less subjective than determining the oxide desorption temperature with RHEED.

## 2.6 GaInNAs and GaInNAsSb growth

The growth of nitride-arsenide alloys is different from that of ordinary arsenide materials. Part of this difference comes from the very different properties of nitrogen and arsenic atoms (Table 3) and nitride and arsenide binaries (Table 4). One of the key issues for growing high quality dilute nitrogen material is to prevent phase segregation caused by these differences.

As shown in Table 3, nitrogen has a smaller atomic radius than arsenic. Since these are isoelectric atoms, the difference in size results in a larger electro-negativity for nitrogen. These differences between nitrogen and arsenic atoms explain the differences between nitrides and arsenides. These differences are: nitrides have wurtzite crystal structure and arsenides have zincblende crystal structure, arsenides have a bigger lattice constant than nitrides, which makes the arsenides have a smaller bandgap, arsenides also have a smaller enthalpy of formation.

Due to these differences, there are many growth challenges in this nitride-arsenide material system. It can be compared to mixing oil and water. In this chapter, the details of

	N	As
Atomic Number	7	33
Non-Polar Covalent Radius	0.75 Å	1.18 Å
Electro-Negativity	3.05	2.18

*Table 3. Properties of nitrogen and arsenic.*

	GaN	GaAs	InN	InAs
Crystal structure	Wurtzite	Zinc-Blende	Wurtzite	Zinc-Blende
Lattice Parameter (Å)	a = 3.18 c = 5.16	a = 5.65	a = 3.54 c = 5.70	a = 6.05
Energy Gap (eV)	3.44	1.428	2.07	0.358

*Table 4. Properties of nitrides and arsenides.*

the GaInNAs and GaInNAsSb growth will be discussed including the optimum growth conditions for high quality material that is suitable for optoelectronic device applications.

### **2.6.1 Nitrogen Concentration**

The rf plasma nitrogen operation and growth conditions used for this work are as following:

1. Nitrogen flow rate: 0.25 sccm ~ 0.5 sccm
2. RF plasma power: 300 W
3. Substrate temperature: 205°C below deoxidation temperature and this is approximately 400°C.
4. Group III growth rate: 0.5 um/hr.
5. The As<sub>2</sub> pressure is maintained 20 times higher than total group III flux.

Since all other parameters nitrogen source (i.e. nitrogen flow rate, rf power, reflected power, As<sub>2</sub> pressure, growth temperature) are optimized to achieve stable plasma, the best material characteristics (highest photoluminescence intensity and smallest FWHM), and maximum nitrogen incorporation, the only parameter for controlling the nitrogen concentration is the group III growth rate. It is well known that nitrogen concentration is inversely proportional to growth rate<sup>67</sup>. This is a reasonable hypothesis for dilute nitrogen material since the available atomic nitrogen in the growth chamber is stable under the constant plasma condition. This premise can be understood as following: when the growth rate is low, the ratio of available atomic nitrogen to group III species is higher and this increases the high nitrogen concentration in the epitaxial film and vice versa. This is advantageous for GaInNAs compared to the Arsenide-Phosphide system where the group V flux control is very crucial and strongly temperature dependent. High-resolution x-ray (HRXRD) measurements support this theory as shown in Figure 24. This result shows that the nitrogen concentration versus inverse group III growth rate is linear and the relation can be expressed as,

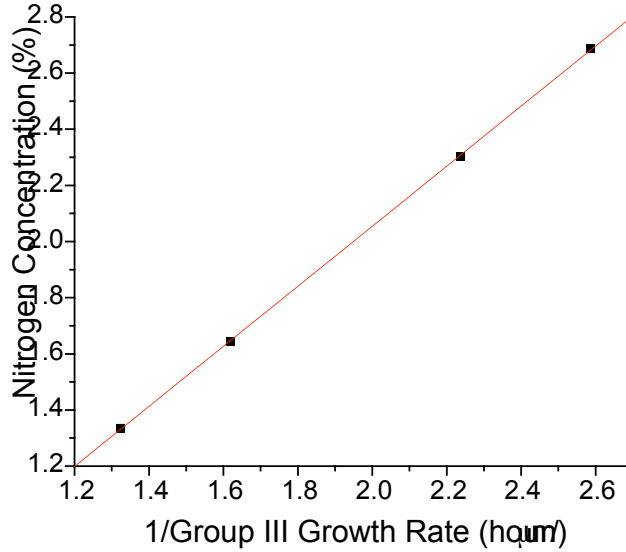


Figure 24. Group III growth rate versus nitrogen concentration.

$$\text{Nitrogen concentration}(\%) = 1.0694 / \text{Growth rate}(\mu\text{m} / \text{hour})$$

From the equation above, it can be found that under our ordinary group III growth rate of 0.5  $\mu\text{m}$ , this yields approximately 2.1 % nitrogen incorporation in the epitaxial film.

### 2.6.2 Miscibility Gap in Dilute Nitride Material

As shown in Table 3 and 4, there are many differences between the two isoelectronic nitrogen and arsenic atoms and, hence, between nitrides and arsenides. This large difference causes a large miscibility gap, which made it difficult to grow III-V-N alloys over any useful composition region for a long time. In this chapter, a simple calculation to the estimate upper limit for the miscibility of GaAs and GaN will be performed, rather than deriving a complicated phase diagram equation already done by Spruytte<sup>67</sup>.

In the case of a cubic lattice, the lattice constant of GaAs (5.653 Å) is over 10% larger than that of GaN (4.520 Å). Thus, the strain-induced energy from the deformation of the bond angle and/or the bond length needed to form a uniform alloy is quite large.

This excess internal energy equals to an increase in the enthalpy  $\Delta H^M$  of mixing. Here excess enthalpy  $\Delta H^{GaNAs}$  can be defined as,

$$\Delta H^{GaNAs}(x) = E_{tot}^{GaNAs} - xE_{tot}^{GaN} - (1-x)E_{tot}^{GaAs}$$

where  $x$  is the nitrogen mole fraction in  $GaN_xAs_{1-x}$  system.  $E_{tot}^{GaNAs}$  is the total energy per atom for the GaNAs alloy structure and  $E_{tot}^{GaN}$  and  $E_{tot}^{GaAs}$  are the total energies for binary GaN and GaAs, respectively.

Calculation of the excess enthalpies can be used to construct a lower limit  $\Delta H_{min}(x)$  for each composition,

$$\Delta H_{min}(x) = 4x(1-x)\Delta H_0$$

with  $\Delta H_0 = 199$  meV is a lower limit for all calculated excess enthalpies<sup>92</sup>. The equation above gives the spinodal line which divides the metastable and unstable region. Using this relation, the miscibility gap can be calculated analytically. The entropy is estimated within a mean-field approximation, giving an upper limit of:

$$S(x) = \Delta k_B [x \ln x + (1-x) \ln(1-x)]$$

where  $k_B$  is the Boltzman constant. The free energy becomes,

$$G(x, T) = \Delta H_{min}(x) - TS(x)$$

The miscibility gap as a function of temperature is then given by the binodal line<sup>92</sup>, which divides the stable and metastable region:

$$k_B T / \Delta H_0 = (8x - 4) / [\ln x - \ln(1-x)]$$

Figure 25 shows the lower limit of the miscibility gap (binodal line, dashed curve) and spinodal line (solid line) for  $GaN_xAs_{1-x}$ . The critical temperature, above which complete miscibility is possible, is  $T_{critical} = 2\Delta H_0 / k_B \approx 4611K$ . In the case of MOCVD and MBE growth, a composition within the miscibility gap can be grown under metastable conditions because crystal growth is performed under non-equilibrium conditions.

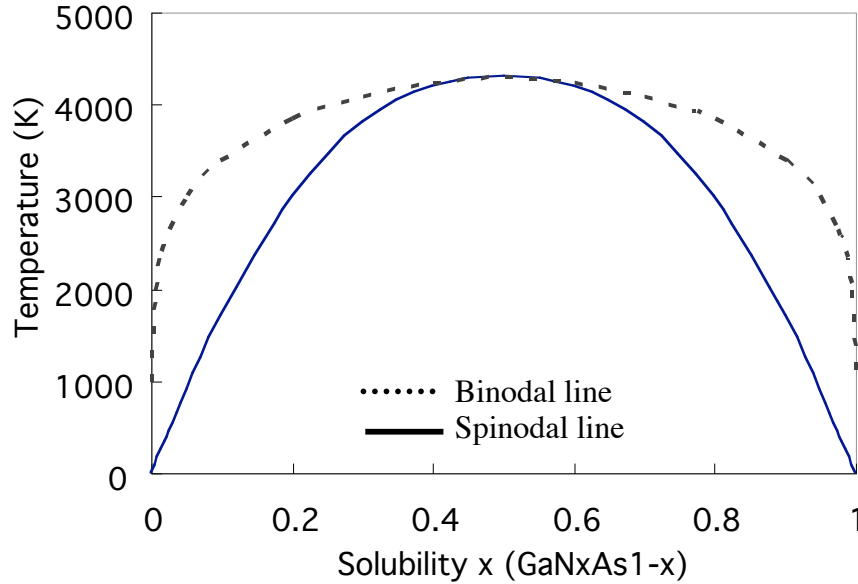


Figure 25. Miscibility gap calculation of free-standing  $\text{GaN}_x\text{As}_{1-x}$  alloy. Binodal line (dashed) indicates the lower limit of miscibility gap which divides stable phase and metastable phase. Spinodal line (solid) indicates the division of the phase between metastable and unstable.

The solubility of compound semiconductors can be estimated by applying regular solution approximation.  $\Delta H^{\text{GaAs}}$  can be written as,

$$\Delta H^M(x) = \Omega x(1-x)$$

where  $\Omega$  is interaction parameter calculated by the delta lattice-parameter (DLP) model<sup>48,93</sup> based on a lattice mismatch between two binary materials. A interaction parameter,  $\Omega$ , which is a good index of the strength of immiscibility, is given by,

$$\Omega = 4K \frac{\Omega}{2} (a_A^{2.5} + a_B^{2.5}) \left[ \frac{a_A + a_B}{2} \right]^{2.5}$$

where  $K$  is a constant and  $a_A$  and  $a_B$  are the lattice constants of components A and B, respectively. Assuming that  $K = 1.15 \times 10^7 \text{ cal/mol-}\text{\AA}^{2.5}$ , which has been widely used for ternary alloys with zincblende structures, and converting the lattice constant of the wurtzite to that of the zincblende structure. At a temperature of  $T$ , solubility  $x$ , assuming  $x \ll 1$ , can be determined from the interaction parameter  $\Omega$ ,

$$x = \exp\left(\frac{\Omega}{RT}\right)$$

where  $R$  is the gas constant. The interaction parameters,  $\Omega$ , for various ternary compound materials are shown in Table 5. GaInAs alloy has a solubility of over 1% at room temperature. On the other hand, a GaNAs alloy has a solubility of only  $10^{13} \text{ cm}^{-3}$  even at 800°C. Furthermore, structural difference between wurtzite and zincblende may contribute to the solubility of GaNAs higher. This result indicates that the crystal growth of GaNAs alloys is difficult in thermal equilibrium. Thus, a non-equilibrium growth method such as MBE, CBE, and MOCVD is needed to grow.

III-V Ternary alloy system	Lattice mismatching from GaAs, $\Delta a/a$ (%)	Interaction parameter $\Omega$ (DLP model) (kcal/mole)
GaInAs	7.2	2.815
GaInP	7.1	3.63
GaNAs	20	42.78
GaNP	18.9	28.90
AlNAs	22.3	57.93
AlNP	19.5	45.53
InNAs	17.3	26.71
InNP	14.6	19.68

Table 5. Lattice mismatches and interaction parameters for various III-V ternary alloy systems<sup>48</sup>

### 2.6.3 Antimony as a Surfactant

To push lasing wavelength beyond 1.4  $\mu\text{m}$ , while maintaining low threshold current, it is desirable to increase indium while minimizing nitrogen compositions. The problem with high indium compositions is that the growth goes from 2D to 3D with the formation of “quantum dots”. Eventually, the film relaxes with a large number of point defects and dislocations.

Much research has shown that using antimony as a surfactant helps prevent the onset of 3D growth<sup>94,95,96</sup>. The term “surfactant”, which traditionally has referred to an agent that lowers the surface energy of a system, emphasizes the presumed thermodynamic origin of the effects. Surfactants can be defined by two key properties. First, surfactants tend to change the growth mode of films from 3D growth (island growth), in which many atomic layers of the film grow at once, to layer-by-layer growth, in which each atomic layer is filled completely before the next layer begins. Second, surfactants tend to float on the surface of the film as deposition proceeds, leaving a relatively small trace behind. Investigators in the various areas of thin-film growth have worked to characterize these properties and to expand the range of surfactant applications.

Since the original experiments on the use of surfactants in metal thin film growth, it has become increasingly clear that the action of surfactants is due to modifications of the kinetics of the growth process and not, as initially postulated, to changes in the thermodynamics of the film/substrate system. The early observations by Egelhoff et. al.<sup>97,98</sup> of the “surfactant” effect of adsorbed gases on the growth of metal thin films — the suppression of island (3D) growth and the enhancement of layer-by-layer (2D) growth — were attributed to a modification of thermodynamic functions such as the surface energy of the films and the substrates, and a similar mechanism was invoked in a later experiment<sup>99</sup>. However, because most thin film growth (MBE and MOCVD) takes place under non-equilibrium conditions<sup>100</sup>, thus thermodynamic factors are not likely to be very important and recent attempts to explain how surfactants work have concentrated on kinetic factors.

Three-dimensional growth (island growth like quantum dot growth) of a thin film results when stable nuclei form and grow on top of two-dimensional islands before the islands themselves coalesce into a single monolayer. Consequently, one of the critical processes leading to 3D film growth is nucleation on top of the islands (second-layer nucleation). Therefore, avoiding nucleation of the second layer is necessary in order to prevent 3D growth. A logical way to suppress nucleation of the second layer is to deplete the population of adatoms on top of islands. One way to do this is to increase the

probability that atoms deposited on top of islands move down to lower layers of the film surface, a process known as interlayer mass transport.

Two proposed surfactant mechanisms involve the kinetics of a “traditional” concept of interlayer mass transport, in which the adatoms diffuse to the edge of an island and step down the next lower level. Another category of mechanisms involves interlayer mass transport methods that do not involve climbing down over a step.

Normal interlayer mass transport involves the diffusion of adatoms to the edge of an island followed by a stepping-down process onto the lower terrace. This form of transport is limited by the stepping-down process, which is governed by a rate equation characterized by an attempt frequency (the frequency with which adatoms encounter the edge of the island) and an activation energy associated with climbing down off the step. This model inspires two mechanisms of surfactant action, each of which involves the modification of one of these quantities.

One proposed surfactant mechanism attributes the enhancement of layer-by-layer growth to an increase in the island density of the growing film. The importance of increasing the island density is that the mean island size becomes smaller. This, in turn, means that adatoms taking part in normal diffusion on top of the islands visit the island edges more often due to a higher perimeter to area ratio, so the frequency factor in the step-down rate equation is increased and the interlayer mass transport is enhanced. Surfactants are thought to enhance island density by reducing the mobility of adatoms on the substrate. This increases the probability that stable nuclei will be formed on the substrate and, hence, increases the number of islands in the first layer of the film. On the other hand, in order for this mechanism to work, the surfactant must not affect the behavior of the atoms that are deposited on top of the first-layer islands; the mobility of adatoms on top of the islands must remain unchanged (or at least must remain higher than the mobility on the terraces).

For the case of metal surfactants, Oppo et. al.<sup>101</sup> and Fiorentini et. al.<sup>102</sup> attribute the mobility reduction to the role of surfactant atoms and clusters as repulsive nucleation centers. Their calculations show that adatoms tend to stay in regions of the surface that are free of metal surfactant, which limits the movement of adatoms, reduces their

effective mobility, and increases the probability that they will form stable nuclei. The mobility of adatoms on top of the newly-formed islands remains unchanged because the metal surfactant atoms move up into the new layer only when it is almost complete (when the islands coalesce); thus the metal surfactant atoms exert a mobility-reducing influence only on the atoms that are in the same level as the currently growing islands, not on the atoms that land on top of the growing islands. Other experiments also support the idea that enhanced island density can lead to layer-by-layer growth. In a conceptual paper<sup>103</sup>, Rosenfeld underscores the fact that the island-density-enhancement mechanisms require that kinetic conditions be different in different parts of the film; specifically, the conditions governing the behavior of adatoms within the layer of the growing islands must be different from the conditions governing the behavior of adatoms on top of the growing islands. He calls this “the concept of two mobilities.” This idea is strongly supported by Voigtländer et. al.<sup>104,105,106</sup> and Copel and Horn-von Hoegen et. al.<sup>107,108,109,110</sup>.

Wang and Ehrlich<sup>111</sup> point out that there are other possible mechanisms for interlayer mass transport aside from the traditional view of adatoms on top of islands diffusing to the island edge and stepping down. In particular, they refer to calculations that support a place-exchange mechanism of adatom incorporation into islands whereby adatoms on top of islands burrow down to join the islands at interior sites rather than stepping over the edge and joining the islands at edge sites. They have published several papers<sup>112,113,114,115</sup> using field ion microscopy to investigate the behavior of individual adatoms. The calculation by Feibelman<sup>116</sup> supports and extends the picture of adatom/surface atom place exchange by showing that the process may be a general mechanism for surface diffusion and, consequently, a mechanism of interlayer mass transport. Markov<sup>117,118,119</sup> supports the island-incorporation mechanism by pointing out that saturation of island edges by surfactant atoms reverses the energetic asymmetry of the island edge. In the non-surfactant-modified case, step edges are energetically asymmetric in that adatoms are attracted to ascending steps, because these are energetically favorable attachment sites, but repelled from descending steps due to the step-edge barrier. If ascending step sites are filled with surfactant atoms, on the other hand, the step may become repulsive to adatoms approaching from the same level,

because attaching now involves moving past and displacing the surfactant atoms, but attractive — or at least less repulsive — to atoms on top of the island, which can attach to the island edge by pushing the surfactant atom out one space and dropping down into the vacancy.

In conclusion, despite of much research and effort, the role of antimony is complex and not entirely explained so far. The only clear fact that shows in our work is that antimony definitely helps maintaining 2D growth and is significantly incorporated into epitaxial film. However, unlike classic surfactants discussed in this chapter, antimony does not appear to be heavily accumulated at the interface in our work.

## CHAPTER 3: Thermal Annealing Effect on GaInNAs and GaInNAsSb quantum well

**A**S grown GaInNAs and GaInNAsSb currently require relatively high temperature annealing to remove defects which result from either damage caused by high energy ions and molecular nitrogen from the RF plasma source or the very low growth temperature or some combination of both. We utilize an *ex-situ* annealing process to achieve high quality optoelectronic material. Post-growth annealing has been also used for bandgap engineering of superlattice heterostructures<sup>120</sup>, emission trimming of semiconductor lasers<sup>121</sup> using inter-diffusion, such as In-Ga and As-P atoms, or dopant profile control using doping atom diffusion<sup>122</sup>. It has also been shown that post growth annealing can improve the luminescence efficiency of dilute nitride materials<sup>20,67,123,124</sup>. In this chapter, post-growth annealing effects on photoluminescence results of GaInNAs/GaAs, GaInNAs/GaNAs, and GaInNAsSb/GaNAsSb will be discussed. The origin of the blue-shift of photoluminescence peak wavelength during post growth annealing will be also discussed.

### 3.1. Photoluminescence Improvements by Thermal Annealing

The samples used for thermal annealing investigations were grown under the same condition as those used for the earlier photoluminescence study.  $\text{Ga}_{1-x}\text{In}_x\text{N}_y\text{As}_{1-y-z}\text{Sb}_z/\text{GaN}_a\text{As}_{1-a-b}\text{Sb}_b$  ( $0 < x < 0.42$ ,  $0 < y < 0.04$ ,  $0 < z < 0.06$ ,  $0 < a < 0.06$ ,  $0 < b < 0.08$ ) quantum well samples were grown by solid source MBE as discussed earlier. The rf plasma condition used for this study was fixed while rf power at 300 W, reflected power at 6 W and  $\text{N}_2$  flow rate of 0.5 sccm. The growth temperature was 400°C and the growth rate was in the range of 0.3~0.6  $\mu\text{m}/\text{hour}$ . Samples had between one and nine quantum wells with thicknesses ranging between 70 and 100 Å. The barrier thicknesses were between 150 and 250 Å. The structure of the sample was determined by HRXRD and photoluminescence.

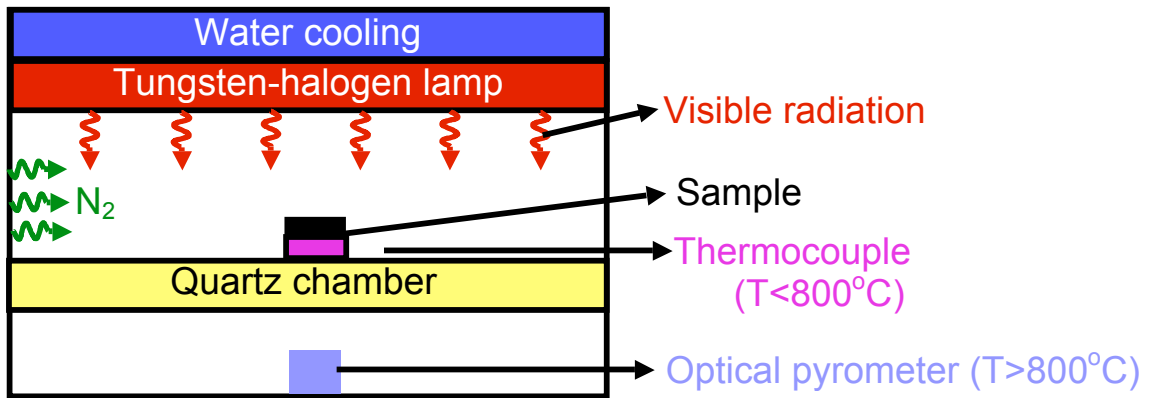


Figure 26. Schematic of RTA system for this study.

A rapid thermal annealing (RTA) system made by AG Associates with a tungsten-halogen lamp under continuous  $N_2$  flow was used for this study as shown in Figure 26. Temperature is monitored by thermocouple below  $800^\circ\text{C}$  and by pyrometer above  $800^\circ\text{C}$ . Temperature is controlled by computer using a closed-loop feedback system for better control. Time sequence and temperature gradient of temperature are programmable and controlled by the sequencer. Cooling down is done by water and oil-free air flow. The sample is put on a thermocouple wafer and covered with an epitaxial-grade GaAs

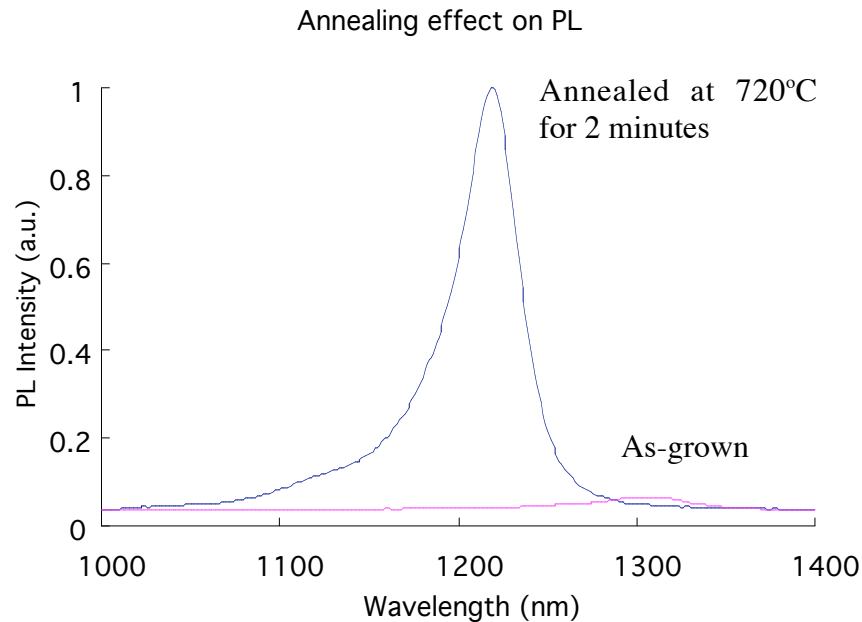


Figure 27. Room temperature photoluminescence of  $Ga_{0.7}In_{0.3}N_{0.01}As_{0.99}/GaAs$

substrate to prevent arsenic desorption from the sample surface. In this study, the annealing time was varied from 1 to 4 minutes and the annealing temperature was varied from 700°C to 860°C. After annealing, the sample was examined by photoluminescence measurements at room temperature as it will be discussed in chapter 4.1.

Figure 27 shows the room temperature photoluminescence spectra of three  $\text{Ga}_{0.7}\text{In}_{0.3}\text{N}_{0.01}\text{As}_{0.99}$  quantum wells with GaAs barriers before and after annealing. As-grown samples showed poor photoluminescence characteristics (low photoluminescence intensity and broad FWHM) due to crystal damage from the plasma source, low growth temperature, and non-optimized growth conditions. The ions, molecules and atomic nitrogen from the rf plasma source have high energy and when these particles hit the crystal surface, this damages the crystal structure causing dislocations and point defects. This is a well known phenomenon which also occurs during dry etching processes and the crystal disorder can be removed thermally by RTA. These undesired factors cause non-radiative recombination centers, including vacancies, anti-sites, interstitials, and point defects to be formed in the epitaxial layer. The photoluminescence intensity increase during post growth annealing is thought to originate from a decrease in the number of non-radiative recombination centers. Also Khreis et. al. reported that low temperature grown GaInAs/GaAs quantum wells showed larger blue-shifts after annealing those grown at higher temperature<sup>125</sup>. They found that GaInAs/GaAs quantum wells grown at low temperature included high concentrations of point defects that enhance In-Ga inter-diffusion during annealing. Since our growth temperature of 400°C is much lower than normal GaAs-based material growth temperatures, ~600°C, and normal GaInAs growth temperature of 450~500°C, as-grown GaInNAs almost certainly includes high concentrations of defects as discussed above.

As seen in Figure 27, the post-growth annealing process increases the photoluminescence intensity and decreases FWHM dramatically. Depending on the growth conditions and compositions of quaternary material, the photoluminescence intensity of as-grown samples increases 10~100 times after annealing. This photoluminescence intensity increase is certainly a desirable effect for optoelectronic device applications. However, a large blue-shift of the photoluminescence peak

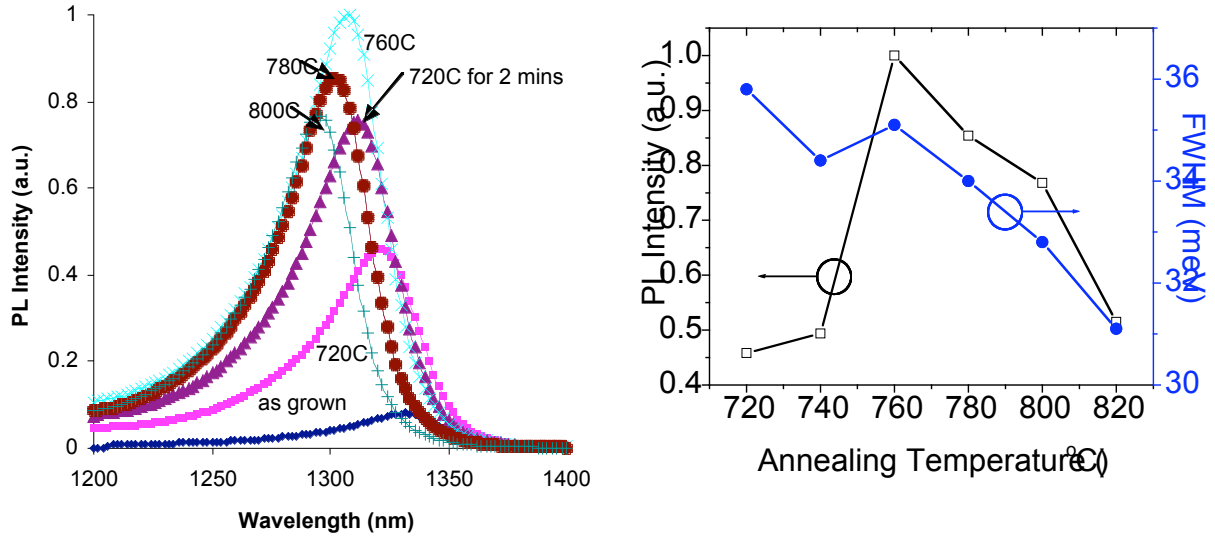


Figure 28. Photoluminescence peak intensity, peak wavelength, and FWHM as a function of annealing temperature for  $Ga_{0.7}In_{0.3}N_{0.015}As_{0.985}/GaAs$  QWs.

wavelength was also observed and, for the sample shown in Figure 27, the photoluminescence peak shifted from 1.306  $\mu\text{m}$  to 1.218  $\mu\text{m}$  ( $E=68.6$  meV) due to annealing. This large blue-shift has been one of the largest hindrances of achieving emission beyond 1.3  $\mu\text{m}$ . It is thought that both nitrogen out-diffusion from the quantum well<sup>6</sup> and nearest atom rearrangement cause this blue-shift<sup>126</sup> as will be discussed in later this chapter.

Photoluminescence properties including peak wavelength, peak intensity, and FWHM were investigated to clarify the optimum annealing conditions and the mechanism of the annealing effect as shown in Figure 28. The sample had three  $Ga_{0.7}In_{0.3}N_{0.015}As_{0.985}$  quantum wells and GaAs barriers. As shown, the photoluminescence peak wavelength continuously shifts from 1.34  $\mu\text{m}$  for the as-grown sample toward shorter wavelengths as the annealing temperature increases. On the other hand, photoluminescence intensity increases up to 760°C, but decreases beyond this value. From photoluminescence measurement for this specific sample, we can conclude that 760°C is the optimum temperature. Therefore we can conclude that the majority of the non-radiative recombination centers are annealed out at 760°C. The decrease of the photoluminescence intensity above 760°C is most likely due to arsenic desorption from the surface and crystal structure deterioration at high annealing temperature. At the

optimum temperature, photoluminescence intensity is 40 times higher than for the as-grown sample, the photoluminescence FWHM decreased to 35 meV from 90 meV, and the peak shifted from 1.34  $\mu\text{m}$  to 1.305  $\mu\text{m}$  or 55.3 meV in energy. The FWHM measured here is exaggerated due to wide open slit (3 mm) of the monochromator which, on the other hand, increases the photoluminescence intensity. To achieve accurate photoluminescence peak position and FWHM, the slit of the monochromator needs to be closed down to 0.5 mm.

### 3.2 Photoluminescence Peak Blue-Shift during Post Growth Annealing

As discussed in the previous chapter, post growth annealing improves photoluminescence intensity. This is desirable for optoelectronic device applications. However, the photoluminescence peak also blue-shifts during this annealing process, which presents a bottleneck for telecommunication laser applications at 1.3  $\mu\text{m}$ . The causes of this blue-shift have been mainly understood by two mechanisms. One cause is known to be nitrogen out-diffusion from quantum wells during annealing<sup>6</sup>. The other is nearest neighbor atom re-arrangement<sup>126</sup>.

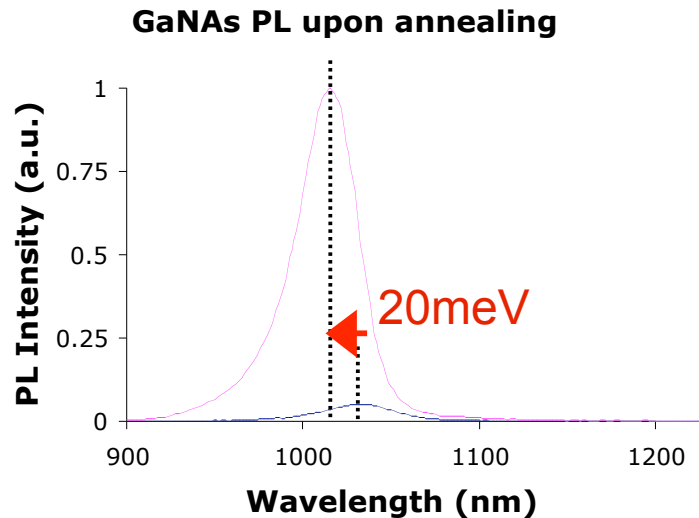


Figure 29. Photoluminescence peak intensity increase and photoluminescence peak wavelength blue shift upon annealing for  $\text{GaN}_{0.024}\text{As}_{0.976}/\text{GaAs}$ .

### 3.2.1 Nitrogen Out-Diffusion

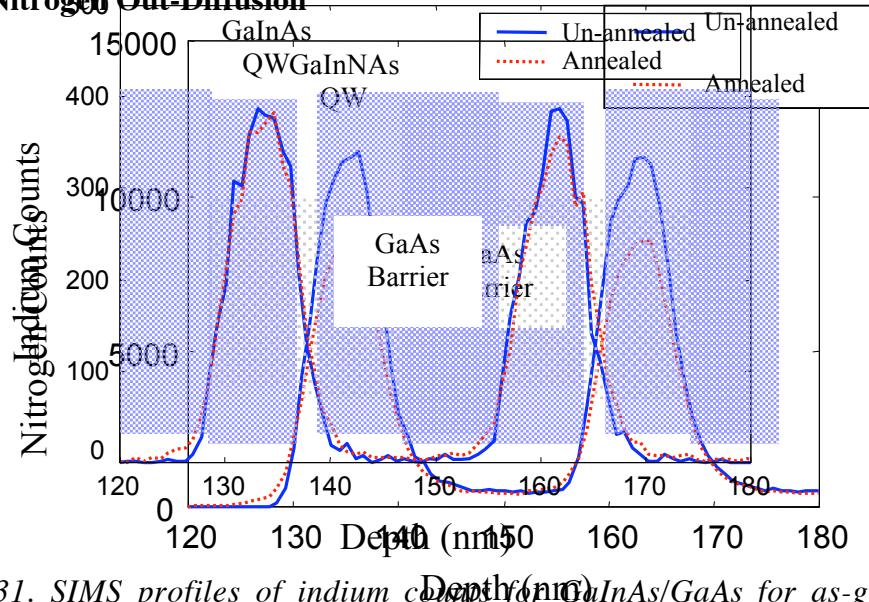


Figure 31. SIMS profiles of indium counts for GaInAs/GaAs for as-grown and annealed sample.  
 Figure 30. SIMS profiles of nitrogen counts for GaInNAs/GaAs for as-grown and annealed sample.

As a first step towards understanding the mechanisms responsible for photoluminescence increase and blue-shift from post growth annealing, GaNAs quantum well structures were grown and analyzed with the photoluminescence experiment as shown in Figure 29. We observe the same phenomenon of improved photoluminescence and photoluminescence peak blue-shift in these GaNAs quantum wells as previously

shown in (Figure 29). For this structure, there is no nitrogen out-diffusion from the well, secondary ion mass spectrometry sample for both nitrogen and indium composition. Its clearly show a 35% decrease in the quantum well during post-growth annealing. To be explored.

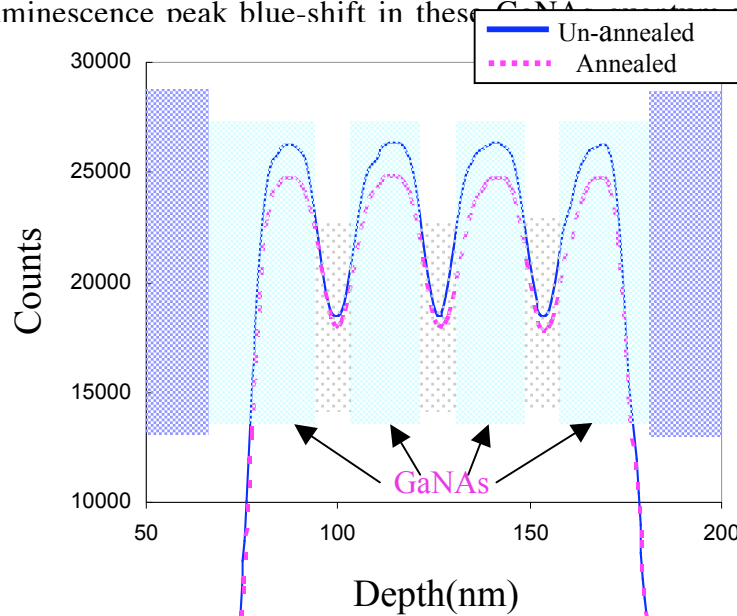


Figure 32. SIMS profiles of nitrogen counts for GaInNAs/GaAs for as-grown and annealed sample. Since, as shown in 2.6.1, nitrogen incorporation is inversely proportional

to the group III growth rate and indium was not added to the barriers (a reduced group III growth rate), the nitrogen mole fraction in the barrier is approximately 1.5 times higher in the barriers than that in the quantum wells. This higher nitrogen concentration in the barriers acts as a nitrogen reservoir for the quantum wells during annealing. Also, nitrogen in barriers reduces the band gap energy of the barrier and thus the electron confinement energy in the quantum wells, which further pushes the emission to longer wavelength. To verify our theory with GaNAs barriers, SIMS was done on a GaInNAs/GaNAs sample. As shown in Figure 32, nitrogen losses from the quantum wells and barriers were less than 8% and 10% respectively. This can be compared to 35% nitrogen loss in the structure with conventional GaAs barriers. Thus, this SIMS result shows that GaNAs barriers act as reservoirs reducing nitrogen out-diffusion during the annealing process.

Photoluminescence experiments were done on GaInNAs quantum wells with different barrier structures of GaAs and GaNAs. As shown in Figure 33, the as-grown sample with GaAs barriers shows a photoluminescence peak at 1.36  $\mu\text{m}$  while that with the GaNAs barrier sample has a photoluminescence peak at 1.44  $\mu\text{m}$ . After annealing, the photoluminescence peaks moved to 1.26  $\mu\text{m}$  and 1.34  $\mu\text{m}$  respectively, which corresponds to 73 meV and 64 meV energy shifts upon annealing. This result shows that

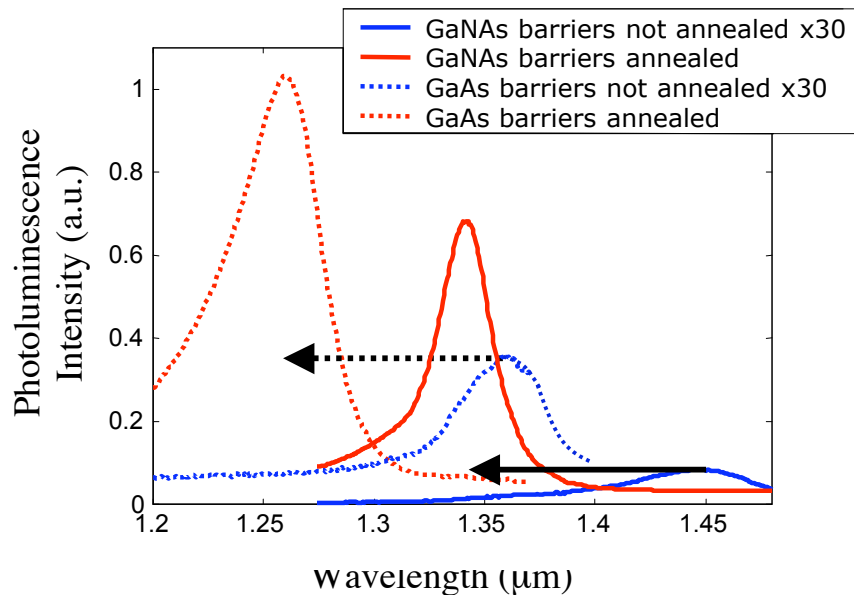


Figure 33. PL comparison between GaAs and GaNAs barrier structures.

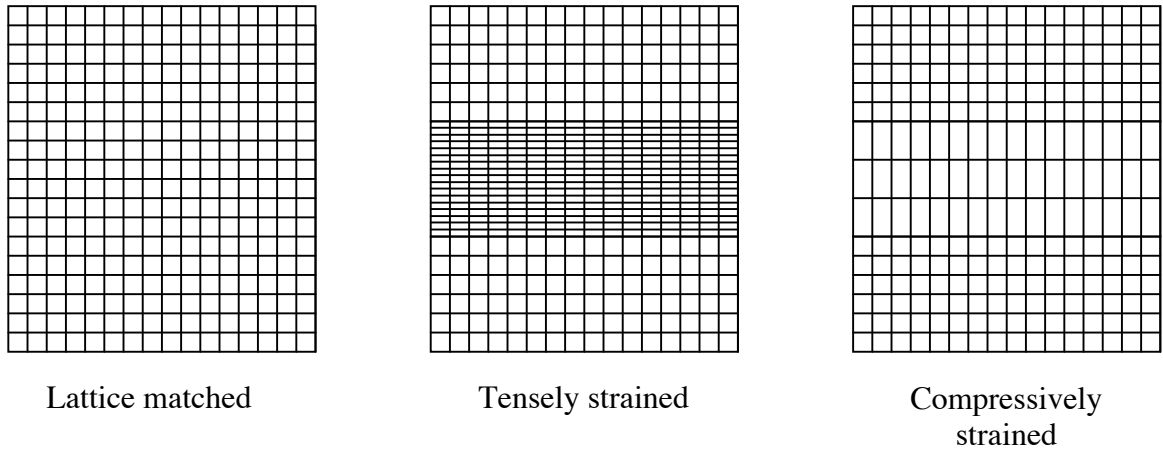


Figure 34. Schematic of strained structure.

the structure with GaNAs has longer wavelength emission for both as grown and annealed samples by suppression of the blue-shift.

GaNAs barriers can also reduce the overall strain from the quantum well, making it possible to grow more quantum wells for high power device applications. This is due to the fact that quantum wells are usually grown under compressive strain to take advantage of reduced heavy hole effective mass discussed in 5.2. Also, for our case, higher indium incorporation is preferable to higher nitrogen incorporation due to fewer non-radiative recombination centers. For these reasons, it is imperative to have compressively strained quantum wells and this strain limits the volume of active layer.

Since nitrogen is a smaller atom than arsenic, GaN has a smaller lattice constant than GaAs, which places the GaNAs barriers under tensile strain compared to GaAs.

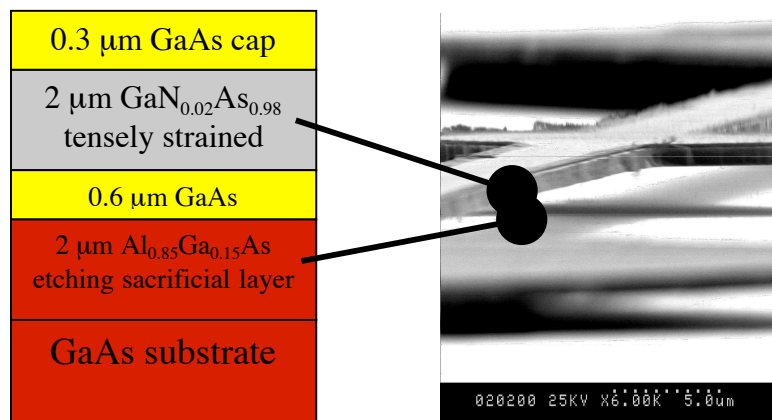


Figure 35. GaNAs air bridge structure  
 (a) GaNAs air bridge structure (b) SEM image of air-bridge structure after sacrificial layer etching

Compressive strain and tensile strain are depicted in Figure 34. Since GaNAs barriers have the opposite strain compared to the quantum wells, these barriers relieve the strain from the quantum wells.

To show the mechanical strength of the tensely strained quantum well, a GaNAs air bridge structure with an AlGaAs sacrificial layer was grown as shown in Figure 35 (a). If the layer above the sacrificial layer is not under tensile strain, the top layer collapses when the sacrificial layer is etched away. In the past, to have the GaAs layer under tensile strain,  $\text{Si}_x\text{N}_{1-x}$  dummy layer under tensile strain was deposited on top of the GaAs layer to hold the underneath layer in the air. However, the strain of GaNAs layer eliminates the necessity for this dummy layer. In Figure 35, the GaNAs air-bridge structure is free-standing after the sacrificial layer is removed. This is a very important material property for MEMS applications such as tunable optoelectronic devices.

To prove the strain compensation between GaNAs and GaInNAs, multiple numbers of quantum wells of three, six and nine were grown. The quantum well thickness was 70 Å each and the barriers were each 200 Å wide. The three, six, and nine quantum well samples have a total quantum well thickness of 210 Å, 420 Å, and 630 Å

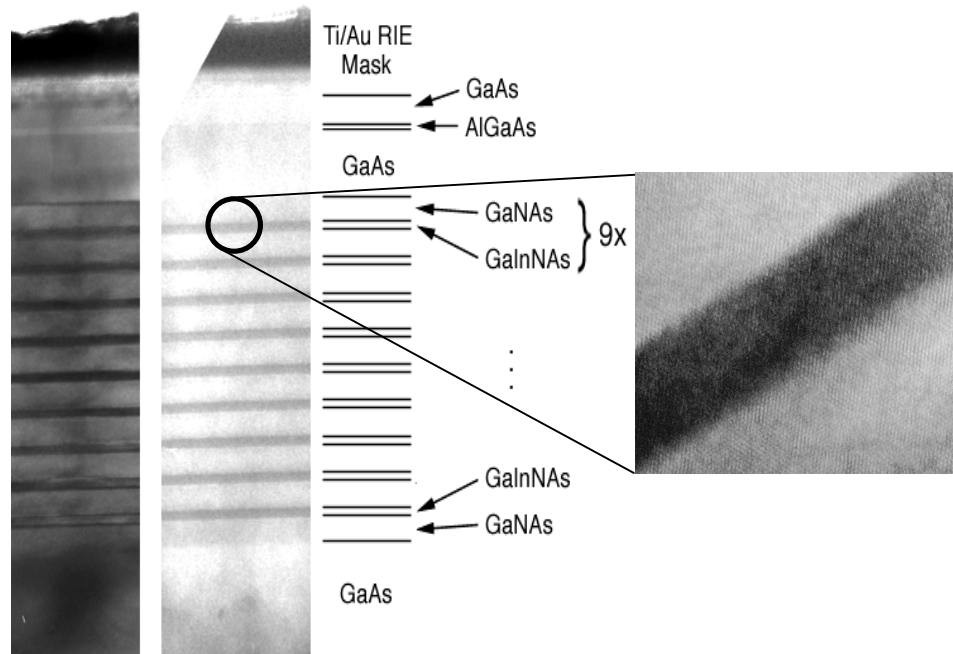


Figure 36. TEM images of a nine quantum well sample and a higher magnification image of the top quantum well.

respectively, despite a 70 Å critical thickness for GaInAs layer with 30% indium mole fraction. To investigate this, TEM was performed on a sample and a TEM image shows no noticeable lattice fringes, well-defined interface, and optical properties. As the number of photoluminescence quantum wells increases linearly, the gain regions for quantum wells become more well-defined.

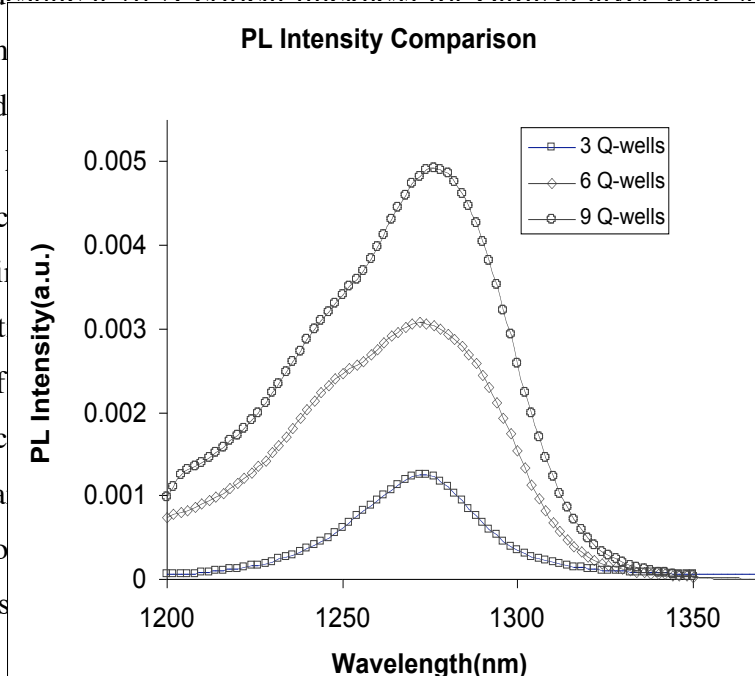


Figure 37. PL intensity comparison for different numbers of quantum wells.

### 3.2.2 Nearest Atom Rearrangement

Microscopy (TEM) image of this sample shows sharp and well-defined interface to identify the relationship between the number of quantum wells and the peak intensity. Figure 37 shows the relationship between the number of quantum wells and the peak intensity to grow larger as the number of quantum wells increases between nine quantum wells.

During the growth process, chemical bonding aspects dominate at the surface, which favors Ga-N bonds instead of In-N bonds because the bonding of Ga-N is stronger than that of In-N. This state is frozen in during the non-equilibrium growth process.

In contrast to the surface, In-rich nitrogen neighbor configurations are favored in the bulk at equilibrium due to the dominance of local strain effects. In Figure 1, InAs has a bigger lattice constant than GaAs and GaN has a smaller lattice constant than GaAs, which makes the lattice constant of In-N closer than GaN to the GaAs substrate. Therefore, the frozen non-equilibrium bulk state, Ga-N, may be transformed into the equilibrium bulk state, In-N, during post-growth annealing. Since the GaInNAs growth temperature is low, there are many vacancies formed during the growth and it is believed that changes in the nitrogen nearest neighbor is enhanced by these vacancies. It is probably due to a hopping of interstitial nitrogen ions into the vacancies and unlikely to change of the nitrogen atom site bonded to group III atoms. This is because the energy required to break the bonds between nitrogen and neighboring group III atoms is very high compared to the energy provided by thermal annealing. The nitrogen hopping process is driven by the competition between chemical bonding and local strain contributions to the site energies of the different nitrogen environments as it is explained

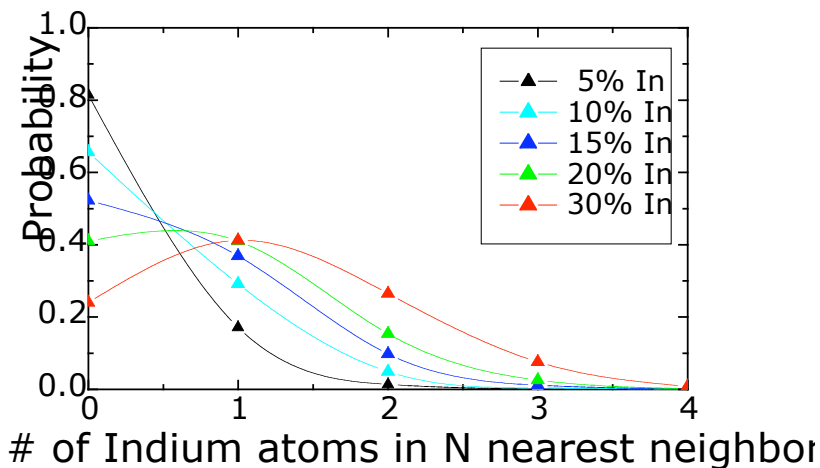


Figure 38. Simulation of configurations surrounding nitrogen atom for different indium concentration during growth. The chemical bonding energy difference between GaN and InN is not considered<sup>127</sup>.

above. This theory is shown by many research groups<sup>127,128,129</sup>. To verify this theory for

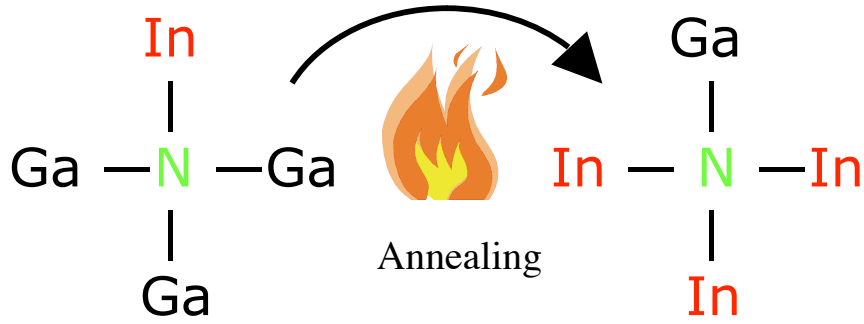


Figure 39. The probable configuration change around nitrogen atom during annealing process.

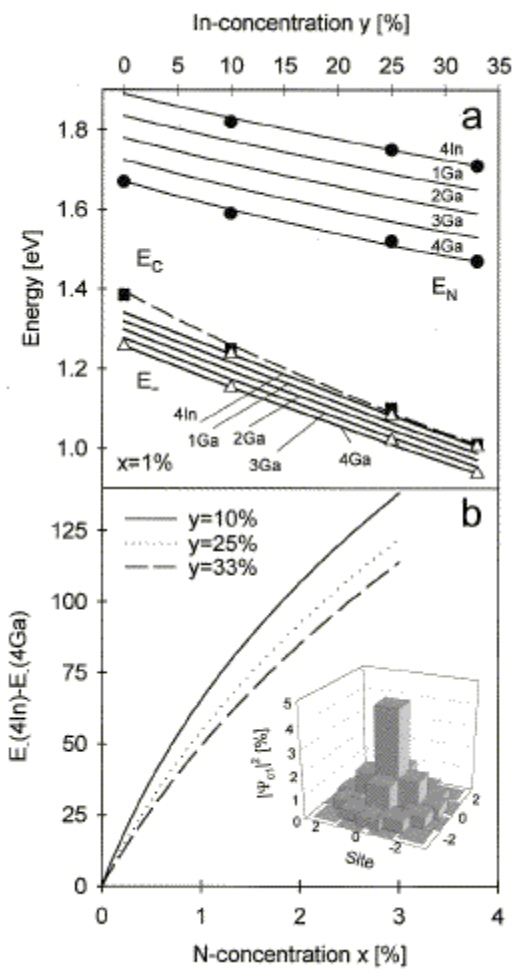


Figure 40. Super-cell simulation results of the conduction band structure of  $Ga_{1-y}In_yN_xAs_{1-x}$  for various nitrogen neighbor environments of the nitrogen center. (a)  $y$  dependence, Constant  $x$ . (b)  $x$  dependence, constant  $y$ . Inset: probability density of the conduction band edge wave function around the nitrogen center<sup>127</sup>.

our case, a  $GaN_{0.024}As_{0.976}/GaAs$  sample was grown and annealed. The photoluminescence experiment result is shown in Figure 29. The photoluminescence peak blue-shift was 20 meV, which is from nitrogen out-diffusion from the quantum well since there is no indium causing Ga-In inter-diffusion or nearest atom re-arrangement. This 20 meV blue-shift is smaller than that of 35 meV  $\sim$  80 meV from  $GaInNAs/GaAs$  and  $GaInNAs/GaNAs$  samples. Therefore, we can conclude that the rest of the blue-shift is caused by the change in nitrogen environment. For a better understanding of this mechanism, simulations were done to find the most probable configuration of Ga-N and In-N for different indium concentrations, as shown in Figure 38. The chemical bonding energy

difference between GaN and InN is not considered for this simulation. For the 30% indium concentration, there will be most likely only one indium atom surrounding the nitrogen atom. This configuration will be changed to the configuration with a higher number of indium atoms as shown in Figure 39 during the annealing process. Figure 40 (a) shows results of 216-atom super-cell simulation done by Klar et. al. for  $\text{Ga}_{1-y}\text{In}_y\text{N}_x\text{As}_{1-x}$  (corresponding to  $x \approx 0.01$ )<sup>126</sup>. Regardless of the indium concentration, the nitrogen energy level above valence band,  $E_N$ , is equally spaced for the five nitrogen neighbor (NN) configurations. The energy for four Ga NNs (meaning that four gallium surrounds nitrogen atom) is always about 220 meV lower than that of four In NNs. The derived matrix element,  $V_{Nc}$ , linking the nitrogen resonant state and the conduction band-edge, varies between about  $2.0 \text{ eV}_x^{1/2}$  for four Ga NNs to about  $1.35 \text{ eV}_x^{1/2}$  for four In NNs. This indicates that the strength of the perturbation of the crystal decreases with increasing number of indium atoms surrounding nitrogen. The large differences of the five NN configurations are also reflected in the derived conduction band edge energies  $E_c$ . For each  $y$  at  $x=0.01$ , the  $E_c$  values for the five configurations are evenly spread over an energy range of about 80 meV below the corresponding unperturbed  $E_c$  of GaInAs, with that for four Ga NNs being lowest in energy. The influence of the different NN configurations on the valence band edge is small compared to that on the conduction band edge. The magnitude of the splitting  $E_c(4 \text{ Ga}) - E_c(4 \text{ In})$  increases strongly with  $x$  for all  $y$  in Figure 40 (b). The three curves were calculated by varying the number of the atoms in the super-cell between 1728 ( $x \approx 0.001$ ) and 64 ( $x \approx 0.031$ ). This theoretical calculation supports the fact that NN configuration changes from the preferred chemical bonding state with more gallium around nitrogen to the preferred crystal structure state with more indium around nitrogen causing the photoluminescence peak blue-shift. This effect becomes obvious as more nitrogen is incorporated as it is shown in Figure 40 (b). Also, at high nitrogen concentration, the amount of nitrogen out-diffusion increases. These reasons, combined with the fact that high nitrogen increases the non-radiative recombination center, means that one wants to limit the nitrogen concentration for better device performance, which necessitate high indium concentrations. The inset of Figure 40 (a) depicts the probability density of the band edge wave function  $\psi_{cl}$ . About 40% of it

is localized around the nitrogen impurity and its four NNs. Changing the NN configuration modifies this localized band-edge strongly. Such strong impurity-like band gap behavior has been reported for GaNAs<sup>130</sup> and GaInN<sup>131</sup>. It explains the strong effect of the nitrogen impurity environment on the band gap structure of GaInNAs.

## **CHAPTER 4: Characterization**

The previous chapter discussed the MBE growth of GaInNAs and GaInNAsSb. After the material is grown, it undergoes several measurement steps to determine the characteristics of the material. This is very important step to understand this new material system, the MBE growth conditions, and to find the optimum conditions for optical devices. Determining the optimum MBE growth conditions is not an easy task and only can be found by trial and error because of the complexity of the four and five element alloys. The methods used in this work were photoluminescence (PL), high-resolution x-ray diffraction (HRXRD), photo-reflectance (PR), electro-reflectance (ER), secondary ion mass spectrometry (SIMS), cathodoluminescence (CL) and Rutherford backscattering spectroscopy (RBS).

### **4.1 Photoluminescence (PL) Spectroscopy Measurement**

#### **4.1.1 Introduction**

Photoluminescence is a measurement of the spontaneous optical emission obtained after photon excitation (usually a high power pump laser) and is observed with a grating spectrometer and semiconductor detectors. This analysis allows non-destructive characterization of semiconductors, including material composition, by measuring the bandgap energy and the optical quality of material by comparing the sample with standard sample. New III-V composition and novel structures were tested by photoluminescence and applied to optical devices.

High power pump light illuminates the sample, where it is absorbed and imparts excess energy into the material in a process called "photo-excitation" as shown schematically in Figure 41. To excite the electrons from ground states to excited states, the pump light must have a higher energy than the bandgap energy. Also the pump light

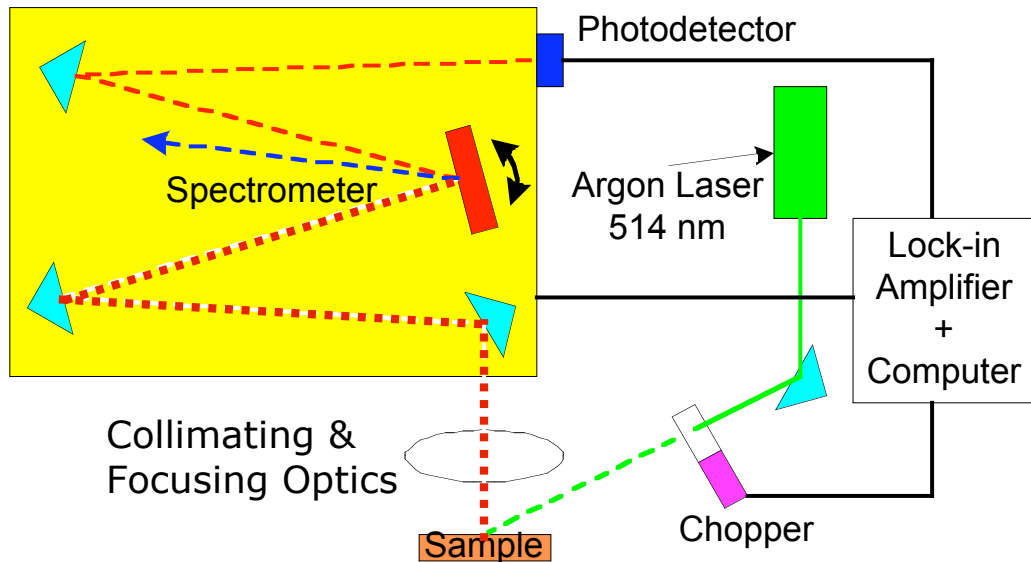


Figure 41. Photoluminescence spectroscopy measurement setup.

needs to have enough intensity to excite enough electrons so that the output can be easily detected with a high signal to noise ratio (SNR).

The relaxation process from a sample following photo-excitation is the emission of a photon, or luminescence. In the case of photo-excitation, this luminescence is called "photoluminescence (PL)." The intensity and spectral content of this PL is a direct measure of various important material properties. Specifically, photo-excitation causes electrons within the material to move into permissible excited states. When these electrons return to their equilibrium states, the excess energy is released and may include the emission of light by a radiative process or by a non-radiative process. The energy of the emitted light, PL, is related to the difference in energy levels between the two electron states involved in the transition—between the excited state and the equilibrium state, and this is bandgap energy in semiconductor material. The quantity of the emitted light is related to the relative efficiency of the radiative process. The material properties, which can be obtained from PL measurement, are following,

1. Bandgap determination: The most common radiative transition in semiconductors is between states in the conduction and valence bands, where the energy difference is the bandgap. Bandgap determination is particularly

useful when working with new compound semiconductors and for determining compositions.

2. Impurity levels and defect detection. Radiative transitions in semiconductors involve localized defect levels. The photoluminescence energy associated with these levels can be used to identify specific defects, and PL intensity can be used to determine their concentration. For this specific experiment, PL needs to be done at low temperature and with a tunable wavelength laser to distinguish signals from each energy level.
3. Recombination mechanisms. As discussed above, the electron's return to equilibrium, also known as recombination, can involve both radiative and non-radiative processes. The PL intensity and its dependence on the level of photo-excitation and temperature are directly related to the dominant recombination process. Analysis of PL helps to uncover the underlying physics of the recombination mechanisms.
4. Material quality. In general, non-radiative processes are associated with localized defect levels, whose presence is detrimental to material quality and subsequent optical device performance. Thus, relative material quality can be measured by quantifying the amount of radiative recombination.

#### 4.1.2 Theoretical Background

There are many ways for a semiconductor to relatively remove the excess energy added by the pump light: electron-hole recombination from the conduction band to valence band, free exciton recombination, recombination of excitons bound to neutral donors and acceptors, electron-hole recombination from the conduction band to an acceptor level, and recombination from a donor level to an acceptor level. The basic carrier excitation and recombination of direct bandgap semiconductors is illustrated in Figure 42.

The lifetime for electrons in the conduction band is,  $\tau_{ot}$ ,

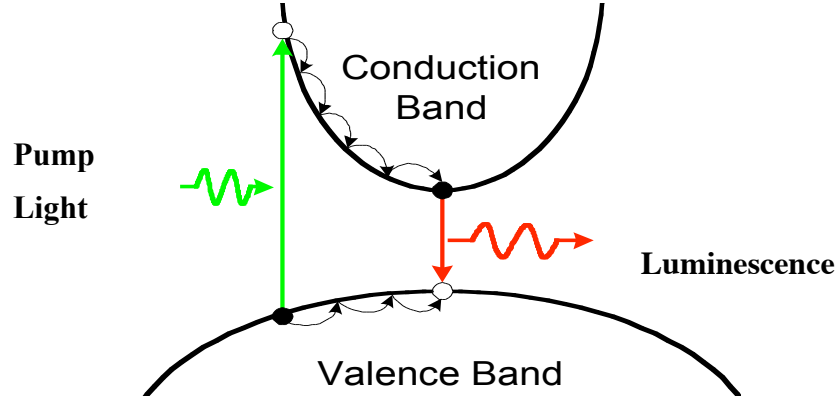


Figure 42. Basic theory on band diagram and luminescence.

$$\frac{1}{\tau_{tot}} = \frac{1}{\tau_{non-rad}} + \frac{1}{\tau_{rad}}$$

where,  $\tau_{rad}$  is the radiative recombination lifetime and  $\tau_{non-rad}$  is non-radiative recombination lifetime. In addition to spontaneous emission, radiative recombination, there are other non-radiative process, including: Auger recombination, trapping and recombination at impurities and defects, and surface recombination. If the non-radiative recombination process dominate, the PL intensity will be sharply decreased and the optical device performance will be degraded. Therefore, while somewhat qualitative, PL intensity is directly related to laser performance.

From Fermi's golden rule<sup>133</sup>, the radiative recombination (spontaneous emission) at one wavelength,  $R_{sp}(\hbar\omega)$ , is equal to the transition rate from filled states in the conduction band to empty states in the valence band times the probability of a filled initial state and an empty final state,

$$R_{sp}(\hbar\omega) \cdot d(\hbar\omega) = \sum_{i,f} \frac{2\pi}{\hbar} \left| \langle f | H'(r,t) | i \rangle \right|^2 P_i \cdot P_f \cdot \delta(E_f - E_i - \hbar\omega) \cdot d(\hbar\omega)$$

where,  $P_i$  is the probability that the initial state is occupied and  $P_f$  is the probability that the final state is empty. These probabilities can be determined using Fermi-Dirac statistics,

$$P_i = \frac{1}{1 + \exp\left(\frac{E_i - E_F^e}{k_B T}\right)}, \quad \text{and} \quad P_f = \frac{1}{1 + \exp\left(\frac{E_f - E_F^h}{k_B T}\right)}$$

where,  $E_F^e$  and  $E_F^h$  are the electron and hole quasi-Fermi levels. Since the downward and upward transition rates should be equal at thermal equilibrium, the emission and the absorption processes are related each other. Therefore, the spontaneous emission can be calculated from the absorption equation using the van Roosbroeck-Shockley relation,

$$R_{sp}(\hbar\omega) = \frac{8\pi}{h^3 c^2} \frac{(\hbar\omega)^2}{\exp\left(\frac{E_i - E_F^e}{k_B T}\right) + \exp\left(\frac{E_F^h - E_f}{k_B T}\right)} \cdot \alpha(\hbar\omega)^{132}$$

where,  $h (=2\pi\hbar)$  is Planck's constant and  $E_F = E_F^e = E_F^h$ . For direct band-to-band transitions, with parabolic bands, the expression for  $\alpha(\hbar\omega)$  is,

$$\alpha(\hbar\omega) = \frac{\hbar e^2}{4\pi m_0 n_r c \epsilon_0} \frac{E_p}{\hbar\omega} \frac{2\pi \epsilon_{eff}^{3/2}}{\hbar^2} (\hbar\omega - E_g)^{1/2} \quad 133$$

Therefore the spontaneous emission,  $R_{sp}(\hbar\omega)$ , can be expressed as,

$$R_{sp}(\hbar\omega) = (\hbar\omega - E_g)^{1/2} \cdot \exp\left(-\frac{(\hbar\omega - E_g)}{k_B T}\right)$$

and the Fermi-Dirac distribution may be approximated by a Boltzmann distribution. This assumption results in a PL peak shape as shown in Figure 43<sup>134</sup> with an exponential tail toward higher energy (or shorter wavelength). The peak energy,  $\hbar\omega_p$ , and the half-width,  $\Delta E$ , of the PL signal are respectively,

$$\hbar\omega_p = E_g + \frac{1}{2}k_B T \quad \text{and} \quad \Delta E = 1.8k_B T$$

Thus far we have derived equations for spontaneous emission from bulk material. Since most of the optical devices have multiple quantum wells, we need to calculate the emission mechanism from a quantum well. Based on the calculation of energy levels in a quantum well, which will be described in chapter 5.1, we can derive the PL spectra from a quantum well. Starting from the absorption spectra calculation from a quantum well,

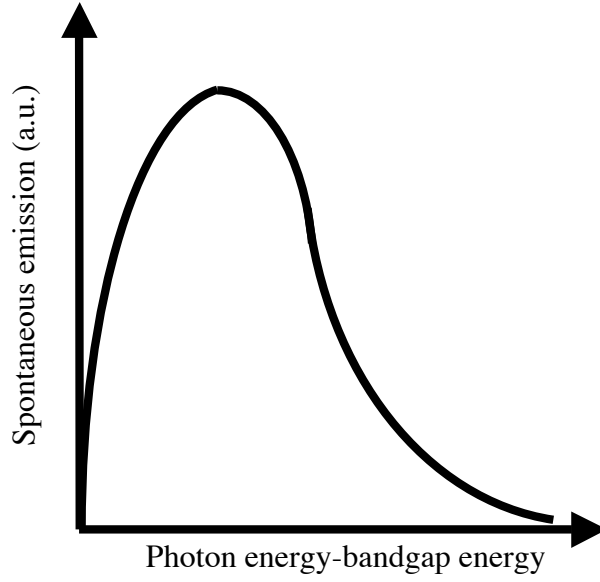


Figure 43. Spontaneous emission spectrum for direct band semiconductor.

$$a(\hbar\omega) = \frac{e^2}{2n_r c \epsilon_0 m_0} E_p \sum_{n,m} |I_{hm}^{en}|^2 \frac{m_r}{\hbar^2 L_z} H(\hbar\omega - E_{hm}^{en})$$

with  $E_{hm}^{en} = E_g + E_{en} - E_{hm}$  in which  $E_{en}$  and  $E_{hm}$  are the energies for the electron and hole respectively, and  $I_{hm}^{en} = \int dz \psi_n^*(z) \psi_m(z)$  is the overlap integral of the conduction- and valence-band envelope functions. For an infinite quantum well,  $I_{hm}^{en} = \delta_{nm}$  and  $a(\hbar\omega)$  is given by,

$$a(\hbar\omega) = \frac{e^2 \hbar}{2n_r c \epsilon_0 m_0} \frac{E_p}{\hbar\omega} \begin{cases} \frac{m_r}{\hbar^2 L_z} & \text{for } E_{h1}^{e1} < \hbar\omega < E_{h2}^{e2} \\ 2 \frac{m_r}{\hbar^2 L_z} & \text{for } E_{h2}^{e2} < \hbar\omega < E_{h3}^{e3} \\ 3 \frac{m_r}{\hbar^2 L_z} & \text{for } E_{h3}^{e3} < \hbar\omega < E_{h4}^{e4} \\ \text{etc} \end{cases}$$

where, we have again assumed that the valence band is completely filled and the conduction band is completely empty. If this is not the case, the absorption from injected carriers,  $a_j$ , can be found by<sup>133</sup>,

$$a_j(\hbar\omega) = a(\hbar\omega) P_m(\hbar\omega - E_{hm}^{en}) P_n(\hbar\omega - E_{hm}^{en})$$

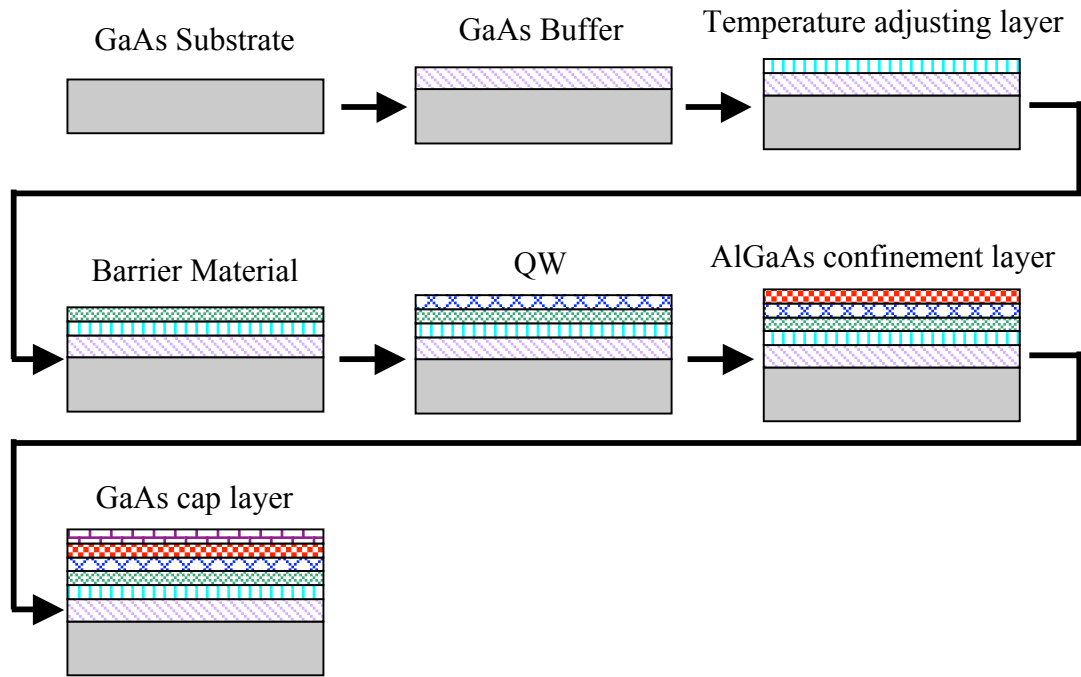


Figure 44. PL sample growth sequence

where  $P_m(\hbar\omega - E_{hm}^{en}) - P_n(\hbar\omega - E_{hn}^{en})$  is the Fermi-Dirac population inversion factor. The relationship between absorption and spontaneous emission gives a spontaneous emission spectrum of the form,

$$R_{sp}(\hbar\omega) = \frac{8}{h^3 c^2} [\hbar\omega]^2 P_n (1 - P_m) a(\hbar\omega)$$

which still has the typical shape shown in Figure 43.

### 4.1.3 Photoluminescence Sample Growth

Photoluminescence sample growth is a very important step prior to device growth. By growing PL samples, the emission wavelength for specific growth conditions can be predicted and by measuring photoluminescence intensity, the optical quality of the material can be evaluated. The normal photoluminescence sample growth sequence is as follows and is shown schematically in Figure 44,

- 1 300 nm GaAs buffer layer is grown.

- 2 40 nm GaAs layer is grown while the substrate temperature is changed to the active layer growth temperature (usually lower).
- 3 The first QW barrier material is grown. The choice of barrier material depends on the QW material. If the photoluminescence sample contains nitrogen, the plasma source is ignited 10 minutes before the first nitrogen containing layer is grown to ensure stable plasma operation. If antimony is needed, the antimony shutter is opened 30 seconds before the first layer with antimony to ensure a stable Sb flux.
- 4 A single QW, or multiple QWs are grown as the active layer.
- 5 For improved carrier confinement and reduction of surface recombination, 10 nm of  $\text{Al}_{0.33}\text{Ga}_{0.67}\text{As}$  is grown.
- 6 GaAs capping layer is grown at elevated temperature.

The as-grown sample is divided into pieces, annealed at different temperatures and then tested. To match with laser growth conditions, as-grown samples are often re-loaded into the MBE growth chamber and annealed at the same growth temperature and time for either laser cladding layer or DBR growth. The *in-situ* annealed sample follows the same steps as the as-grown sample and the optimum annealing condition is determined by photoluminescence measurements.

#### **4.1.4 Photoluminescence Experimental Setup and Results**

The photoluminescence setup for this work is shown in Figure 41. An  $\text{Ar}^+$  ion laser ( $\lambda=514.5$  nm) serves as the pump laser with an output power of 500 mW. After passing through mirrors and focusing lenses, the pump light power level at the sample surface is 200 mW. Therefore, the actual pumping power on PL samples is 200mW. This power is kept constant for all samples to compare PL intensity from each sample and to understand the recombination mechanism and material quality. The pump light passes through a chopper, which is referenced to a lock-in amplifier. Using reference chopped signal and lock-in amplifier, we can get a clean signal and higher sensitivity. This is important since the luminescence from as grown samples is particularly weak and this

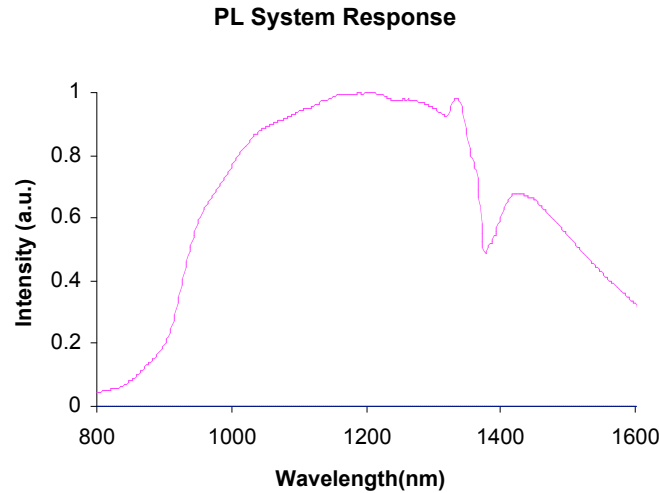


Figure 45. Photoluminescence System response.

signal must pass through a collimating lens, focusing lens, and spectrometer. Each optical component decreases the luminescence intensity. Since the spectrometer relies on the angle of the grating inside to determine the wavelength, the input opening should be small and this opening is usually made by an adjustable slit. We normally decrease the slit down to 3 mm to get high wavelength resolution, resulting in additional luminescence loss. For higher wavelength resolution, the slit needs to be closed down to a few tenths of a mm. The luminescence passing through both input and output slits is detected by GaInAs photodiode. The photo-generated electrical signal is fed into a lock-in amplifier, processed, and the data is sent to a control computer.

Due to the optics, spectrometer and detector characteristics as a function of wavelength, the system background signal is not flat in the wavelength domain. The PL system response, taken with a white light source, is shown in Figure 45. As it shows, there is quite significant signal amplitude fluctuation across between 800 nm and 1600 nm. The grating has a blaze point at 1200 nm. The blaze point is where the grating has maximum efficiency and each grating has a different blaze point, dependent on its design. Therefore the raw data taken from the lock-in amplifier will not show correct information due to this system response fluctuation and it must be processed to remove the system response. This is especially important for samples with photoluminescence peaks longer than 1300 nm.

As explained, the PL intensity data cannot be directly compared since different setups can have different efficiency and signal strengths. The only way to get a reasonable comparison of the photoluminescence intensity between samples is to compare them with an already-known, “standard”, sample, which is described below.

For system wavelength calibration, a He-Ne laser and standard GaAs quantum wells with AlGaAs barriers sample is used. The He-Ne laser is positioned on the sample holder and scattered light is collected in the same way as the luminescence from sample. Since He-Ne laser has a peak wavelength at 632.8 nm, the spectrometer is scanned over a broad wavelength range to find the scattered light peak exactly at that wavelength. This process is an especially convenient way since the He-Ne laser beam is visible. Once the peak is located, the wavelength offset between the spectrometer and real wavelength can be corrected. The GaAs quantum well sample can also be used as a wavelength calibration as well as a PL intensity reference. Since this sample was grown under well-known conditions, we know the quantum well thickness and energy band offset to calculate the bandgap energy and also the quality of quantum well for intensity comparison. With this standard sample, the wavelength calibrated with the He-Ne laser can be confirmed and the luminescence intensity from new material can then be compared. Usually a good quality GaInNAs quantum well sample has half the peak intensity as the standard GaAs quantum well sample.

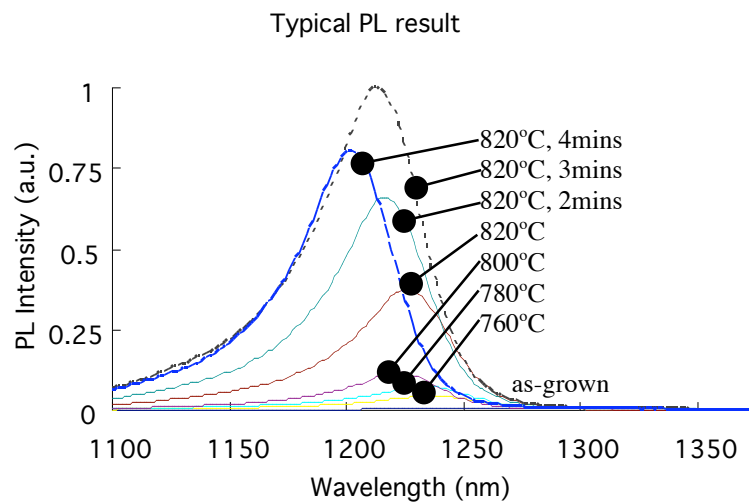


*Figure 46. Typical photoluminescence result dependent on annealing temperature from GaInNAs sample.*

Typical PL data for different annealing conditions of GaInNAs quantum wells is shown in Figure 46. The PL signal from quantum wells plotted as a function of wavelength normally has a bell-shape. This is because luminescence efficiency reaches its maximum at the bandgap energy and the photoluminescence peak corresponds to this bandgap energy. The as-grown sample shows small PL intensity and the peak is at a longer wavelength. As the sample is cleaved in many pieces and annealed at different temperature, both PL intensity and peak change. The PL intensity increases until the annealing temperature reaches 760°C. The PL peak also shifts to shorter wavelengths (blue-shifts). As the annealing temperature passes 760°C, the PL intensity decreases but the peak continues moving toward shorter wavelengths. Clearly the optimum temperature for this PL sample is 760°C. The effect of annealing on GaInNAs(Sb) material was discussed in chapter 3. Compared to the intensity from a standard GaAs quantum well sample, the intensity of this sample was 30%, which indicates a reasonably high quality of material. The full width at half maximum (FWHM) of the 760°C-annealed sample is 35 meV, which also proves the high quality of material. This FWHM can be used to judge the abruptness between quantum well and barrier and the uniformity of multiple

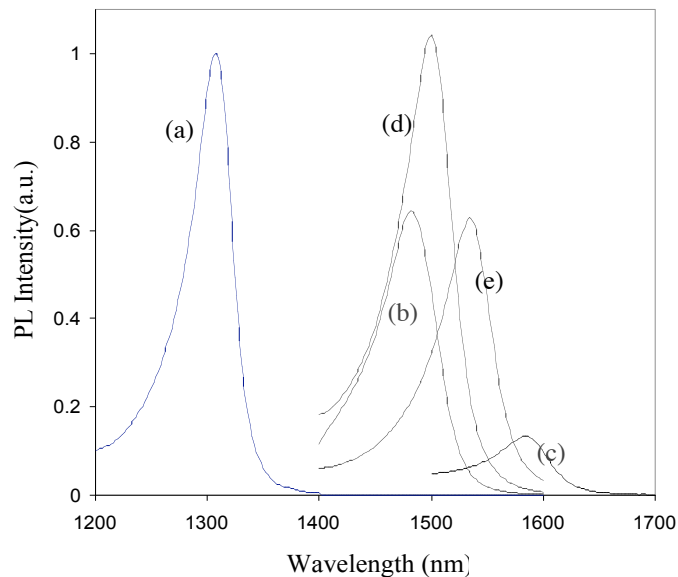


Figure 47. PL of various GaInNAs(Sb) samples normalized to (a) the highest 1.3  $\mu\text{m}$  photoluminescence intensity from three quantum wells, (b) three quantum well, 37% In, and Sb BEP of  $7.2 \times 10^{-8}$  Torr, (c) three quantum well, 38% In, and Sb BEP of  $1.4 \times 10^{-7}$  Torr, (d) 10 nm thick Single quantum well, 39% In, and Sb BEP of  $1.2 \times 10^{-7}$  Torr, (e) 9 nm thick Single quantum well, 42% In and Sb BEP of  $1.0 \times 10^{-7}$  Torr.

Sample number	Structure	In %	N %	PL Peak (nm)	PL Intensity	PL Peak Annealing Condition	Sb flux
n232d	GaInNAs/GaAs	30	2.1	1.28	6.72E-10	820°C 4minutes	N/A
233b	GaInNAs/GaAs	24	2.2	1.214	1.02E-09	820°C 3minutes	N/A
n234	GaInNAs/GaAs	25	2.2	1.204	2.07E-10	760°C 1minute	N/A
n237c	GaInNAs/GaAs	30	2.1	1.258	6.92E-10	820°C 3minutes	N/A
n244	GaInNAs/GaAs	24	2.1	1.206	2.68E-09	820°C 3minutes	N/A
s277	GaInNAs/GaAs	31	2.1	1.288	8.53E-10	760°C 1minute	N/A
n299	GaInNAs/GaAs	31	2.1	1.274	6.82E-10	800°C 1minute	N/A
n305	GaInNAs/GaAs	31	2.1	1.282	2.10E-10	820°C 1minute	N/A
n233c	GaInNAs/GaNAs	23	2	1.226	5.03E-10	820°C 3minutes	N/A
n236	GaInNAs/GaNAs	29	2.1	1.304	2.95E-10	800°C 1minute	N/A
n237a	GaInNAs/GaNAs	24	2.1	1.24	7.09E-10	820°C 4minutes	N/A
n243	GaInNAs/GaNAs	30	2.1	1.294	4.08E-10	820°C 3minutes	N/A
n246	GaInNAs/GaNAs	30	2.1	1.302	2.19E-10	820°C 3minutes	N/A
n250	GaInNAs/GaNAs	29	2.1	1.278	2.96E-10	800°C 1minute	N/A
n256	GaInNAs/GaNAs	30	2.1	1.308	4.04E-10	760°C 1minute	N/A
n282	GaInNAs/GaNAs	28	2.2	1.248	6.08E-10	820°C 2minutes	N/A
s300	GaInNAs/GaNAs	31	2.1	1.324	4.05E-13	820°C 2minutes	N/A
n242	GaInNAsSb/GaNAsSb	30	2.1	1.312	3.02E-10	820°C 3minutes	1.35E-08
n247	GaInNAsSb/GaNAsSb	29	2.1	1.326	9.97E-11	820°C 1minute	7.36E-08
s252a	GaInNAsSb/GaNAsSb	36	2.3	1.458	1.16E-11	760°C 1minute	4.58E-08
s257	GaInNAsSb/GaNAsSb	37	2.3	1.482	1.63E-10	780°C 1minute	7.14E-08
s258	GaInNAsSb/GaNAsSb	38	2.2	1.586	2.03E-11	780°C 1minute	1.40E-07

Sample number	Structure	In %	N %	PL Peak ( $\mu\text{m}$ )	PL Intensity	PL Peak Annealing Condition	Sb flux
s261	GaInNAsSb/GaNAsSb	29	2.1	1.316	9.87E-11	820°C 2minutes	7.08E-08
n270	GaInNAsSb/GaNAsSb	37	2.3	1.426	2.09E-11	820°C 2minutes	7.05E-08
n275	GaInNAsSb/GaNAsSb	35	2.7	1.518	2.01E-11	780°C 1minute	8.14E-08
n288	GaInNAsSb/GaNAsSb	42	2.4	1.55	1.27E-12	780°C 1minute	7.20E-08
n289	GaInNAsSb/GaNAsSb	40	2.4	1.492	8.56E-11	780°C 1minute	7.20E-08
n290	GaInNAsSb/GaNAsSb	43	2.1	1.476	8.96E-11	780°C 1minute	7.96E-08
n306	GaInNAsSb/GaNAsSb	39	2.3	1.448	1.87E-10	820°C 1minute	8.30E-08
s308	GaInNAsSb/GaNAsSb	39	2.2	1.498	2.45E-10	780°C 1minute	1.20E-07
s309	GaInNAsSb/GaNAsSb	42	2.3	1.534	1.25E-10	780°C 1minute	1.00E-07
n298	GaInNAsSb/GaAs	38	2.2	1.368	3.17E-10	800°C 1minute	7.20E-08

*Table 6. PL result summary of GaInNAs/GaAs, GaInNAs/GaNAs, GaInNAsSb/GaAs, GaInNAsSb/GaNAsSb structures.*

quantum wells. As shown in Figure 28, the photoluminescence intensity increases and FWHM decreases as the GaInNAs quantum well sample is annealed. The narrower the FWHM, the higher the quality of the quantum well. Several sources including MBE source flux fluctuation or plasma source power variation can cause non-uniformity across multiple quantum wells. This can produce multiple PL peaks. Table 6 summarizes the PL results from this work. The PL peak wavelength is in the range between 1.2  $\mu\text{m}$  and 1.6  $\mu\text{m}$  from GaInNAs/GaAs, GaInNAs/GaNAs, GaInNAsSb/GaAs, or GaInNAsSb/GaNAsSb structures. This is the broadest range of PL achieved from the dilute nitride materials systems. Figure 47 shows the PL from GaInNAsSb quantum wells with GaNAsSb barriers for various antimony fluxes. The standard luminescence at 1.3  $\mu\text{m}$  is the highest PL intensity we have achieved with the GaInNAs/GaAs combination and is presented here for comparison. Four samples with different antimony fluxes,

number of quantum wells, and different indium compositions were grown. The antimony cracking temperature for all samples was 850°C, resulting in ~30% cracking efficiency. The first sample (Figure 47 (b)) was grown with  $7.2 \times 10^{-8}$  Torr of antimony beam equivalent pressure (BEP) and the PL peak was at 1.48  $\mu\text{m}$  with 65% PL intensity of that from the standard 1.3  $\mu\text{m}$  PL sample. Increased antimony BEP of  $1.4 \times 10^{-7}$  Torr was applied to the second sample (Figure 47 (c)) with almost the same indium concentration of 38% and a dramatic decrease in photoluminescence intensity and a wavelength red-shift were observed. The peak intensity was at 1.58  $\mu\text{m}$  and the luminescence intensity was about 14% of that from the standard 1.3  $\mu\text{m}$  photoluminescence intensity. The attempts to achieve high photoluminescence intensity, while maintaining the wavelength around 1.5  $\mu\text{m}$ , led us to grow single quantum well (SQW) photoluminescence samples. The reduced interface roughness and decreased volume of highly strained material improved the photoluminescence intensity as shown in Figure 47 (d) and (e). The 10 nm thick single quantum well sample with 39% indium and an antimony pressure of  $1.2 \times 10^{-7}$  Torr showed a photoluminescence peak at 1.5  $\mu\text{m}$  with peak intensity slightly higher than the reference (Figure 47 (d)). From the 9 nm thick single quantum well structure with 42% indium and an antimony pressure of  $1.0 \times 10^{-7}$  Torr, the photoluminescence peak shifted to 1.54  $\mu\text{m}$  and the peak intensity was approximately 62% of the reference (Figure 47 (e)). These quantum wells are of excellent optical quality and represent a marked improvement over previously reported results<sup>161,162,163</sup>.

As clearly evident from the above discussion, PL is an extremely valuable material characterization technique. In this work, PL measurements always preceded device growth and study. PL was used to establish the optimum growth and *ex-situ* annealing conditions.

## 4.2 X-ray Diffraction (XRD)

X-ray diffraction measurements start from Bragg's Law:

$$n\lambda = 2d \sin \theta,$$

which was derived by the English physicists Sir W.H. Bragg and his son Sir W.L. Bragg in 1913 to explain why the cleavage faces of crystals appear to reflect X-ray beams at certain angles of incidence,  $\theta$ . The variable  $d$  is the distance between atomic layers in a crystal, and the variable  $\lambda$  is the wavelength of the incident X-ray beam, and  $n$  is an integer.

This observation is an example of X-ray wave interference, commonly known as X-ray diffraction (XRD), and was direct evidence of the periodic atomic structure of crystals, postulated for several centuries earlier. Although Bragg's law was used to explain the interference pattern of X-rays scattered by crystals, diffraction has been developed to study the structure of all states of matter with any beam, e.g., ions, electrons, neutrons, and protons, with a wavelength similar to the distance between the atomic or molecular structures of interest.

Bragg's Law can easily be derived by considering the conditions necessary to make the phases of collinear reflected beams different by an integer multiple of  $2\pi$ . The rays of the incident beam are always in phase and parallel up to the point at which the top beam strikes the top layer at atom  $z$  (Figure 48). The second beam continues to the next layer where it is scattered by atom  $B$ . The second beam must travel the extra distance  $AB + BC$  if the two beams are to continue traveling adjacent and parallel. This extra distance

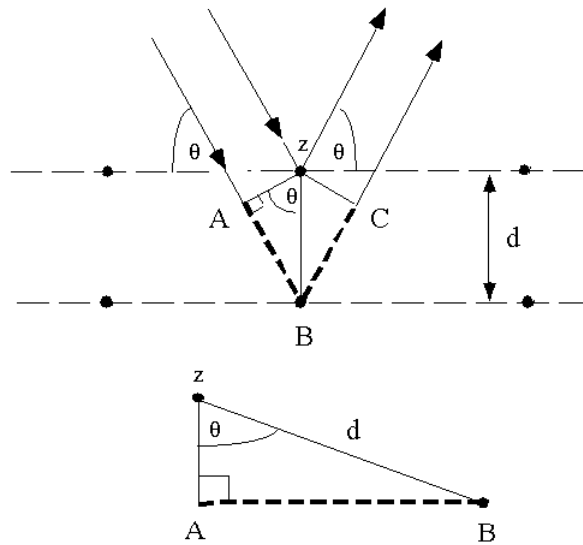


Figure 48. Deriving Bragg's Law using the reflection geometry and applying trigonometry.

must be an integral ( $n$ ) multiple of the wavelength ( $\lambda$ ) for the phases of the two beams to be the same and produce constructive or additive interference:

$$n\lambda = AB + BC$$

Recognizing  $d$  as the hypotenuse of the right triangle  $ABz$ , we can use trigonometry to relate  $d$  and  $\lambda$  to the distance  $(AB + BC)$ . The distance  $AB$  is opposite  $\theta$  so,

$$AB = d \sin\theta$$

Because  $AB = BC$  the equation above becomes,

$$n\lambda = 2AB$$

and we have,

$$n\lambda = 2d \sin\theta$$

and Bragg's Law has been derived. The location of the surface does not change the derivation of Bragg's Law.

Based on Bragg's Law derived above, XRD can measure the lattice parameter of the film. The lattice parameter is related to the position of the constructive interference X-ray peak by Bragg's law as derived earlier:

$$n\lambda = 2d_{hkl} \sin\theta$$

where  $\lambda$  is the wavelength of the used X-ray source, and  $d_{hkl}$  is the spacing between the  $hkl$  planes, which for cubic crystals is related to the lattice parameter  $a$  as,

$$\frac{1}{d_{hkl}^2} = \frac{h^2 + k^2 + l^2}{a^2}$$

All the measured films are not relaxed as indicated by the position of the film (224) peak with respect to the GaAs (224) peak. Hence, the equilibrium unstrained lattice parameter ( $a_{eq}$ ) can be calculated from the measured out-of-plane lattice parameter ( $a_{004}$ ) as,

$$\epsilon_z = 0 = 2 \cdot C_{12} \cdot \epsilon_{in\text{-}plane} + C_{11} \cdot \epsilon_{out\text{-}plane} \text{ or } a_{eq} = \frac{2 \cdot \frac{C_{12}}{C_{11}} a_{GaAs} + a_{004}}{\frac{C_{12}}{C_{11}} + 2}$$

where  $\epsilon_{in\text{-}plane}$  is the in-plane strain which is equal to  $\frac{a_{GaAs} - a_{eq}}{a_{eq}}$  if the film is not

relaxed. This means that the epitaxially-grown film thickness is within the critical

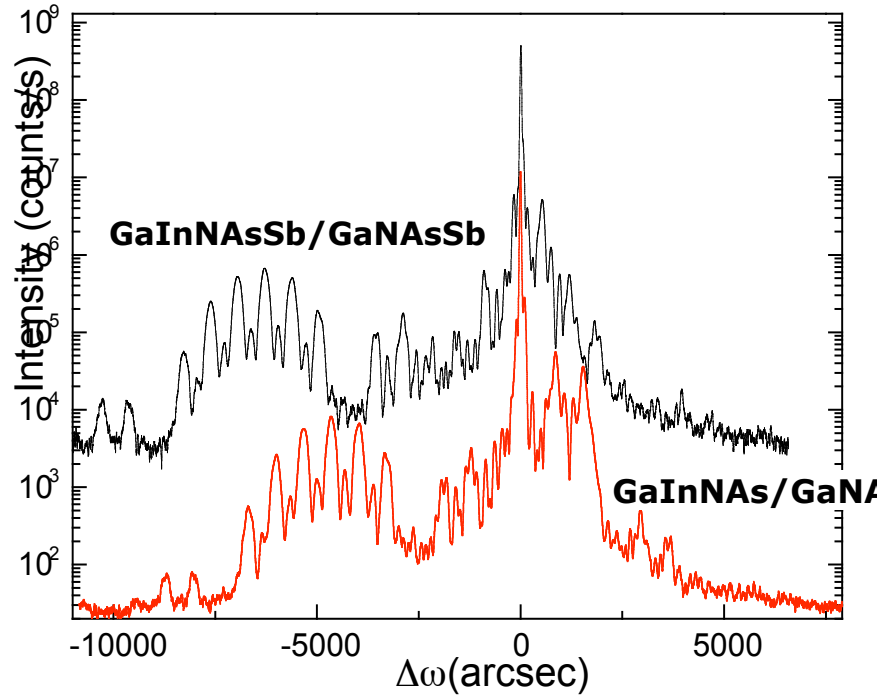


Figure 49. HRXRD result on GaInNAs/GaNAs and GaInNAsSb/GaNAsSb.

thickness, of which concept will be explained in later chapter,  $\epsilon_{out\ plane}$  is the out-of plane strain which is equal to  $\frac{a_{004} - a_{eq}}{a_{eq}}$  ( $a_{GaAs}$  is the lattice parameter of GaAs), and  $\epsilon_z$  is the strain in the out-of-plane direction.  $C_{11}$  and  $C_{12}$  are the stiffness coefficients;  $2\frac{C_{12}}{C_{11}}$  is around 0.9 for all III-V materials<sup>135</sup>. As Vegard's law is valid in the Nitride-Arsenide material system<sup>136</sup>, it can be used to calculate the nitrogen concentration from the unstrained lattice parameter as discussed in chapter 2.6.

For nitrogen concentrations below 5%, the nitrogen concentration can be calculated from the lattice parameter of the coherent nitride film. For higher nitrogen concentrations, a coherent single film is too thin for accurate analysis, in other words, too low X-ray counts. Therefore, the concentration is determined by comparing the measured XRD spectrum from a GaAs/GaNAs superlattice with a spectrum simulated from the High Resolution Simulation software supplied by Phillips<sup>137</sup>.

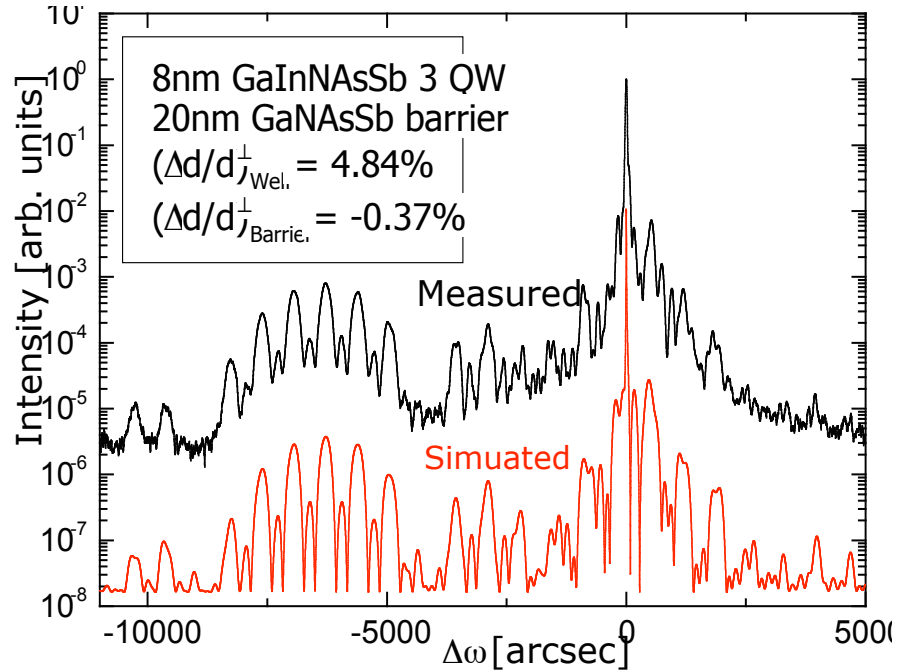


Figure 50. Comparison between HRXRD experimental result and dynamical simulation.

Figure 49 shows the  $(004)$  HRXRD pattern of GaInNAs/GaNAs and GaInNAsSb/GaNAsSb samples. Both samples have three 7 nm thick highly compressive by strained quantum wells surrounded by 20 nm tensely-strained barriers. The GaInNAsSb sample contained 37% indium, 1.2% nitrogen, and  $7.1 \times 10^{-8}$  Torr of antimony pressure and the GaInNAs contained 30% indium and 1.2% nitrogen. The broad enveloped peak at smaller angles from the GaAs substrate corresponds to the  $(004)$  diffraction from the strained quantum well and represents 3.6% and 4.53% compressive strain for the GaInNAs and GaInNAsSb QWs, respectively. The increase in compressive strain of the quantum wells comes from both the increase in indium composition and the addition of antimony. Figure 50 shows the excellent match between experimental data and simulation result. From simulation, we can conclude that there is 4.84% compressive strain in the quantum well and 0.37% tensile strain in the barrier.

### 4.3 Cathodoluminescence (CL)

Cathodoluminescence (CL) is a method conventionally used to analyze the degree of crystalline perfection in single crystalline structures<sup>138</sup>, including trace impurities, lattice defects and crystal distortion. CL spectra are obtained by incorporating an optical collecting mirror and spectrometer into either a transmission electron microscope (TEM) or a scanning electron microscope (SEM), and analyzing the emitted photons, either spectrally or the total intensity synchronized with the scanning electron beam across the entire sample. Near infrared, visible light, and near ultraviolet photons are generated when an electron beam irradiates a specimen, which is called cathodoluminescence. Characteristic X-rays mainly originate from the excitation of inner-shell electrons (100 eV to 10 keV), while CL is due to excitation of the outer electron states, valence band in a semiconductor or molecular orbital (up to several eV). In the case of a semiconductor specimen, the fundamental CL energy is equivalent to the energy gap between the conduction band and the valence band. In addition, these can be related transitions with

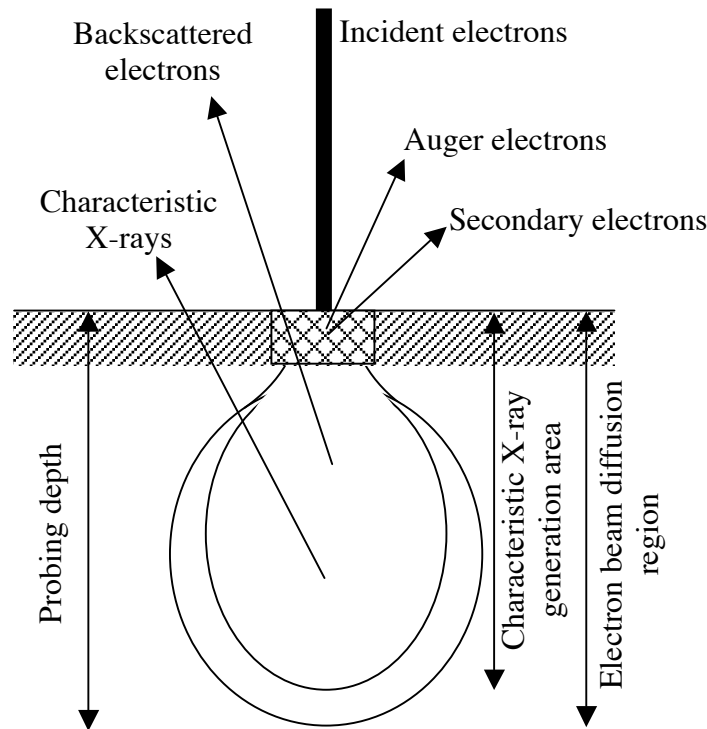


Figure 51. Various signals obtained by the electron irradiation of specimen surface and the signal detection depth.

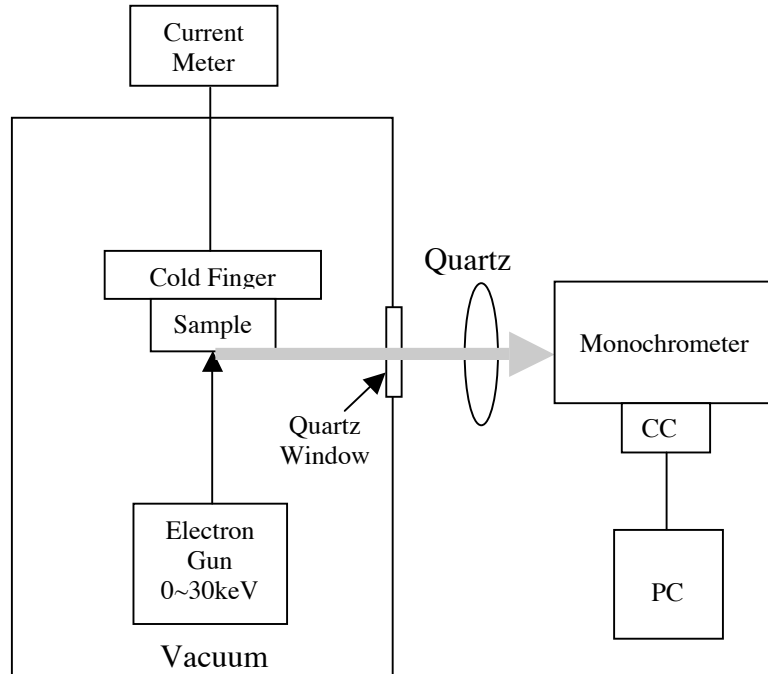


Figure 52. Schematic diagram of CL spectrometer.

nearly the same energy spectrum. Possible transitions include differences in crystal structures or compositions, the substitute of an impurity into the lattice or the generation of trapping level due to a lattice defect. The combination of these electronic transitions and accompanying light emission produce the CL signal. Figure 51<sup>139</sup> shows a schematic diagram of various signals obtained when an electron beam irradiates a specimen surface. Information in depth information can be obtained by exploiting the unique property of a variable energy electron beam to deposit energy at a depth that depends on its kinetic energy<sup>140</sup>. The following are the features of the CL technique: □

1. It is possible to analyze the distribution of trace impurities and also the distribution of defects. The sensitivity of CL is high enough to detect  $\sim 10^{17} \text{ cm}^{-3}$  impurities or defects in a semiconductor specimen.
2. It is possible to perform the measurement over a minute area that is governed by the minority carrier diffusion length in thicker samples, typically  $\sim 1 \text{ }\mu\text{m}$  in III-V compound semiconductor materials or by the sample thickness in thin TEM samples. When a CL device is installed in a TEM and the CL distribution of a

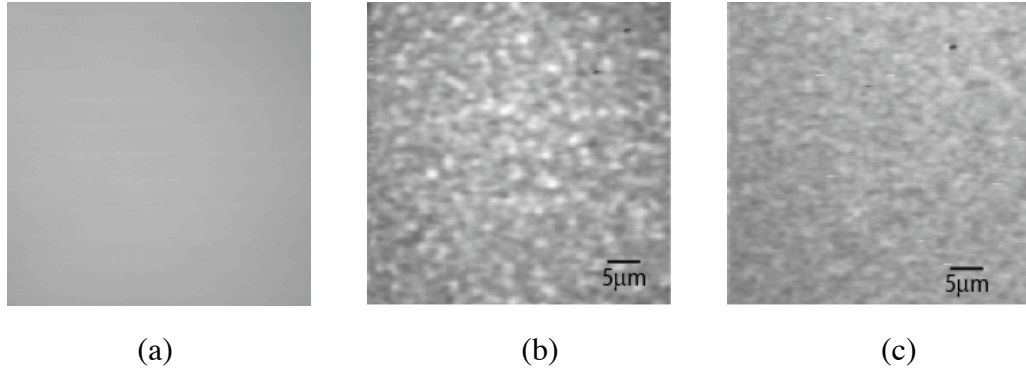


Figure 53. CL measurements of various samples. (a) GaInAs with photoluminescence peak at 980 nm, (b) GaInNAs with photoluminescence peak 1.3  $\mu\text{m}$ , (c) GaInNAsSb with photoluminescence peak with 1.48  $\mu\text{m}$ .

thin-section specimen is observed, the area of scattered electrons in the thin film is small, the spatial resolution of the order of a few nanometers can be obtained. Our samples were in this thin film configuration with high spatial resolution.

Figure 52 shows the typical CL spectrometer setup. The electron beam excitation spot may be either focused to a small spot or defocused to illuminate a large area. Spectra are acquired by a CCD array camera mounted at the exit of the monochromator. The image from this CCD is sent to the computer for further data analysis.

Figure 53 shows CL measurements done on GaInAs, GaInNAs, and GaInNAsSb QW samples at 4K. GaInAs, with a PL peak at 980 nm, has very uniform luminescence across the sample. However a GaInNAs QW, with 1.3  $\mu\text{m}$  room temperature photoluminescence peak, shows a significant degree of graininess and fluctuation of luminescence from the QW across its surface. The contrast on CL represents either non-uniform wavelength in the luminescence or significant non-radiative recombination due to defects. The greater the contrast ratio, the greater the luminescence change on surface. This is supported by the low temperature CL spectrum, on the same sample, shown in Figure 54. The CL spectrum shows two peaks with possibilities of phase segregation or non-planar growth. However, as antimony is introduced into GaInNAs, this improves the surface uniformity and the contrast variation decreases. CL is done on both as-grown and annealed samples, as shown in Figure 55, to identify the effect of annealing on QW uniformity. The improvement of luminescence uniformity is quite noticeable after

annealing. This result is supported by atomic force microscopy (AFM) images shown in Figure 56. Although the GaInNAsSb sample has a higher indium concentration (40%) than that of GaInNAs (33%), the surface roughness of GaInNAsSb is smaller (1 nm)

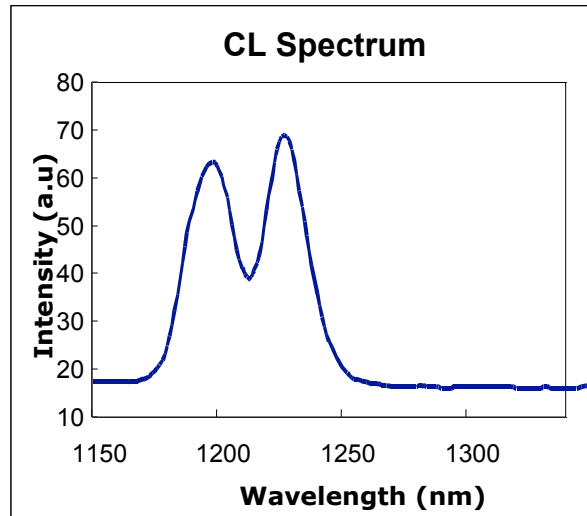


Figure 54. CL spectrum of a GaInNAs sample at 4K.

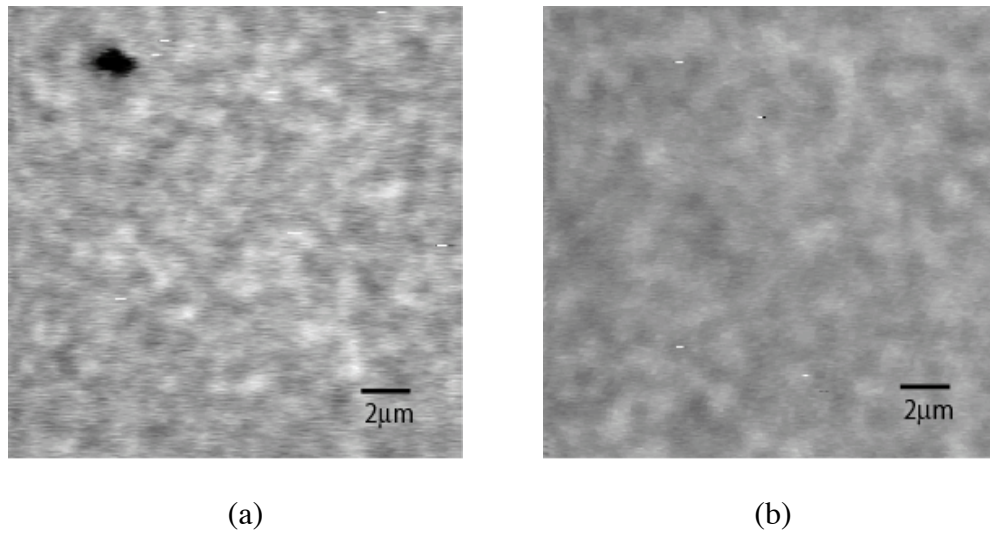


Figure 55. CL on GaInNAs samples (a) as grown and (b) annealed at 780°C for 1 minute. compared to that of GaInNAs (3 nm).

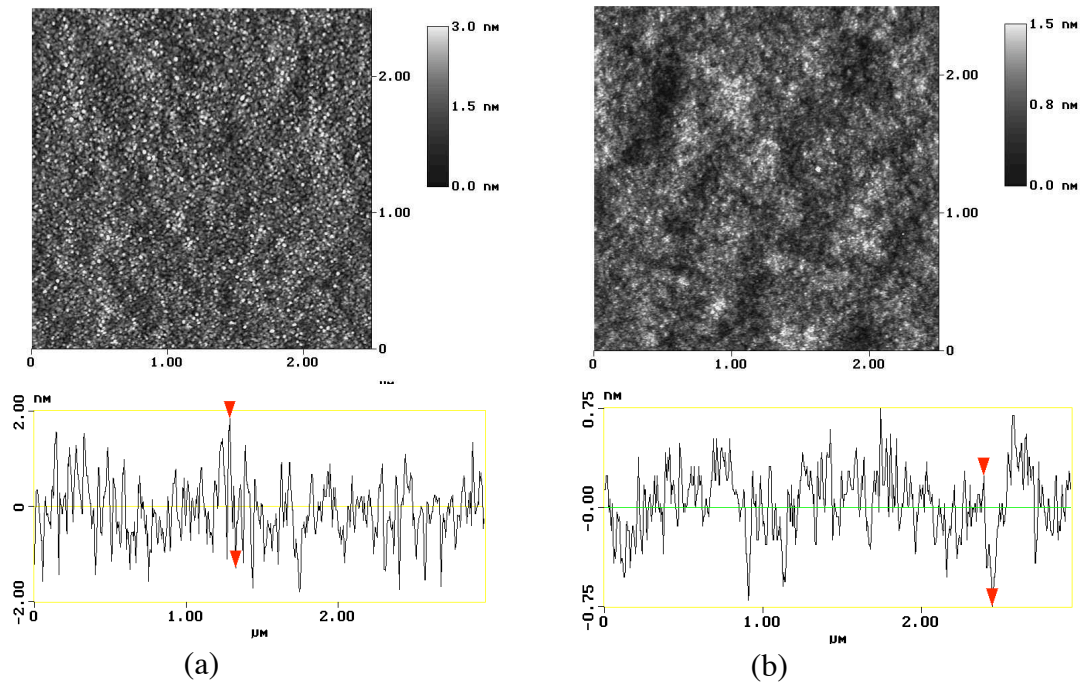


Figure 56. AFM images of (a) a  $Ga_{0.67}In_{0.33}N_{0.02}As_{0.98}$  QW surface and (b) a  $Ga_{0.6}In_{0.4}N_{0.022}AsSb$  QW surface.

## 4.4 Secondary Ion Mass Spectrometry (SIMS)

Secondary ion mass spectrometry (SIMS) is a characterization method in which a primary ion beam bombards the sample surface and the emitted secondary ions are analyzed by mass spectrometry as shown in Figure 57. SIMS is widely used for analysis of trace elements in solid materials, especially semiconductors and thin films.

The SIMS primary ion beam can be focused to less than 1  $\mu\text{m}$  in diameter. Controlling where the primary ion beam strikes the sample surface provides for microanalysis, the measurement of the lateral distribution of elements on a microscopic scale. During SIMS analysis, the sample surface is slowly sputtered away. Continuous analysis while sputtering produces information as a function of depth, called a depth profile. When the sputtering rate is extremely slow, the entire analysis can be performed while consuming less than a tenth of an atomic monolayer. This slow sputtering mode is called static SIMS in contrast to dynamic SIMS used for depth profiles. Sputter rates in typical SIMS experiments vary between 0.5 and 5 nm/s. Sputter rates depend on primary beam intensity, sample material, and crystal orientation.

The ion beam sputtering generates bombarding primary ion beam and in consequence this produces monatomic and polyatomic particles of sample material and re-sputtered primary ions, along with electrons and photons. The secondary particles

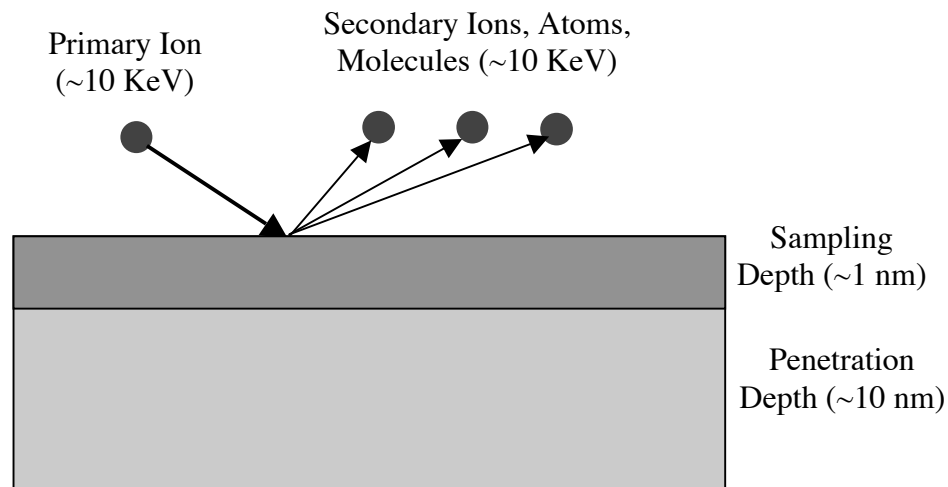


Figure 57. Sputtering effects of SIMS

carry negative, positive, and neutral charges and they have kinetic energies that range from zero to several hundred eV. Primary beam species useful in SIMS include Cs<sup>+</sup>, O<sub>2</sub><sup>+</sup>, O, Ar<sup>+</sup>, and Ga<sup>+</sup> at energies between 1 and 30 keV. Primary ions, particularly when high energies are used, are implanted and mix with sample atoms of depths of 1 to 10 nm and can provide interference effects with the desired analysis.

The SIMS ionization efficiency is called ion yield, defined as the fraction of sputtered atoms that become ionized. Ion yields vary over many orders of magnitude for the various elements. The most obvious influences on ion yield are ionization potential for positive ions and electron affinity for negative ions.

The SIMS detection limits for most trace elements are between  $1 \cdot 10^{12}$  and  $1 \cdot 10^{16}$  atoms/cc. In addition to ionization efficiencies, two other factors can limit sensitivity. The output of an electron multiplier is called dark counts or dark current if no secondary ions are striking it. This dark current arises from stray ions and electrons in the instrument vacuum systems, and from cosmic rays. Count rate limited sensitivity occurs when sputtering produces a lower secondary ion signal than the detector dark current. If the SIMS instrument itself introduces the analyte element, then the introduced level constitutes background limited sensitivity. Oxygen, present as residual gas in vacuum systems, is an example of an element with background limited sensitivity. Analyte atoms sputtered from mass spectrometer parts back onto the sample by secondary ions constitute another source of background. Mass interferences also cause background limited sensitivity.

Monitoring the secondary ion count rate of selected elements as a function of time leads to depth profiles. To convert the time axis into depth, the SIMS analyst uses a profilometer to measure the sputter crater depth. A profilometer is a separate instrument that determines depth by dragging a stylus across the crater and noting vertical deflections. Total crater depth divided by total sputter time provides the average sputter rate. Relative elemental sensitivity factors are then used to convert the vertical axis from ion counts into concentration.

Depth resolution depends on flat bottom craters. Modern instruments provide uniform sputter currents by sweeping a finely focused primary beam in a raster pattern

over a square area. In some instruments, apertures select secondary ions from the crater bottoms, but not the edges. Alternatively, the data processing system ignores all secondary ions produced when the primary sputter beam is at the ends of its raster pattern.

Mass spectra sample the secondary ions in a pre-selected mass range by continuously monitoring the ion signal while scanning a range of mass-to-charge ( $m/z$ ) ratios. The mass analyzer can be either a magnetic sector or a quadrupole. The mass spectrum detects both atomic and molecular ions. Secondary ions containing more than one atom are called molecular ions in SIMS.

The mass analyzer must be scanned in small steps to insure that all mass-to-charge ( $m/z$ ) ratios are sampled. Ten steps per mass unit are common. At higher mass resolution, ten mass increments per peak width adequately define the peak shape. A mass spectrum with a mass range of 100 has at least 1000 data channels, for which a reasonable analysis time is 0.1 second per channel. The ion intensities in data reflect the isotopic abundances of the elements.

SIMS measurements were utilized to find out the exact concentration of each

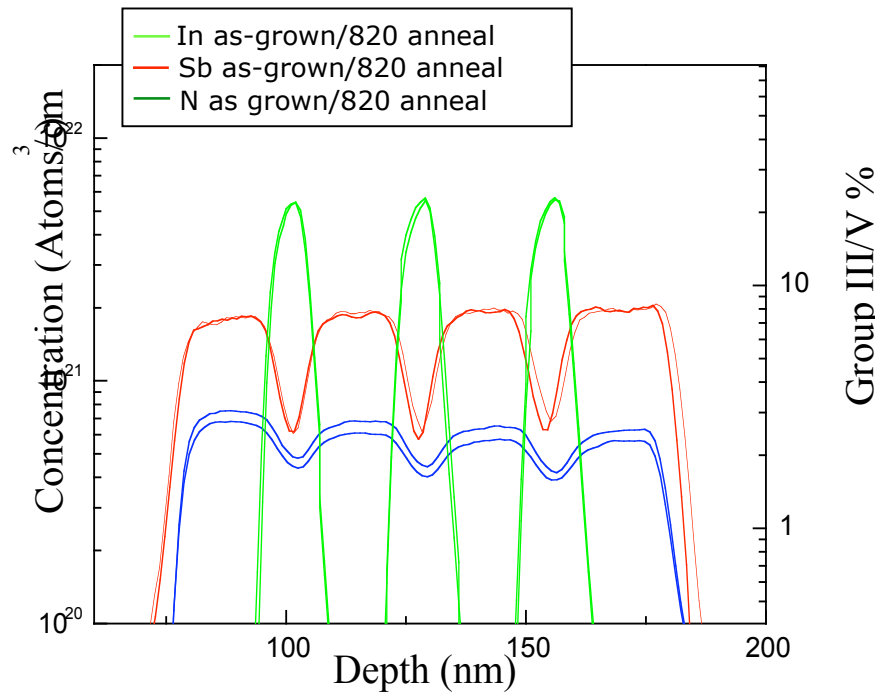


Figure 58. SIMS spectra on GaInNAsSb sample before annealing and after annealing

constituent element of the materials for this work. The acquired data were used to correlate the growth condition and concentrations of the nitrogen and antimony, which are hard to observe by normal measurement methods. A typical spectrum illustrating GaInNAsSb QWs and GaNAsSb barriers is shown in Figure 58. Several SIMS data on our materials can be found throughout this thesis.

## CHAPTER 5: GaInNAs and GaInNAsSb Ridge Waveguide Edge Emitting Laser

In this chapter, the design of GaInNAs and GaInNAsSb edge emitting lasers will be introduced. First, the fundamental calculations of unstrained and strained quantum wells will be described and then the growth and fabrication of lasers with different wavelengths will be discussed. The electrical and optical characteristics of long wavelength lasers will be shown.

### 5.1 Quantum Well Modeling

The modeling of the laser begins with the most basic calculation of a square quantum well (QW) with infinite barriers. In a square quantum well with a barrier potential  $V_o$ , the one-dimensional time-independent Schrödinger equation can be written<sup>133</sup>,

$$\frac{\hbar^2}{2m} \frac{d^2 \psi(z)}{dz^2} + V(z) \psi(z) = E \psi(z).$$

If we first assume the infinite potential barrier, the wave function should be zero at the boundaries,  $\psi_n(0) = \psi_n(L) = 0$  where  $L$  is the length of the quantum well. The solution for this infinite barrier model is then,

$$\psi_n(z) = \sqrt{\frac{2}{L}} \sin\left(\frac{n\pi}{L} z\right) \quad n = 1, 2, 3, \dots$$

with this solution, the energy of the  $n^{\text{th}}$  eigen state,  $E_n$ , is,

$$E_n = \frac{\hbar^2}{2m} \left(\frac{n\pi}{L}\right)^2, \quad k_z = \frac{n\pi}{L}.$$

Therefore, we find that the wave number,  $k_z$ , in the  $z$ -direction and  $E_n$  are quantized. The wave function was normalized to satisfy  $\int_0^L |\psi_n(z)|^2 dz = 1$ .

If the origin of the coordinate  $z = 0$  is chosen at the center of the well, as shown in Figure 59,  $V(+z) = V(-z)$ , the solution can be expressed as even and odd functions,

$$\psi_n(z) = \begin{cases} \sqrt{\frac{2}{L}} \sin\left(\frac{n\pi}{L} z\right) & n \text{ even} \\ \sqrt{\frac{2}{L}} \cos\left(\frac{n\pi}{L} z\right) & n \text{ odd} \end{cases}$$

where the solution satisfies  $\psi\left(\pm\frac{L}{2}\right) = \psi\left(\pm\frac{L}{2}\right) = 0$ . The complete three-dimensional solution, with confinement in only the  $z$ -direction, can be solved from,

$$\left[ -\frac{\hbar^2}{2m} \nabla^2 + V(z) \right] \psi(x, y, z) = E \psi(x, y, z)$$

and the normalized wave function is,

$$\psi(x, y, z) = \frac{e^{ik_x x + ik_y y}}{\sqrt{A}} \psi_n(z), \quad E = \frac{\hbar^2}{2m} (k_x^2 + k_y^2) + \left(\frac{n\pi}{L}\right)^2 \frac{\hbar^2}{2m}$$

where  $A$  is the cross-sectional area in the  $x$ - $y$  plane.

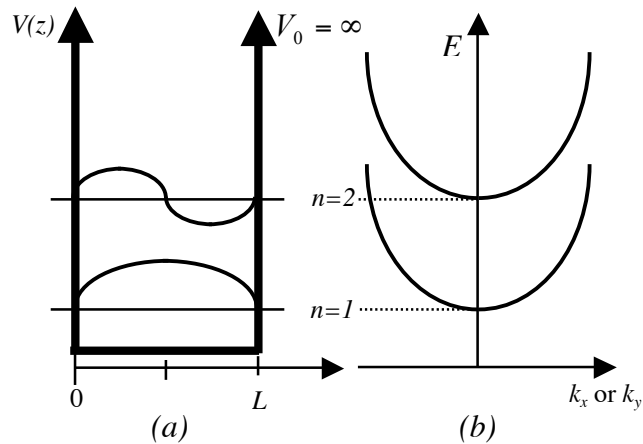


Figure 59. (a) quantum well of width  $L$  and a barrier  $V_0 = \dots$ . (b) The energy dispersion in the  $k_x$  or  $k_y$  space<sup>131</sup>.

A quantum well with finite barriers needs to be modeled to approach real semiconductor quantum well problems. As shown in Figure 60,  $V(z)$  is defined as,

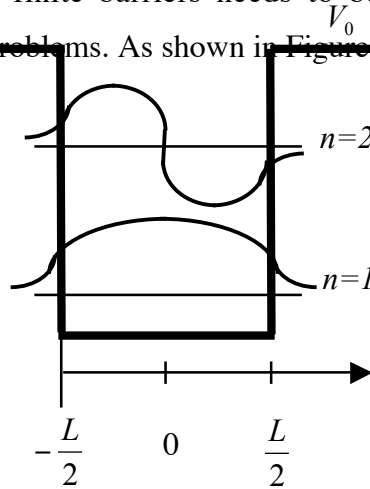
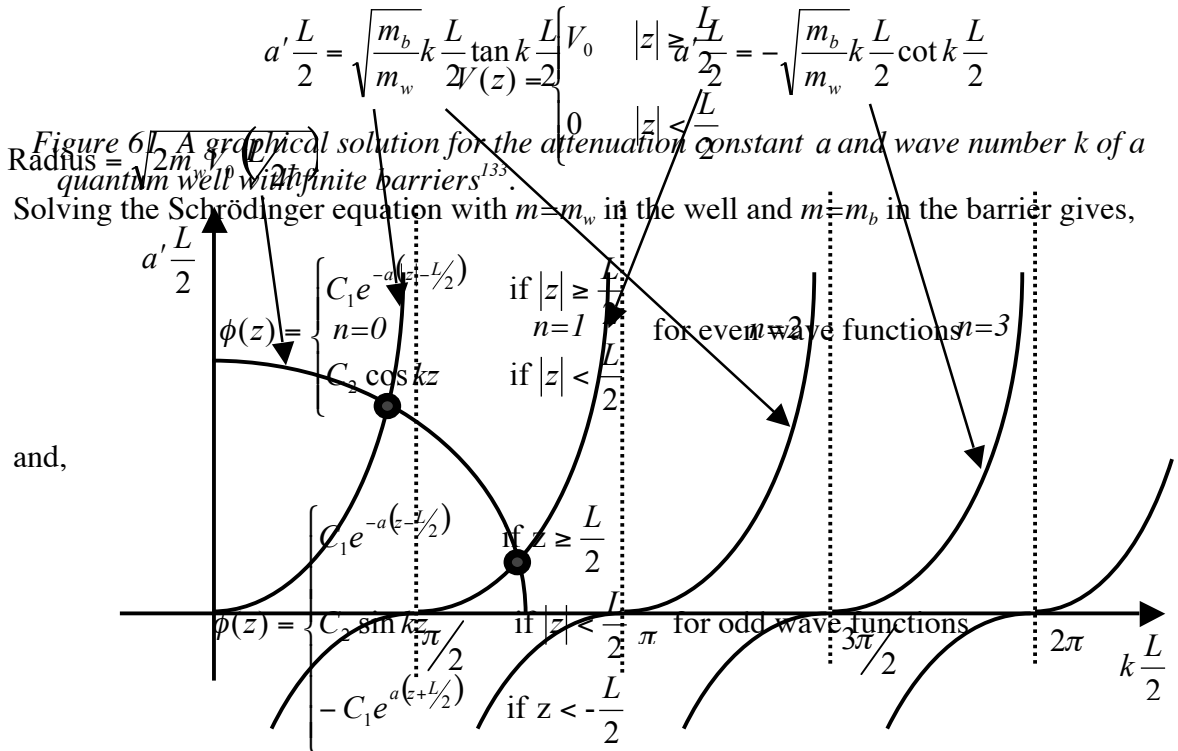


Figure 60. A quantum well with a width  $L$  and a finite barrier height  $V_0$ .



with  $k = \frac{\sqrt{2m_w E}}{\hbar}$  and  $a = \frac{\sqrt{2m_b (V_0 - E)}}{\hbar}$ .

The boundary conditions require that the wave function and its first derivative divided by the effective mass are continuous at the interface between the barrier and the well,

$$\psi\left(\frac{L^+}{2}\right) = \psi\left(\frac{L^0}{2}\right) \text{ and } \frac{1}{m_b} \frac{d\psi}{dz}\bigg|_{\frac{L^+}{2}} = \frac{1}{m_w} \frac{d\psi}{dz}\bigg|_{\frac{L^0}{2}}$$

These boundary conditions are satisfied when,

$$a = \frac{m_b k}{m_w} \tan k \frac{L}{2} \text{ for the even wave functions}$$

and when,

$$a = -\frac{m_b k}{m_w} \cot k \frac{L}{2} \text{ for the odd wave functions}$$

The solutions for the eigen energies in a quantum well with finite barriers can be obtained graphically as shown in Figure 61 from,

$$k \frac{L}{2} + a \frac{L}{2} = \frac{2m_w V_0}{\hbar^2} \frac{L}{2}$$

and,

$$a \frac{L}{2} = \sqrt{\frac{m_b}{m_w}} k \frac{L}{2} \tan k \frac{L}{2} \text{ for the even wave functions}$$

$$a \frac{L}{2} = -\sqrt{\frac{m_b}{m_w}} k \frac{L}{2} \cot k \frac{L}{2} \text{ for the odd wave functions}$$

with  $a = a \sqrt{\frac{m_w}{m_b}}$ . These solutions for  $k$  and  $E$  are smaller than for a quantum well with infinite barriers. The reduced carrier confinement results in a decrease of the energy levels as if the quantum well was widened. Indeed, for the case of  $m_w = m_b = m$  the solutions for the energy and the wave functions are<sup>133</sup>,

$$E_n = \frac{\hbar^2}{2m} \left(\frac{n\pi}{L_{eff}}\right)^2 \text{ and } \psi_n(z) = \sqrt{\frac{2}{L_{eff}}} \sin\left(\frac{n\pi}{L_{eff}} z\right) \text{ with } L_{eff} = L + \frac{2}{a}.$$

The electron density,  $n$ , in a quantum well with infinite barrier can be calculated by,

$$n = \frac{2}{V} \int_n \int_{k_x} \int_{k_y} P(E)$$

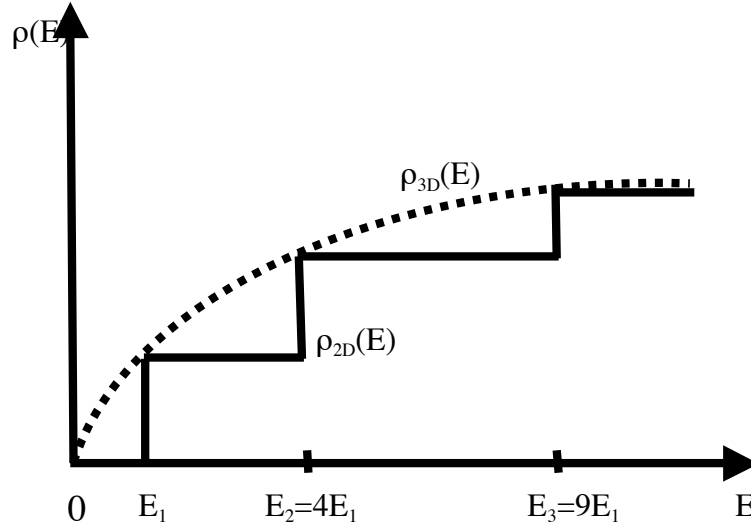


Figure 62. The electron density of states  $g_{2D}(E)$  (solid line) for a two-dimensional quantum well structure compared with the three-dimensional density of states  $g_{3D}(E)$  (dashed curve).

with the summation over all the occupied sub-bands. By converting the sum to an integral so that,

$$n = \int dE g_{2D}(E) P(E)$$

we find the two dimensional density of states,

$$g_{2D}(E) = \frac{m}{\hbar^2 L_z} \sum_n H(E - E_n)$$

with  $E_n$  is defined as  $\frac{\hbar^2}{2m} \left( \frac{n\pi}{L} \right)^2$ , and  $H(x)$  a Heaviside step function  $H(x)=1$  for  $x>0$  and

$H(x)=0$  for  $x<0$ . When the energy is equal to  $E_n$ , the three-dimensional density of states,

$$g_{3D}(E) = \frac{1}{2\pi^2} \left( \frac{2m}{\hbar^2} \right)^{3/2} \sqrt{E}, \text{ and the two dimensional density of states, } g_{2D}(E), \text{ coincide.}$$

A schematic diagram of  $g_{2D}(E)$  and  $g_{3D}(E)$  is shown in Figure 62.

## 5.2 Electron Energy Levels in Strained Quantum Wells

When GaInAs, GaInNAs and GaInNAsSb are grown pseudomorphically on GaAs, these layers are biaxially strained because the lattice constants of these materials

are different from that of GaAs. Pseudomorphic growth means that a material with different lattice constant from that of substrate can be grown in thin strained layers without introducing dislocations within certain limitations of composition and thickness. The lattice constants of GaAs, AlAs, InAs and their alloys versus the band gap energy along with other important semiconductors were shown in Figure 1. The lattice constants of GaAs and AlAs differ only slightly, which is 5.65Å and 5.66Å respectively. Therefore AlGaAs can be grown in almost any arbitrary thicknesses on GaAs for all Al contents without introducing dislocations in the crystal and the critical thickness is almost infinite. The lattice constant of InAs (6.06Å) is significantly larger than that of GaAs (5.65Å) and therefore, unlike AlGaAs, GaInAs can only be grown in limited thicknesses. Like GaInAs, GaInNAs and GaInNAsSb quantum wells for lasers are usually grown under compressive strain. Compressive strain causes an increase in  $E_g$ , which opposes the desired reduction in  $E_g$  with increasing indium mole fraction, i.e. the reduction of  $E_g$  is partially canceled by the strain effect. The strained band gap energy  $E_g^{str}$  can be calculated by<sup>141</sup>;

$$E_g^{str} = E_g + \Delta E_h \pm \Delta E_s$$

where the hydrostatic portion  $\Delta E_h$  of the energy shift reads,

$$\Delta E_h = \frac{2 \cdot d_1 \cdot (C_{11} - C_{12})}{C_{11}}$$

and the uniaxial contribution  $\Delta E_s$  of the energy shift reads,

$$\Delta E_s = \pm d_2 \cdot \frac{C_{11} + 2 \cdot C_{12}}{C_{11}}$$

The values of the lattice constants  $a$ , the deformation potentials  $d_1$  and  $d_2$  as well as the elastic constants  $C_{11}$  and  $C_{12}$  for GaAs and InAs, respectively, can be found in Table 7. The values for GaInAs are obtained by linear interpolation between the numbers for the binary materials and the values for GaInNAs and GaInNAsSb can be calculated from ternary and quaternary values, respectively.

$d_{1 \text{ GaAs}}$ [eV]	$d_{2 \text{ GaAs}}$ [eV]	$d_{1 \text{ InAs}}$ [eV]	$d_{2 \text{ InAs}}$ [eV]	$a_{\text{ GaAs}}$ [nm]
-8.68	-1.7	-5.91	-1.8	0.565

Table 7. Important semiconductor parameters<sup>142</sup>.

Due to the uniaxial strain, the degeneracy of the valence band is removed. The positive sign in the equation for  $\Delta E_s$  holds for the shift of the heavy hole band and the negative sign for the shift of the light hole band. The investigations on strain dependence of the band discontinuities in the literature are contradictory<sup>143,144,145</sup>. Because no consistent results could be found in the literature, 60% of the energy difference between the conduction band and 40% difference in the heavy hole valence band is generally assumed for  $\Delta E_c$  and  $\Delta E_v$  between GaAs and GaInAs as well as for the heterojunction between AlGaAs and GaInAs. On the other hand, the conduction band gap offset of as high as 85% of band gap difference has been reported between GaInNAs and GaAs<sup>55</sup>.

In a quantum well, the continuous energy levels of the conduction band split into discrete levels. The energy levels  $E_e$  can be calculated by solving the Schrödinger equation for a single potential well with finite barrier height. The symmetrical part of the solution is given by;

$$\sqrt{\frac{E_e}{m_{QW}}} \cdot \tan\left[\sqrt{2 \cdot m_{QW} \cdot E_e} \cdot \frac{\Delta \cdot d_c}{h}\right] = \sqrt{\frac{\Delta E_c - E_e}{m_{Barrier}}}$$

which reveals the lowest energy  $E_e$ , i.e. the ground state of the quantum levels in the potential well. In the equation above,  $d_c$  is the thickness of the quantum well, and  $h$  is Planck's constant, and  $m_{Barrier}$  and  $m_{QW}$  are the effective masses of the barrier and quantum well materials, respectively.

To account for strain and quantum effects, an effective band gap  $E_g|_{eff}$  and, therefore, an effective conduction band offset  $\Delta E_c|_{eff}$  needs to be calculated separately according to equations listed above as shown in Figure 63. The unstrained conduction band offset  $\Delta E_c|_{unstrained}$  is reduced by the bandgap shift due to strain and the quantization of the electron energy in the quantum well. Given the critical thickness,  $d_{cr}$ , of a quantum well, the quantum level of electrons  $E_e$  can be calculated with the critical thickness  $d_{cr}$ .

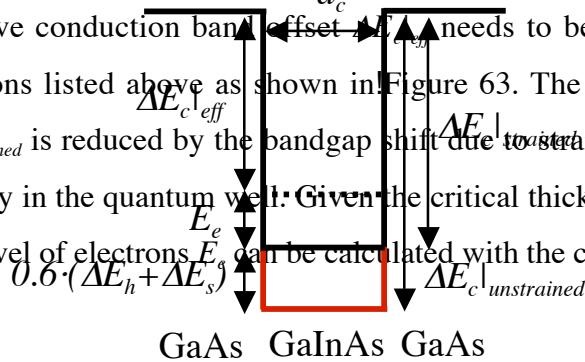


Figure 63. Conduction band diagram of a strained GaInAs quantum well with GaAs barriers.

Having a high conduction band offset,  $\Delta E_c$ , between quantum well and barriers is essential for good laser performance. This is because higher  $\Delta E_c$  provides better electron confinement, which increases both the efficiency of the laser and the characteristic temperature,  $T_o$ . As electrons are injected into the quantum well, some are captured and recombine with holes in the valence band of the quantum well and generate photons. Others do not and they either recombine non-radiatively or escape. All non-radiative recombination contributes to loss and decreases efficiency of a laser. By confining the electrons in a quantum well with bigger  $\Delta E_c$ , the efficiency of a laser can be improved. With this larger  $\Delta E_c$ , electrons are also well retained in the quantum well, even at high temperature and the quantum well lasers are less sensitive to environmental temperature change. In other words, if the average thermal energy of an electron,  $\frac{kT}{q}$ , is a few times smaller than  $\Delta E_c$ , the characteristic temperature,  $T_o$ , is generally high.

However, a larger  $\Delta E_c$  means a smaller  $\Delta E_v$  and less confinement for holes in valence band. Even under compressively strained quantum well conditions, the electron effective mass is still several times lighter than that of heavy holes, so the confinement of electrons is far more important than that of holes. Since heavy holes have low mobility, it is difficult to overcome the valence band offset,  $\Delta E_v$ , and this makes it very difficult to design a multiple quantum well structure. The first few quantum wells will be provided with holes, but the remaining quantum wells will not be easily filled up with holes due to their heavy effective mass. This means that the laser will have large gain in only the first few quantum wells from the p-doped side but not from all its quantum wells. By reducing the  $\Delta E_v$ , holes can be transferred better into the next quantum well. Therefore, a large  $\Delta E_c$  has merits for high power laser structures.

To obtain a high conduction band offset,  $\Delta E_c$ , between quantum wells and barriers, either the indium or nitrogen composition can be increased to increase  $\Delta E_g$ . High indium composition is more preferable than high nitrogen as explained in Chapter 2. Unfortunately, the maximum indium mole fraction in the epitaxial film is limited by the concentration of nitrogen while still maintaining near lattice match to the GaAs substrate.

The limitations of the indium content and the corresponding maximum thickness of the layers are given by the critical thickness ( $d_{cr}$ ). If GaInAs and GaInNAs layers are grown above  $d_{cr}$ , an increased dislocation density from lattice relaxation occurs. The critical thickness,  $d_{cr}$ , can be calculated according to the theory of Matthews and Blakeslee<sup>146,147,148</sup> by,

$$d_{cr} = \frac{1}{2} \cdot \frac{a_s \cdot \left[ \frac{1}{4} \cdot \epsilon_L \right]}{\epsilon \cdot (1 + \epsilon_L) \cdot \epsilon} + \ln \frac{\sqrt{2} \cdot d_{cr}}{a_s}$$

where  $a_s$  is the lattice constant of the unstrained substrate. The in-plane strain  $\epsilon$  is given by,

$$\epsilon = \frac{a_s - a_{GaInNAs}}{a_{GaInNAs}}$$

and  $\epsilon_L$  is given by,

$$\epsilon_L = \frac{C_{12}^{GaInNAs}}{C_{11}^{GaInNAs} + C_{12}^{GaInNAs}}$$

The elastic constants  $C_{11}$  and  $C_{12}$  of GaInNAs can be calculated by linear interpolation of the binary values of GaNAs and GaInAs.

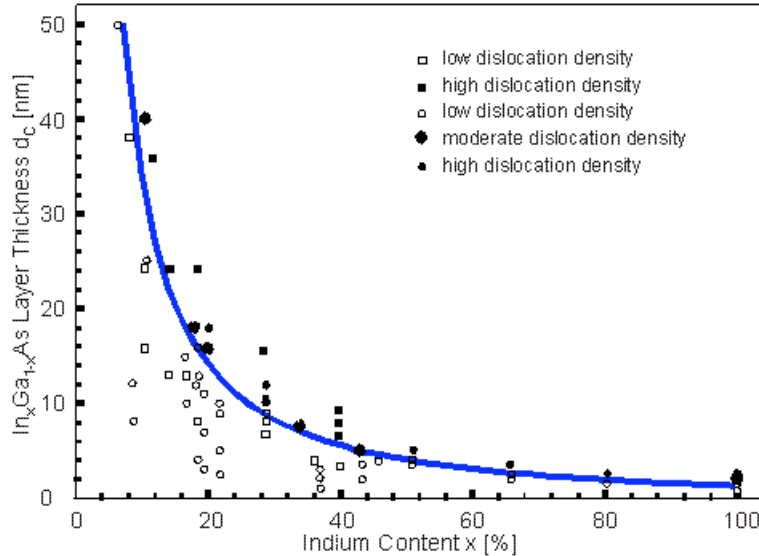


Figure 64. Critical thickness vs. In concentration in GaAs/ $In_xGa_{1-x}As$ /GaAs single quantum well according to the theory of Matthews and Blakeslee is shown as bold line. Data points for different dislocation are shown in different symbols<sup>146</sup>.

In Figure 64, the solutions for the critical thickness  $d_{cr}$  for GaInAs are shown. The theory of Matthews and Blakeslee is confirmed by various data from the literature. Samples below the critical thickness exhibit low dislocation density whereas samples above the critical thickness show a high dislocation density; i.e. the strained layer starts to relax. The large solid circles in Figure 64 represent samples with moderate dislocation density. This result shows that the transition from pseudomorphic growth to relaxation is not abrupt.

## 5.3 Band Gap Energy Calculations of Dilute Nitride Materials

### 5.3.1 Bandgap Calculation of GaNAs

As shown in Figure 1, dilute nitride materials have a huge bandgap energy bowing; meaning the bandgap is very non-linear with composition. Therefore, the common method to get the bandgap energy of ternary material by linear interpolation between two bandgap energies of binary materials does not apply for dilute nitride material. Due to this property, GaNAs is supposed to be a metal over a certain range of nitrogen, even though both GaAs and GaN are semiconductor materials. This bandgap bowing relation is usually expressed by the parabolic function,

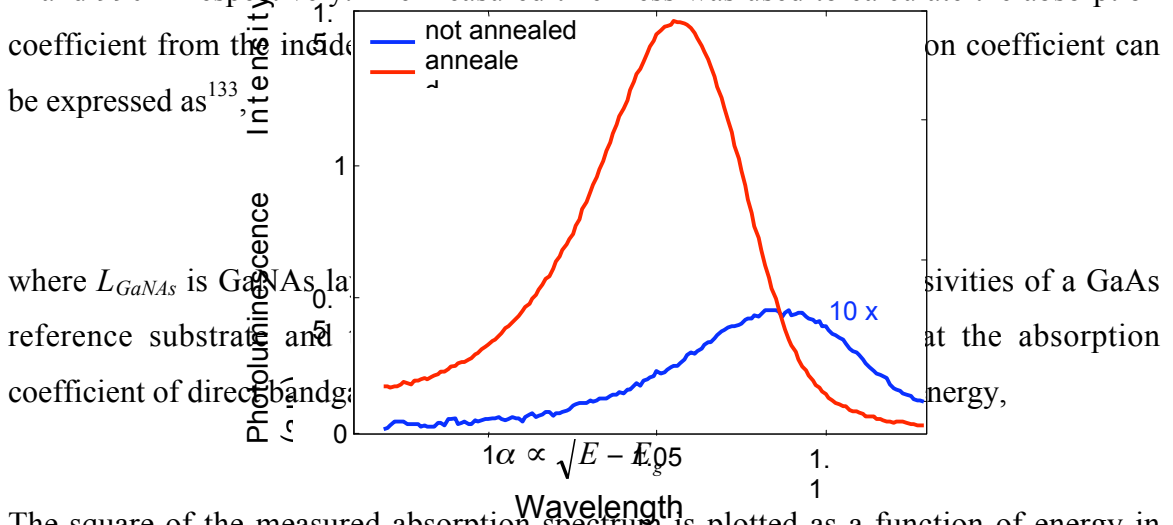
$$E_g(x) = a + bx + cx(x \square 1)$$

where  $c (>0)$  is called the bowing parameter, or  $c = \frac{\partial^2 E_g}{\partial x^2}$ .

Weyer *et. al.* found the large bandgap bowing in GaNAs/GaAs in 1992<sup>50</sup>. Sakai *et. al.* have calculated the bandgap energy and bandgap bowing of GaNAs using dielectric band theory<sup>51</sup>. The dielectric band theory is based on the differences of electron negativity of group III and group V atoms<sup>50,52</sup>. Wei *et. al.* calculated the bandgap of GaNAs alloys using a local density approximation using first principle calculation<sup>130</sup>.

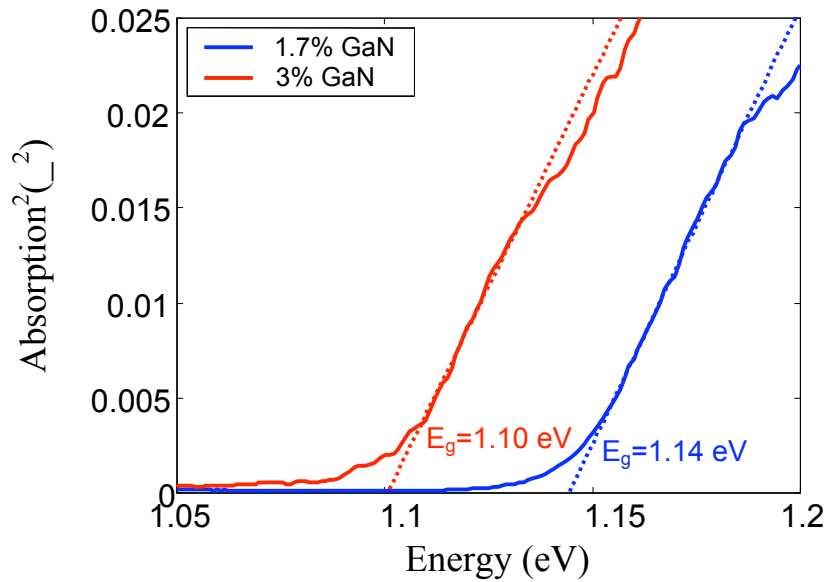
The bandgap of GaNAs on GaAs was evaluated from absorption measurements by a previous student, S. Spruytte<sup>67</sup>. Two samples, 2000 Å thick GaN<sub>0.017</sub>As<sub>0.983</sub> and 1000 Å thick GaN<sub>0.03</sub>As<sub>0.97</sub> were grown on GaAs substrates. The actual thickness of these films was measured by high resolution X-ray diffraction (HRXRD) and were found to be 2185

Å and 990 Å respectively. The measured thickness was used to calculate the absorption coefficient from the incident intensity. The absorption coefficient can be expressed as<sup>133</sup>



where  $L_{GaNAs}$  is GaNAs layer thickness,  $L_{GaAs}$  is GaAs reference substrate thickness, and  $\alpha$  is the absorption coefficient of direct bandgap GaAs.

The square of the measured absorption spectrum is plotted as a function of energy in Figure 65. The linear relationship between the square of the absorption coefficient and energy shows that GaNAs is direct transition semiconductor. The linear extrapolation intercept of the absorption curve at x-axis shows the bandgap energy of the each material,



which is 1.14 eV for  $GaN_{0.017}As_{0.983}$  and 1.1 eV for  $GaN_{0.03}As_{0.97}$ . From this result, it can be concluded that the dependence of the bandgap energy on the nitrogen concentration is approximately -100 meV/nitrogen mole fraction %. Using this experimental data, we can

Figure 65. Absorption measurements from  $GaN_{0.017}As_{0.983}$  and  $GaN_{0.03}As_{0.97}$ .

determine the coefficients for  $\text{GaN}_x\text{As}_{1-x}$  bandgap calculation and  $E_g$  can be described as,

$$E_g(x) = 1.424 - 24.43x + 454.3x^2 \quad (x < 0.03)$$

The photoluminescence spectrum was also obtained for  $\text{GaN}_{0.02}\text{As}_{0.98}$ , as described in Chapter 4-1, and it is shown in Figure 66. The calculated band gap energy of  $\text{GaN}_{0.02}\text{As}_{0.98}$  is 1.12 eV, which corresponds to 1.1  $\mu\text{m}$ . The as-grown sample clearly shows photoluminescence peak at 1.1  $\mu\text{m}$  and this red-shift of photoluminescence peak (1.424 eV - 1.12 eV = 0.304 eV) from the GaAs peak at 1.424 eV is due to nitrogen incorporation. The blue-shift due to annealing is shown in Figure 65 and this phenomenon was explained at Chapter 3.2.

The band lineups of GaNAs and GaInNAs were calculated by Kondow and Uomi based on the dielectric band theory of Sakai *et al.* and they found that the bandgap difference,  $\Delta E_g$ , mainly contributes to the conduction band offset,  $\Delta E_c$ , and hardly affects the valence band offset,  $\Delta E_v$ <sup>54</sup>. Based on this result, they have proposed that GaInNAs QWs would be much less temperature sensitive compared to GaInAsP for long wavelength emission due to its larger conduction band offset to GaAs. Wei and Zunger calculated the composition dependence of the bowing parameter of GaNAs alloys by local density approximation (LDA) using first principle calculations<sup>130</sup>. Their results concluded that the composition dependence of the bowing parameter is divided into two regions, (a) an impurity-like region where the bowing parameter is relatively large and composition dependent, (b) a band-like-region where the bowing parameter is small and nearly constant. The calculated bowing parameter was 16 eV for bulk  $\text{GaN}_{0.125}\text{As}_{0.875}$  and 7 eV for bulk  $\text{GaN}_{0.5}\text{As}_{0.5}$ . Later, Bellaiche, Wei, and Zunger performed comparisons between GaNAs and GaAsP based on first principles linearized augmented plane wave method (LAPW)<sup>149</sup>. Their results indicate that the valence band offset has bowing as well, thus the conduction band bowing is smaller than that based on the dielectric band theory. They also indicated that the dipole matrix element is strongly dependent on composition  $x$  (like bandgap, but stronger) and it is large for small  $x$ <sup>150</sup>. Reduction of the dipole matrix element in small  $x$  means an increase in the electron effective mass calculated from **k-p** perturbation theory<sup>151</sup>,

$$\frac{m_0}{m_e^*} \approx \frac{2}{mE_g} |M_{c,v}|^2$$

where  $M_{c,v}$  is momentum matrix element, which corresponds to the transition probability between states. This equation indicates that smaller bandgaps lead to smaller electron effective mass if  $M_{c,v}$  is constant. For GaNAs,  $M_{c,v}$  is more sensitive to composition than the bandgap. Therefore, increasing nitrogen composition in dilute nitride material leads to an increase in electron effective mass. Bandgap energy of GaNAs used in the calculation is based on LDA ( $c=17\text{eV}$ , bulk) and on EPM (bulk). LDA fits well to experimental values for dilute nitrogen composition ( $x<0.03$ ) and EPM fits well for higher nitrogen composition ( $0.03<x<0.10$ ). Considering two composition regions, the effective mass in the dilute nitrogen region is nearby constant or decreases slightly due to the large bowing but, in the higher nitrogen composition region, the effective mass increases and reaches  $0.1m_0$  at  $x = 0.1$ .

EPM (empirical pseudopotential method) calculations indicate that a fully relaxed, large supercell calculation reproduces well the experimental band gaps of epitaxial GaNP and GaNAs films. Miyoshi and Onabe calculated  $\Gamma-\Gamma$ ,  $\Gamma-X$ , and  $\Gamma-L$  transitions and concluded that the bowing parameter of GaNAs ( $\Gamma-\Gamma$ ) is 4.0 eV from tight binding calculations<sup>152</sup>.

### 5.3.2 Bandgap Calculation of GaInNAs and GaInNAsSb

As discussed above, GaNAs has a large bandgap bowing. Adding indium to GaNAs, creating a quaternary material, GaInNAs, further reduces the bandgap and increases the lattice constant as shown in Figure 1. Tables 8 and 9 list material properties

Binary Material	Lattice constant $a$ (Å)	Bandgap $E_g$ (eV) (cubic)
GaAs	5.6533	1.424
InAs	6.0584	0.324
GaN	4.489	3.2

InN	4.974	1.9
GaSb	6.0959	0.727
InSb	6.4794	0.174

Table 8. Binary material properties.

Ternary alloy material	Bowing parameter $c$ (eV)
GaInN	1 <sup>153</sup>
GaInAs	0.477 <sup>154</sup>
GaNAs	20 <sup>155</sup>
InNAs	4.22 <sup>156</sup>
GaAsSb	1.43 <sup>157</sup>
GaInSb	0.415 <sup>158</sup>
InAsSb	0.67 <sup>159</sup>
InNSb	Unknown
GaNSb	Unknown

Table 9. Bowing parameters for ternary alloy materials

for binary and ternary alloy material to calculate the bandgap and lattice constant of GaInNAs and GaInNAsSb.

Lattice constants of ternary alloys  $A_xB_{1-x}C$  (i.e.  $Ga_xIn_{1-x}As$ ) or  $DE_yF_{1-y}$  (i.e.  $GaN_yAs_{1-y}$ ) can be calculated from Vegard's law as,

$$a_{ABC} = xa_{AC} + (1-x)a_{BC}$$

or,

$$a_{DEF} = ya_{DE} + (1-y)a_{EF}$$

respectively. Therefore, the lattice constant of the quaternary alloy  $Ga_xIn_{1-x}N_yAs_{1-y}$  can be expressed as,

$$a_{GaInNAs} = a_{GaAs}x(1-y) + a_{InAs}(1-x)(1-y) + a_{GaN}xy + a_{InN}(1-x)y$$

and the lattice constant of the quaternary alloy  $Ga_xIn_{1-x}N_yAs_{1-y-z}Sb_z$  can be expressed as,

$$a_{GaInNAsSb} = a_{GaAs}x(1-y-z) + a_{InAs}(1-x)(1-y-z) + a_{GaIn}xy + a_{InN}(1-x)y + a_{GaSb}xz + a_{InSb}(1-x)z$$

In the case for  $Ga_xIn_{1-x}N_yAs_{1-y}$  to be lattice-matched to GaAs substrate, the relation between composition  $x$  and  $y$  is expressed as,

The bandgap energy for ternary alloys  $A_xB_{1-x}C$  or  $DE_yF_{1-y}$  can be calculated by considering the parabolic term (bowing parameter  $c \neq 0$ )

$$E_{gABC} = E_{gAC}x + E_{gBC}(1-x) - c_{ABC}x(1-x)$$

$$E_{gDEF} = E_{gDE}y + E_{gDF}(1-y) - c_{DEF}y(1-y)$$

or, respectively, thus, the bandgap energy of the quaternary alloy  $Ga_xIn_{1-x}N_yAs_{1-y}$  can be expressed as,

$$E_{gGaInNAs} = E_{gGaIn}xy + E_{gInN}(1-x)y + E_{gGaAs}x(1-y) + E_{gInAs}(1-x)(1-y) - x(1-x)[c_{GaInN}y + c_{GaInAs}(1-y)] - y(1-y)[c_{GaAs}x + c_{InAs}(1-x)]$$

and the bandgap energy of quaternary alloy  $Ga_xIn_{1-x}N_yAs_{1-y-z}Sb_z$  can be expressed as,

$$E_{gGaInNAsSb} = E_{gGaIn}xy + E_{gInN}(1-x)y + E_{gGaAs}x(1-y-z) + E_{gInAs}(1-x)(1-y-z) + E_{gGaSb}xz + E_{gInSb}(1-x)z - x(1-x)[c_{GaInN}y + c_{GaInAs}(1-y-z) + c_{GaInSb}z] - y(1-y-z)[c_{GaAs}x + c_{InAs}(1-x)] - yz[c_{GaNSb}x + c_{InNSb}(1-x)] - z(1-y-z)[c_{GaAsSb}x + c_{InAsSb}(1-x)]$$

The above equations are useful for determining the bulk (unstrained) GaInNAs and GaInNAsSb bandgaps. From calculations using above equations, GaInNAs and GaInNAsSb can be grown while remaining lattice matched to GaAs with bandgaps in the 1.3-1.55  $\mu\text{m}$  wavelength range.

The band lineup between GaInNAs and GaAs is shown in Figure 67. GaInAs/GaAs band lineups have been well investigated and the relation between conduction and valence band offset with GaAs is  $\Delta E_c : \Delta E_v = 3 : 2$ <sup>47</sup>. Band offsets between GaNAs and GaAs were calculated by Sakai *et. al.* with dielectric band theory and the result shows bowing parameter of GaNAs is negligible and is almost proportional to its nitrogen composition<sup>51</sup>. Ding *et. al.* directly measured the valence band offset between GaN and GaAs of 1.84 eV by XPS<sup>160</sup>. By combining the theoretical prediction and the experimental result, valence band offset between GaN<sub>y</sub>As<sub>1-y</sub> and GaAs can be expressed as,

$$\Delta E_v = \Delta 1.84\text{eV} \cdot y. \quad (0 \leq y \leq 1)$$

Experimental measurements of valence band offset between GaNAs/GaAs by Kitatani *et. al.* also supports the above equation<sup>56</sup>. From this analysis of valence band offsets, the conduction band offset of GaNAs is supposed to have as large a bowing parameter as that of the bandgap. This is a very important property of GaInNAs because a large conduction band offset increases the characteristic temperature of the laser as mentioned in chapter 5.2. Figure 67 depicts the band lineup of GaInNAs on GaAs as a function of strain. The direction left of zero means tensile strain and to the right means compressive strain. The origin is the valence band maximum point of GaAs.

Adding indium into GaAs increases the compressive strain and pushes the conduction band down and the valence band up. Adding nitrogen to GaAs increases tensile strain, depressing both the conduction band and valence band. The slope of the conduction band is larger than that of the valence band, yielding a net decrease with nitrogen content. Now, if nitrogen is added into GaInAs to form GaInNAs, the conduction band energy of GaInAs shifts to B as the same amount shift as A (GaAs – GaNAs) under the assumption that the bowing parameter of GaInNAs is the same as that

of GaNAs. The valence band of GaInAs shifts to E<sub>v</sub> as the amount of GaNAs increases. The conduction band of GaNAs shifts to E<sub>c</sub> as the shift C (GaAs - GaNAs). This results the

#### 5.4 Fabrication and Characterization

##### Laser

30nm GaAs waveguide  
 Separate confinement layer  
 7nm quantum well  
 20nm barrier  
 GaInNAs or GaInNAsSb quantum well  
 epitaxy. Compared to conventional GaAs, the incorporation of nitrogen in the GaInNAs and GaInNAsSb quantum well layers with

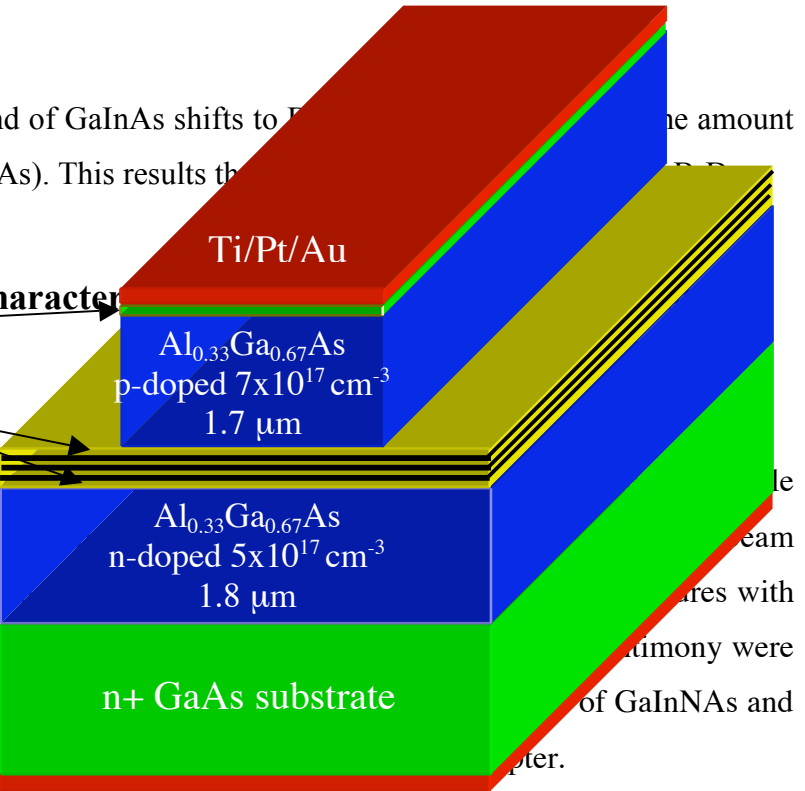


Figure 68. Ridge waveguide laser structure

##### 5.4.1. Laser Structure Growth

The laser diodes for this work were grown by solid source MBE (Varian Mod Gen II system) with a rf nitrogen plasma source. The details of the growth were introduced in chapter 2.

The ridge waveguide laser structure is shown in Figure 68. The structures are always deposited upon a 3000 Å GaAs buffer layer with  $2 \times 10^{18} \text{ cm}^{-3}$  silicon doping to smooth out the surface. Two different growth techniques were utilized for growing the bottom and top cladding layers. Since the nitrogen concentration is decided by the group III growth rate (chapter 2.6.1), once the nitrogen concentration is fixed, the growth rate (or the flux) of both indium and gallium cannot be changed. Therefore, if both of the cladding layers are intended to be grown in the same system and sources as the active layer, those layers will be grown at the growth rate fixed by the desired nitrogen concentration, which is typically 0.3 μm/hour for gallium and 0.15 μm/hour for aluminum to get an  $\text{Al}_{0.33}\text{Ga}_{0.67}\text{As}$  alloy. Since the bottom cladding layer thickness is 1.8 μm and top cladding layer thickness is 1.7 μm, the growth time for only the cladding

Layer	Doping Type	Doping level (cm <sup>-3</sup> )	Layer thickness (μm)
Substrate	N	2×10 <sup>18</sup>	~500
GaAs buffer layer	N	1×10 <sup>19</sup>	0.3
AlGaAs bottom cladding layer	N	5×10 <sup>17</sup>	1.8
Active layer	None	None	~0.35
AlGaAs top cladding layer	P	7×10 <sup>17</sup>	1.7
GaAs capping layer	P	1×10 <sup>19</sup>	0.05

*Table 10. Growth structure of ridge waveguide emitting lasers*

layers is around 8 hours. To avoid this long growth, “wafer-transfer” in the transition tube was adopted. Since we have two sister machines connected by an UHV transition tube ( $\sim 10^{-10}$  Torr), we can grow a sample in one machine and transfer it to the other machine without contamination of the grown sample. In this configuration, the growth rate in the other machine for the cladding layers can be set independently of the nitrogen concentration (i.e. gallium growth rate: 0.67 μm, aluminum growth rate: 0.33 μm) and this shortens growth time. This technique also has the advantage of getting accurate fluxes from each source, especially from the antimony source. If the whole structure is grown in one machine, there is a long interval difference between the flux measurement and actual growth for some sources, like indium and antimony. However, if the growth is done in two machines, the fluxes from these sources can be taken right before the active layer growth, which reduces flux error.

The total thickness of the active layer was designed to produce strong optical confinement, which is set at  $\lambda/n$  for this work. Here  $n$  is effective refractive index of the active layer and, since the thickness of the quantum well and barrier is relatively small and not much different from GaAs, the refractive index of GaAs was used ( $n=3.65$ ,  $\lambda/n \approx 3500$  Å at 1.3 μm). For the three quantum well structure,

1. GaAs bottom and top waveguide layer:  $1200 \text{ Å} \times 2 = 2400 \text{ Å}$
2. Quantum well:  $70 \text{ Å} \times 3 = 210 \text{ Å}$

3. Barrier:  $200 \text{ \AA} \times 4 = 800 \text{ \AA}$
4. Total thickness =  $3410 \text{ \AA}$

The rf power and nitrogen flow rate were set to 300 W and 0.5 sccm, respectively and the reflected power was kept at a minimum (around 6 W) with a rf matching network. The exact procedure for plasma source operation was discussed in chapter 2.2.3. The plasma source was ignited 10 minutes prior to growth of the first barrier layer to reduce unwanted nitrogen background and plasma-related ion damage, which increases non-radiative recombination especially in AlGaAs. For  $0.3 \text{ \mu m/hour}$  gallium growth rate, the layer thickness with nitrogen-plasma-blocked by shutter is  $500 \text{ \AA}$ . As shown in Figure 20, the nitrogen background concentration with the shutter-closed is approximately 1 % of the value with the shutter open. To minimize this unwanted background nitrogen concentration, one of the following methods can be chosen: a separate gate valve is used for the nitrogen plasma source or instant ignition of the plasma right before layer growth is used, which requires an extremely stable plasma source. The plasma source was turned off right after the last GaInNAs quantum well or GaNAs barrier again to reduce unwanted background nitrogen.

The growth temperature was checked by monitoring the GaAs surface deoxidation temperature. The deoxidation temperature under arsenic over pressure on GaAs was  $600^\circ\text{C}$  and the offset between this temperature and the thermocouple temperature was taken into account for figure out the real temperature from the thermocouple temperature. The buffer and cladding layers were grown at  $600^\circ\text{C}$  to produce high quality material. For the active layer, the first  $900 \text{ \AA}$ , out of  $1200 \text{ \AA}$  were grown at  $600^\circ\text{C}$ . To prevent indium desorption and phase segregation caused by nitrogen, the growth temperature for the GaInNAs quantum wells and GaNAs barriers was set at  $400^\circ\text{C}$ . During the final  $300 \text{ \AA}$  of the GaAs waveguide, the substrate temperature was ramped down from  $600^\circ\text{C}$  to  $400^\circ\text{C}$ . This low temperature growth is necessary for dilute nitride alloy growth but this can cause large number of non-radiative point defects ( $1 \times 10^{20} \text{ cm}^{-3}$ ) including arsenic antisites<sup>161</sup>. This high defect concentration contributes to the high threshold current, low radiative efficiency, and low output power. These defects caused by low growth

temperature can be restored by high temperature annealing; as can crystal defects caused by the plasma source, as discussed in chapter 3.

Substrate rotation of 12 rpm for bulk layer growth and 15 rotation per minute for quantum well layers are used to improve film uniformity across the substrate.

#### 5.4.2 Laser Structure Fabrication

The optimal annealing conditions for photoluminescence samples to achieve the highest photoluminescence intensity and smallest FWHM are between in 760 - 820°C for 1~3 minutes, as explained in chapter 3.1. However, for the laser structure, high temperature growth (600°C) of the top cladding layer growth for 2~4 hours provides *in-situ* annealing and changes the optimum post-growth annealing conditions. Our experiments show that the optimum post growth annealing temperature for laser samples is approximately 60°C below that of the photoluminescence samples. Laser diodes were annealed at the optimum temperature according to this offset. Laser diodes were annealed under a GaAs proximity cap to prevent arsenic desorption under continuous nitrogen flow.

Ridge waveguides were patterned by photolithography using a lift-off process followed by reactive ion etching (RIE) down to the GaAs waveguide layer. To prevent rough side wall formation due to metal lift-off process, a special chemical, LOL-2000,

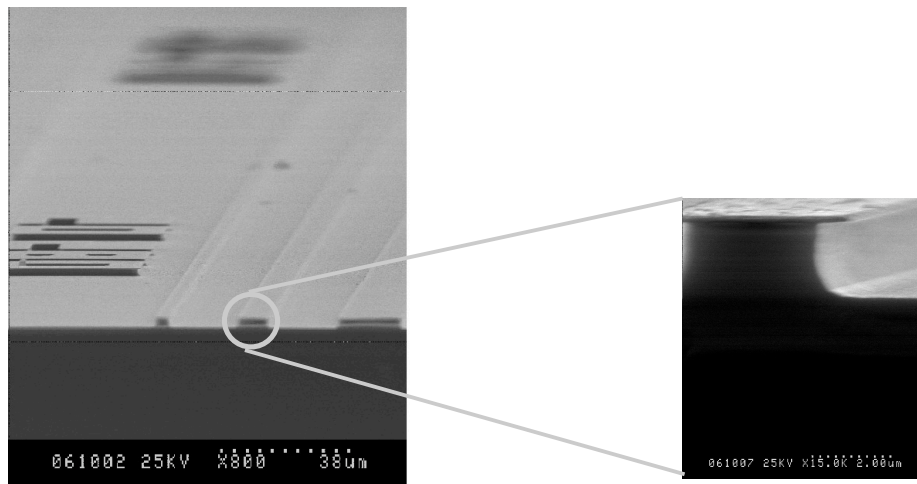


Figure 69. SEM images of a ridge waveguide structure. The size of mesas are 5, 10, 20  $\mu\text{m}$  from left to right.

was used to have undercut beneath the photoresist (SPR-3612), which prohibits the evaporated metal from sticking on the side of the patterned photoresist. Following this patterning, p-contact layers were evaporated with Ti/Pt/Au: 200Å/400Å/4000Å. A titanium layer is used for smoothing the surface and provides a eutectic layer on GaAs. Since gold gets soft at high temperature (during contact annealing), it penetrates into the semiconductor, and spikes through the *p-n* junction (which is often a cause of device failure). A harder material than gold, platinum, was used between Ti and Au. Finally, a thick gold layer was deposited to accommodate the physical impact of the probe tip and provide better electric distribution across the device. To form a waveguide, dry-etching is done and masked by the self-aligned p-contact. Wet etching was utilized following the RIE etch to remove sidewall damages and roughness and reduce optical scattering losses. A SEM micrograph of a ridge waveguide structure is shown in Figure 69. As shown in the magnified image, the typical side wall roughness is removed by wet etching. Following the top p-side processing, the substrate was lapped and polished down to 100 μm for better thermal conduction and manual cleaving convenience. The thinned surface was coated with a n-contact alloy (Ni/Ge/Au/Ge/Au: 80Å/100Å/120Å/100Å/2000Å) and annealed with a two stage annealing process. The first stage was 360°C for 30 seconds to make Ni wet to the GaAs surface. Then the temperature was set to 430°C for 1 minute to alloy the contact. This process mixes the complicated alloy and provides a low contact resistance. High contact resistance causes undesired voltage drops across metal and semiconductor junctions which causes Joule heating and device degradation.

The ridge waveguide laser diodes have stripe widths of 5, 10, and 20 μm and lengths ranging from 400 μm to 1500 μm. After cleaving, the devices were mounted on a variable temperature copper block for both room temperature and temperature-varying measurements. No conductive epoxy or active cooling was used during device measurements. Light output was measured using a calibrated broad area GaInAs photodiode with an integrating sphere and spectral data was obtained by coupling into a graded-index lensed multimode fiber connected to an optical spectrum analyzer (OSA).

## 5.5 Laser Results

### 5.5.1 1.3 $\mu\text{m}$ GaInNAs/GaNAs Lasers

Based on the photoluminescence results in Chapter 3, the first laser described in this thesis contained three  $\text{Ga}_{0.68}\text{In}_{0.32}\text{N}_{0.015}\text{As}_{0.985}$  quantum wells with  $\text{GaAs}_{0.98}\text{N}_{0.02}$  barriers. Figure 70 shows the optical spectrum of this laser with an emission peak at 1.315  $\mu\text{m}$  at  $I=1.2I_{th}$ . This laser was one of the few lasers with emission beyond 1.3  $\mu\text{m}$  when it was measured. Light output power (L) vs. injection current (I) vs. voltage across device (V) are shown in Figure 71. The turn-on voltage was less than 1 V, which demonstrates that very low contact resistance and excellent diode characteristics are possible with proper doping and device design. One of the important parameters that determines the quality of the laser is the threshold current density. Threshold current can be found as<sup>162</sup>,

$$I_{th} = WL \frac{N_w J_{tr}}{\Gamma} \exp \left[ \frac{1}{2L} \ln \left( \frac{1}{R_f R_r} \right) \right] + I_1 L + I_2$$

**Optical Spectrum**

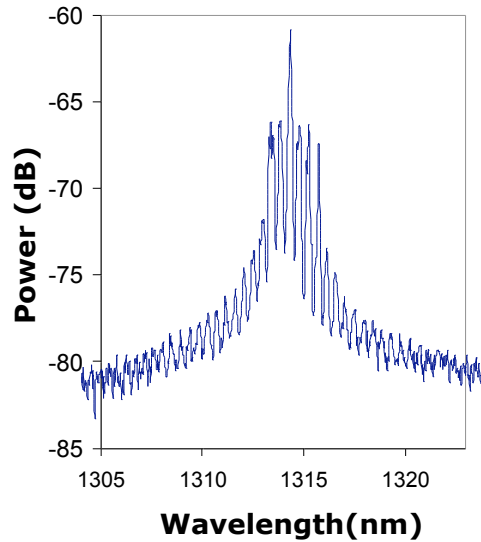


Figure 70. Optical spectrum of  $\text{Ga}_{0.68}\text{In}_{0.32}\text{N}_{0.015}\text{As}_{0.985}/\text{GaAs}_{0.98}\text{N}_{0.02}$  laser.

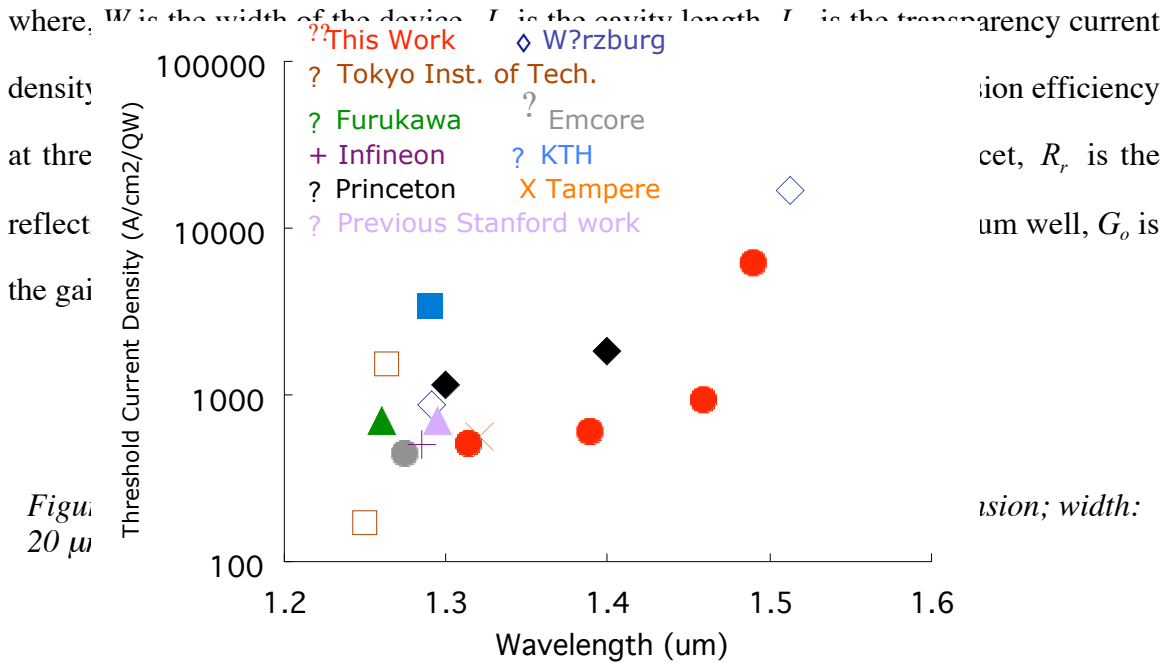


Figure 72. Comparison chart on threshold current density vs. emission wavelength between this work and those from other research groups.

Unlike GaInAs or GaAs quantum well lasers, GaInNAs lasers suffer from high threshold current density due to a high concentration of non-radiative recombination defects. Figure 72 shows the comparison chart of threshold current density vs. emission wavelength between this work and those from other research groups. As shown, the threshold current density increases as the emission wavelength reaches 1.3 μm. This is because increasing nitrogen needs to be incorporated to get longer wavelength laser emission and this higher nitrogen concentration causes phase segregation along with more non-radiative defects. The threshold current density of this work at 1.3 μm is 1.5 KA/cm<sup>2</sup> for the laser with three quantum well (500 A/cm<sup>2</sup> per quantum well) and this is one of the lowest threshold current densities reported for GaInNAs quantum well lasers.

Figure 73 shows the cavity length dependent inverse differential quantum efficiency,  $\eta_d^{-1}$ . Internal quantum efficiency  $\eta_i$ , internal loss  $\alpha_i$ , and transparency current density  $J_{tr}$  can be calculated from experimental data. The differential quantum efficiency (DQE),  $\eta_d$ , can be expressed as,

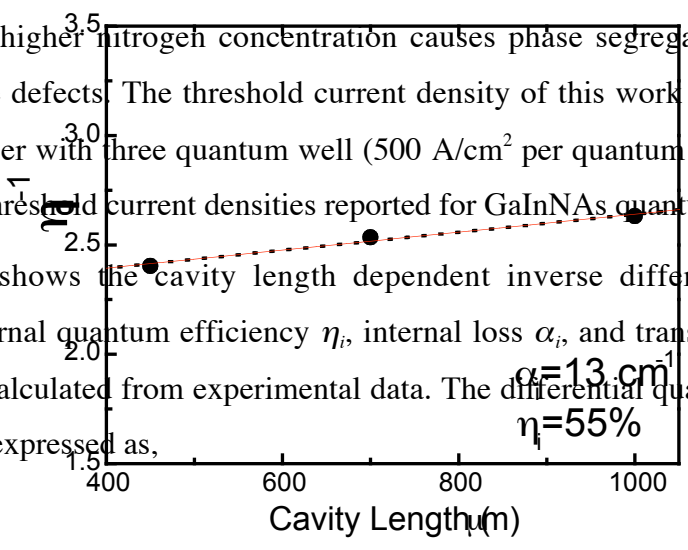


Figure 73. Cavity length dependent inverse differential quantum efficiency of  $Ga_{0.68}In_{0.32}N_{0.015}As_{0.985}/GaAs_{0.98}N_{0.02}$  laser.

$$\frac{1}{\eta_d} = \frac{\langle \eta_i \rangle}{\eta_i \ln(1/R)} L + \frac{1}{\eta_i}$$

and  $\eta_d$  can be estimated from the slope of I-L curve above threshold by,

$$\eta_d = \frac{q}{h\nu} \frac{dP_o}{dI}, \quad I > I_{th}$$

differential quantum efficiency,  $\eta_d$ , can be given in units of A/W or % under the relationship of,

$$\eta_d[\%] = \eta_d[A/W] / h\nu$$

here  $\eta_d$  of 48% (0.45 A/W) is obtained from Figure 72. An uncoated GaAs facet has  $R$  of 0.32, giving  $\eta_i = 13$ ,  $\eta_i = 55\%$ . Gain can be found from the relation,

$$g = G_o \ln \left( \frac{\eta_i \cdot J}{J_{tr}} \right)$$

where  $G_o$  is gain constant. At threshold, loss and gain are equal,  $\alpha \cdot g = a$ , ( $a = a_i + a_m$ ), thus the threshold current density can be expressed as,

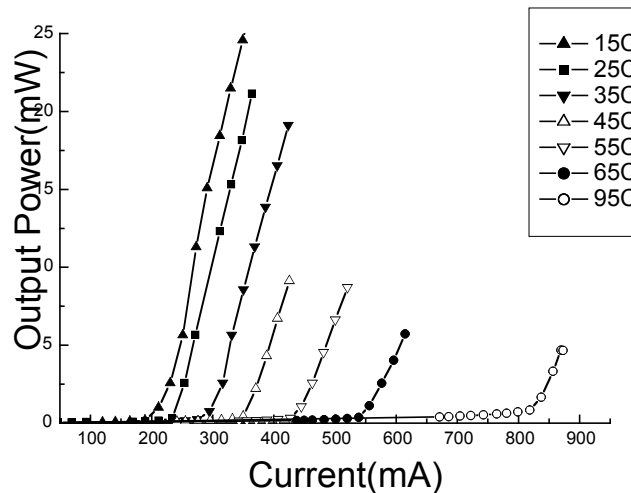


Figure 74. Temperature dependent device operation of  $1.31 \mu\text{m Ga}_{0.68}\text{In}_{0.32}\text{N}_{0.015}\text{As}_{0.985}/\text{GaAs}_{0.98}\text{N}_{0.02}$ , Device width:  $20 \mu\text{m}$ , length:  $600 \mu\text{m}$ .

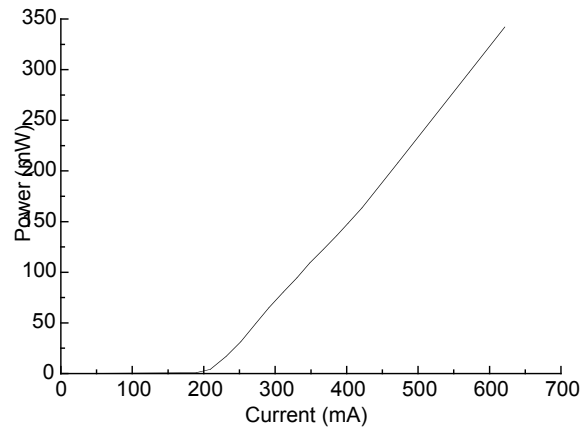


Figure 75. Maximum power of 350 mW from  $Ga_{0.68}In_{0.32}N_{0.015}As_{0.985}/GaAs_{0.98}N_{0.02}$  laser.

$$J_{th} = \frac{J_{tr}}{\Gamma_i} \exp\left(\frac{a}{G_o \cdot \Gamma_i}\right)$$

where the optical confinement factor,  $\Gamma_i$ , is assumed to be 0.04, device length,  $L$ , is measured to be 600  $\mu\text{m}$ , and  $J_{th}$  is measured to be 1.6  $\text{kA}/\text{cm}^2$  for the edge emitting laser. By solving the above equation,  $G_o=1627 \text{ cm}^{-1}$  and  $J_{tr}=205 \text{ A}/\text{cm}^2$  were obtained.

Devices were tested under pulsed conditions at different operating temperatures to characterize the temperature dependent device operation. Figure 74 shows the pulsed operation for different stage temperatures. This device operates up to 95°C.

The maximum pulsed output power from both facets, without a heat sink or

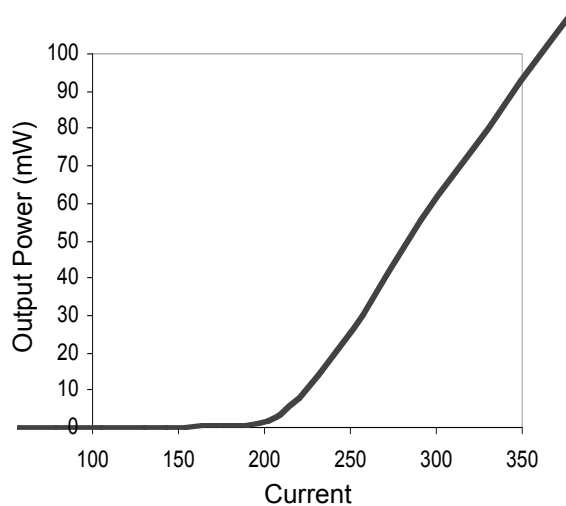


Figure 76. L-I for the laser diode with  $Ga_{0.65}In_{0.35}N_{0.017}As_{0.0983}/GaAs_{0.978}N_{0.022}$ . Device width: 20  $\mu\text{m}$ , length: 560  $\mu\text{m}$ .

AR/HR coating, was 350 mW as shown in Figure 75. This maximum power was reproducible without device failure (1  $\mu$ s period with 1% duty cycle).

A laser with higher indium (35%) and nitrogen (1.7%) compositions was grown to demonstrate emission beyond 1.3  $\mu$ m. The L-I curve for this device, with three  $\text{Ga}_{0.65}\text{In}_{0.35}\text{N}_{0.017}\text{As}_{0.0983}$  quantum wells and  $\text{GaAs}_{0.978}\text{N}_{0.022}$  barriers, is shown in Figure 76. This in-plane laser showed room temperature emission at 1.39  $\mu$ m as shown in Figure 77.

The threshold current density was 1.8 kA/cm<sup>2</sup>, which is 600 A/cm<sup>2</sup> per quantum well. The slope efficiency from both facets was 0.67 W/A (74.6%) above threshold current. The maximum output power under pulsed conditions was 320 mW from both facets without a heat sink or AR/HR coating. Again, the maximum output power was repeatable without device failure. The maximum operating temperature was 70°C without a heat sink. The epitaxial layer design and device geometries were not optimized for high power device application. Thus, with proper modification, higher output power can be achieved. Figure 78 shows the optical spectrum of the device operating at 1.4  $\mu$ m, which is the longest wavelength we have observed to date from our GaInNAs/GaNAs laser diodes.

Due to the lattice mismatch between GaAs and InAs, indium incorporation over 40% is not easily achieved with MBE, as explained in Chapter 5.2. While a higher nitrogen concentration compensates for the lattice mismatch, thus allowing increased

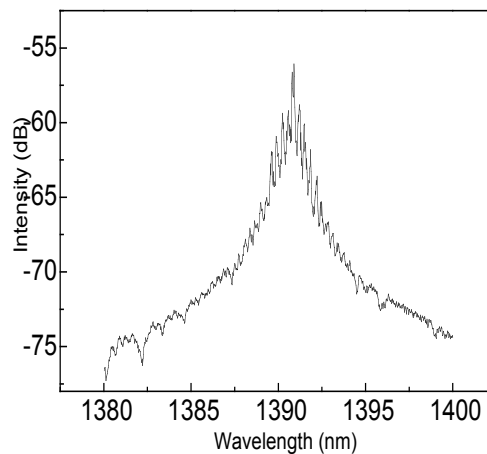


Figure 77. Emission spectrum of  $\text{Ga}_{0.65}\text{In}_{0.35}\text{N}_{0.017}\text{As}_{0.0983}/\text{GaAs}_{0.978}\text{N}_{0.022}$  at 1.39  $\mu$ m.

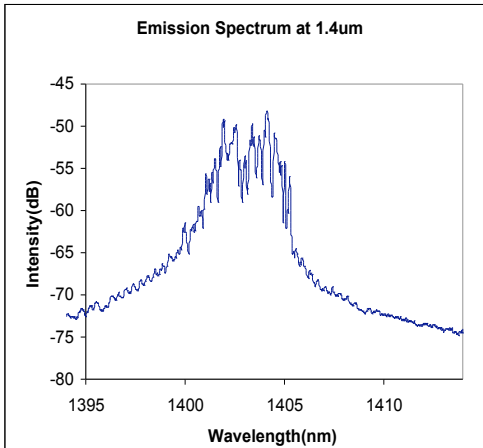


Figure 78. Laser emission at 1.4  $\mu\text{m}$  at room temperature.

indium incorporation, it dramatically degrades the device performance as shown in Figure 72. Thus, to push the wavelength past 1.4  $\mu\text{m}$ , while maintaining low threshold current, it is desirable to increase indium and decrease the nitrogen compositions. The problem with high indium compositions is that the growth goes from planar 2D to rough 3D growth with the formation of “quantum dots.” Some work was reported on utilization of antimony as a surfactant to prevent the onset of 3D growth and extend the emission wavelength of GaInNAs<sup>163,164,165</sup>. However, all of this work showed either shorter wavelength<sup>164</sup> or insufficient material quality for optoelectronic device application<sup>163,165</sup>. As presented in Chapter 4, our work shows that the material quality of GaInNAsSb can be competitive with, or even better than GaInNAs without antimony but with much longer emission, out to 1.6  $\mu\text{m}$ . Additionally, for our case, antimony is not only working as a surface surfactant, but as one of the group V constituents. This was shown by secondary ion mass spectroscopy in Chapter 4. This result can be supported by the fact that GaSb and InSb have smaller bandgap energies than GaAs and InAs and having Sb as a constituent further reduces bandgap. This indicates that longer wavelength emission is possible with Sb incorporation into the quantum wells. However, a clear explanation of how the larger GaSb or InSb molecules can be incorporated into the already highly strained GaInNAs quantum wells is not yet known. Nonetheless, knowing that Sb can be utilized as a surfactant, we introduced it during the active layer growth and were able to incorporate up to 42% indium without 3D growth or relaxation of the epitaxial film.

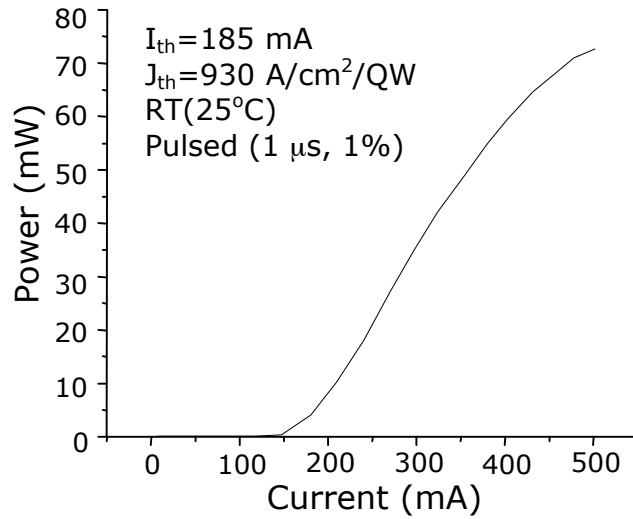


Figure 79. L-I curve of a 1.4  $\mu\text{m}$  GaInNAsSb/GaNAsSb ridge waveguide laser with maximum output power exceeding 70 mW. The indium concentration is 36% and antimony pressure was  $6.86 \times 10^{-8}$  Torr.

However, the sample with greater than 42% indium composition shows a noticeable degradation in epitaxial film quality and two orders of magnitude lower photoluminescence intensity as shown in Figure 47.

A ridge waveguide laser was grown under the conditions of 36% indium concentration and antimony pressure of  $6.86 \times 10^{-8}$  Torr based on the photoluminescence results in Chapter 4.1. This sample was grown with three GaInNAsSb quantum wells and GaNAsSb barriers. Figure 79 shows the light output power as a function of injection

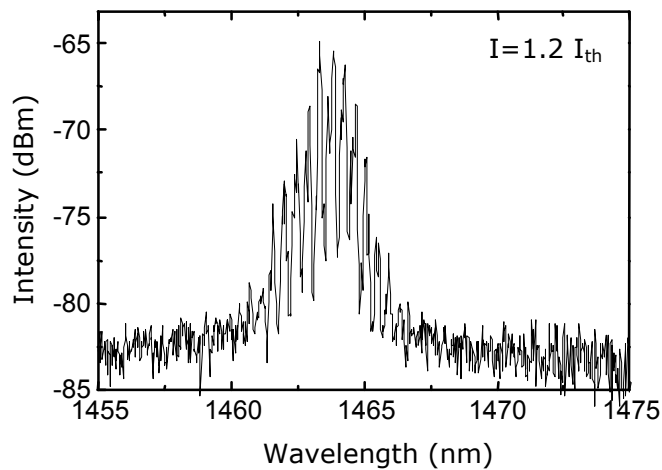
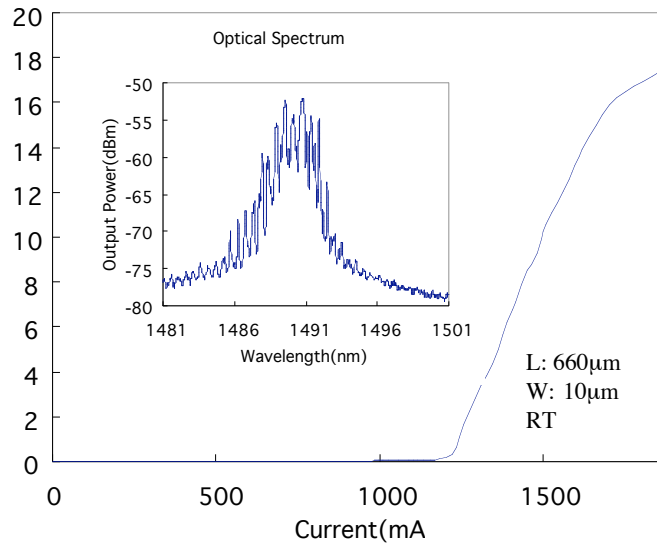


Figure 80. Optical spectrum of a GaInNAsSb/GaNAsSb ridge waveguide laser with peak emission at 1.465  $\mu\text{m}$ . The indium concentration is 36% and antimony pressure is  $6.86 \times 10^{-8}$  Torr.



*Figure 81. L-I curve and optical spectrum for a GaInNAsSb/GaNAsSb ridge waveguide laser with peak emission at 1.49 μm. The indium mole fraction is 38% and antimony flux was  $1.4 \times 10^{-7}$  Torr.*

current. This laser operated at room temperature with maximum output power exceeding 70 mW from a 5 μm wide stripe. As shown in Figure 80, the laser diode exhibited emission at 1.465 μm. The minimum threshold current density was 2.8 kA/cm<sup>2</sup>, which is 930 A/cm<sup>2</sup> per quantum well. To the best of our knowledge, this is the lowest threshold current density for lasers beyond 1.4 μm grown on a GaAs substrate. Another laser sample was grown with 38% indium composition and Sb pressure of  $1.4 \times 10^{-8}$  Torr. As shown in Figure 80, the laser diode showed room temperature operation and emission at 1.49 μm. The device performance was degraded compared to the previous one at 1.46 μm and the devices had shorter wavelength emission than that of the photoluminescence samples grown under the same conditions. This might be due to the un-valved Sb source used for this growth resulting in Sb flux variation over the course of the growth. A second reason may be due to an unstable indium cell, which suffered flux fluctuations over time. This unstable indium pressure fluctuation made it very difficult to predict accurate compositions and could have shifted the wavelength to shorter wavelengths.

## CHAPTER 6: Conclusion and Future Improvement

This work was intended to develop a high quality, reliable, temperature insensitive, inexpensive material for optical communication lasers at 1.3 ~ 1.6  $\mu\text{m}$  on a GaAs substrate. The possible device application with this new material, GaInNAs and GaInNAsSb, could be Fabry-Perot lasers, ridge-waveguide lasers, distributed feedback (DFB) lasers, vertical cavity surface emitting lasers (VCSELs), electro-absorption modulators, photodetectors, solar cells, etc. Being based on mechanically strong, inexpensive, highly thermally conductive and well-developed GaAs substrate, the advantages of this new material shine even more brightly.

The purpose of this work was focused on investigation of the material properties of GaInNAs and GaInNAsSb, finding optimum growth conditions and parameters, exploiting new structures using nitrogen and antimony in the barriers, realizing laser structures with these new materials, and improving laser performance.

This work investigated the characteristics of a nitrogen rf plasma source and optimized the conditions of this source for stable operation, maximum atomic N flux, and maximal optical quality material. The rf plasma conditions were rf power of 300 W, reflected power of 6 W, and nitrogen flow of 0.25 ~ 0.5 sccm. Measurements were done to correlate the nitrogen concentration to growth parameters. MBE growth conditions were optimized to provide high quality material with long wavelength beyond 1.3  $\mu\text{m}$ . The growth conditions included group III growth rate, substrate temperature, arsenic over-pressure, and antimony pressure.

Extensive annealing studies were performed to understand the effects of thermal annealing on dilute nitride materials. The photoluminescence intensity increased 100 times after proper annealing, though the photoluminescence blue-shifts around 50 meV. The causes of this PL shift were found to be nitrogen out-diffusion and nitrogen nearest atom rearrangement.

Many measurement techniques were utilized to characterize this material, including, photoluminescence, X-ray diffraction, cathodoluminescence, atomic force

microscopy, and secondary ion mass spectrometry. These measurements provided a better understanding of this new material and guided the improvement of material quality. These materials grown under optimum conditions proved to be of high quality by these measurements. Also, the fundamentals of these measurements were briefly described in Chapter 4.

The laser growth and fabrication was discussed in Chapter 5. The growth conditions and fabrication steps were detailed. The lasers from this work showed excellent characteristics including wide wavelength coverage, high efficiency, high operation temperature, low threshold current density and high output power.

In the future, there are several issues that could possibly improve the quality and extend the emission wavelength of this new material. These are following,

1. Finding a way to keep the emission wavelength beyond 1.3  $\mu\text{m}$  without using a GaNAs barrier. GaAs barriers have a higher conduction band offset and unnecessary non-radiative recombination centers from nitrogen in the barriers can be avoided. This will require fine tuning of growth conditions since more indium incorporation is needed to achieve long emission without GaNAs. GaInNAsSb will be a good candidate.
2. Installation of a gate-valve for the plasma source. Isolating the nitrogen source from the growth chamber during non-dilute nitrogen material growth will remove the unwanted nitrogen background, which is the main culprit for non-radiative recombination centers and reduced injection efficiency of the laser.
3. Installation of a valved antimony cracker. The precise control of antimony pressure can be achieved with a valved cracker. Since antimony is the key element in this new material and the optical quality is very sensitive to the antimony pressure, the ability to control the antimony pressure will greatly contribute to the quality of the material.
4. Exploiting antimony cell conditions. This will include various pressure points and cracking temperatures for different cracking efficiency dependent on growth conditions.

5. Further optimization of indium, nitrogen, and antimony concentrations. Fine tuning of these parameters will provide higher quality material.
6. Optimizing the substrate temperature dependence of the growth conditions. No extensive study has been done on the optimum growth temperature and finding the right temperature will be great help to achieve high quality material.

## BIBLIOGRAPHY

- 
- <sup>1</sup> Phillips, A. F., Sweeney, S. J., Adams, A.R., and Thijs, P. J. A., "The temperature dependence of 1.3 and 1.55  $\mu\text{m}$  compressively strained GaInAs(P) Multiple quantum well semiconductor lasers," *IEEE J. Select. Topics Quantum Electron.*, vol. 5, pp. 301-352, 1999.
- <sup>2</sup> C. W. Coldren, M. C. Larson, S. G. Spruytte and J.S. Harris Jr., "1200 nm GaAs based vertical cavity lasers employing GaInNAs multiple quantum well active region," *Electron. Lett.* Vol. 36, no 11, pp. 951-952, May 25, 2000.
- <sup>3</sup> J. S. Harris Jr., "Tunable long-wavelength vertical-cavity lasers: the engine of next generation optical networks?" *IEEE J. Select. Topics Quantum Electron.*, vol. 6, pp. 1145-1160, Nov.-Dec. 2000.
- <sup>4</sup> W. Ha, V. Gambin, M. Wistey, S. Bank, H. Yuen, S. Kim, J. Harris, "Long Wavelength GaInNAsSb/GaNAsSb Multiple Quantum Well Lasers," *Elect. Lett.* Vol. 38, no. 6, pp. 277-278, Mar.2002.
- <sup>5</sup> W. Ha, V. Gambin, M. Wistey, S. Bank, S. Kim, J. Harris, "Multiple Quantum Well GaInNAs/GaNAs Ridge-Waveguide Laser Diodes Operating out to 1.4  $\mu\text{m}$ ", *Photon. Tech. Lett.* vol. 14, no. 5, May 2002.
- <sup>6</sup> W. Ha, V. Gambin, M. Wistey, S. Bank, H. Yuen, S. Kim, J. Harris, *Jour. Of Quant. Elect.*, vol. 38, no. 9, p. 1260-1267, Sep. 2002.
- <sup>7</sup> S. Sato, Y. Osawa, T. Saitoh, and I. Fujimura, "Room-temperature pulsed operation of 1.3  $\mu\text{m}$  GaInNAs/GaAs laser diode," *Electro. Lett.*, vol. 33, no. 16, pp. 1386-1387, July 1997.
- <sup>8</sup> Gokhale, M.R., Studentkov, P.V., Wei J., and Forrest, S. R., "Low threshold current, high efficiency 1.3  $\mu\text{m}$  wavelength aluminum-free GaInNAs-based quantum-well lasers," *IEEE Photonics Tech. Lett.*, vol. 12, pp. 131-133, 2000.
- <sup>9</sup> T. Kitatani, K. Nakahara, M. Kondow, K. Uomi, T. Tanaka, "Mechanism analysis of improved GaInNAs optical properties through thermal annealing," *J. of Crystal Growth*, 209, 345-349, 2000.
- <sup>10</sup> L. A. Coldren and S. W. Corzine, "Diode lasers and photonic integrated circuits", John Wiley & Sons Inc., 1998.
- <sup>11</sup> Reprinted from [www.iec.org](http://www.iec.org)
- <sup>12</sup> S. Kawanishi, H. Takara, K. Uchiyama, I. Shake, K. Mori, *Electron. Lett.* vol. 35, pp. 826, 1999.
- <sup>13</sup> M. N. Islam, *Physics Today*, p. 34, May, 1994.

- 
- <sup>14</sup> B. Pezeshki, "Optimization of reflection electro-absorption modulators", Ph.D. thesis, Stanford university, 1991.
- <sup>15</sup> K. I. Kang, T. G. Chang, I. Glesk, P. R. Prucnal, *Appl. Opt.* vol. 35, p.417, 1996.
- <sup>16</sup> R. H. Coase, "The Firm, the market, and the Law," Reprint ed., Chicago: university of Chicago Press, 1988.
- <sup>17</sup> U. J. Heuser, "*Das schnelle Leben*," 1st ed., Berlin: Berlin Veriag, 2000.
- <sup>18</sup> F. P. Kapron, D. B. Keck, and R. D. Maurer, "Radiation losses in glass optical waveguides," *Appl. Phys. Lett.*, vol. 17, pp. 423-425, 1970.
- <sup>19</sup> K. Sagara, *OPTRONICS*, No. 8, pp. 108-112, 2000
- <sup>20</sup> J. Harris, "GaInNAs: A New Material for Long Wavelength Lasers", *IEEE LEOS Summer Topicals Meeting*, Copper Mountain, CO, Aug. 2000.
- <sup>21</sup> H. Soda, K. Iga, C. Kitahara and Y. Suematsu, "GaInAsP/InP Surface Emitting Injection Lasers", *Jpn. J. Appl. Phys.* Vol. 18, pp 2329-2330, 1979.
- <sup>22</sup> I. Ibaraki, S. Ishikawa, S. Ohkouchi and K. Iga, *Elec. Letts.* Vol. 20, pp 420, 1984.
- <sup>23</sup> S. A. Chailertvanitkul, K. Iga, K. Moriki, "GaInAsP/InP surface emitting laser ( $\lambda=1.4 \mu\text{m}$ , 77K) with heteromultilayer Bragg reflector," *Electron. Lett.*, Vol. 21, pp. 303-304, 1985.
- <sup>24</sup> P. L. Gourley and T. J. Drummond, "Single crystal, epitaxial multi-layers of AlAs, GaAs, and  $\text{Al}_x\text{Ga}_{1-x}\text{As}$  for use as optical interferometric elements," *Appl. Phys. Lett.*, vol. 49, pp. 489-491, 1986.
- <sup>25</sup> S. Kinoshita, T. Kobayashi, T. Sakaguchi, T. Odagawa, and K. Iga, "Room temperature pulse operation of GaAs surface emitting laser by using  $\text{TiO}_2/\text{SiO}_2$  dielectric multilayer reflector," *Trans. IEICE. Jpn.*, vol. J69-C, pp. 412-420, 1986.
- <sup>26</sup> P. L. Gourley and T. J. Drummond, "Visible room temperature surface emitting laser using an epitaxial Fabry-Perot resonator with AlGaAs/AlAs quarter-wave high reflectors and AlGaAs/GaAs multiple quantum wells," *Appl. Phys. Lett.*, vol. 50, pp. 1225-1227, 1987.
- <sup>27</sup> F. Koyarna, S. Kinoshita, and K. Iga, "Room temperature CW operation of GaAs vertical cavity surface emitting laser," *Trans. IEICE*, vol. E71, pp. 1089-1090, 1988.
- <sup>28</sup> J. M. Dallesasse, N. Holonyak, Jr., A. R. Sugg, T. A. Richard, and N. El-Zein, "Hydrolyzation oxidation of  $\text{Al}_x\text{Ga}_{1-x}\text{As}$ -AlAs-GaAs quantum well heterostructures and superlattices," *Appl. Phys. Lett.*, vol. 57, pp. 2844-2846. 1990.
- <sup>29</sup> D. L. Huffaker, D. G Deppe, K. Kumar, and T. J. Rogers, "Native-oxide defined ring contact for low threshold vertical-cavity lasers," *Appl. Phys. Lett.*, vol. 65, pp. 97-99, 1994.

- 
- <sup>30</sup> Y. Hayashi, T. Mukaiharu, N. Hatori, N. Ohnoki, A. Matsutani, F. Koyama, and K. Iga, "Record low-threshold index-guided GaInAs/AlGaAs vertical-cavity surface-emitting laser with a native oxide confinement structure," *Electron. Lett.*, vol. 31, pp. 560-562, 1995.
- <sup>31</sup> G. M. Yang, M. H. McDougal, and P. D. Dupkus, "Ultra-low threshold VCSELs fabricated by selective oxidation from all epitaxial structure," *CLEO'95*, Baltimore, Maryland, May 21-25, paper CPD4-1, 1995.
- <sup>32</sup> K. L. Lear, K. D. Choquette, R. P. Schneider, S. P. Kilcoyne, and K. M. Geib, "Selectively oxidized vertical cavity surface emitting lasers with 50% power conversion efficiency," *Electron. Lett.*, vol. 31, pp. 208-209, 1995.
- <sup>33</sup> R. Jäger, M. Grabherr, C. Jung, R. Michalzik, G. reiner, B. Weigel, and K. J. Ebeling, "57% wall-plug efficiency oxide-confined 850nm wavelength GaAs VCSELs," *Electron. Lett.*, vol. 33, pp. 300-301, 1997.
- <sup>34</sup> K. L. Lear, M. Ochiai, V. M. Hietala, H. Q. Hou, B. E. Hammons, J. J. banas, and J. A. Nevers, "High-speed vertical cavity surface emitting lasers," *LEOS Summer Topical Meeting*, WA-1, Montreal, Canada, 1997.
- <sup>35</sup> C. Jung, R. Jäger, M. Grabherr, P. Schnitzer, R. Michalzik, B. weigel, S. Müller and K. J. Ebeling, "4.8 mW single mode oxide confined top-surface emitting vertical-cavity laser diodes," *Electron. Lett.*, vol. 33, pp. 1790-1791, 1997.
- <sup>36</sup> J. J. Dudley, M. Ishikawa, D. 1. Babic, B. I. Miller, R. Mirin, W. B. Jiang, J. E. Bowers, and E. L. Hu, "144°C operation of 1.3  $\mu$ m GaInAsP vertical cavity lasers on GaAs substrate," *Appl. Phys. Lett.*, vol. 61, pp. 3095-3097, 1992.
- <sup>37</sup> J. J. Dudley, D. 1. Babic, R. Mirin, L. Yang, B. 1. Miller, R. J. Ram, T. Reynold, E. L. Hu, and J. E. Bowers, "Low threshold wafer fused long wavelength vertical cavity lasers," *Appl. Phys. Lett.*, vol. 64, pp. 1463-1465, 1994.
- <sup>38</sup> N. M. Margalit, D. 1. Babic, K. Streubel, R. P. Mirin, R. L. Naone, J. E. Bowers, and E. L. Hu, "Sub-milliamp long wavelength vertical cavity lasers," *Electron. Lett.*, vol. 32, pp. 1675-1677, 1996.
- <sup>39</sup> O. Blum, J. F. Klein, K. L. Lear, G. A. Vawter, and S.R. Kurtz, "Optically pumped, monolithic, all-epitaxial 1.56 $\mu$ m vertical cavity surface emitting laser using Sb-based reflectors," *Electron. Lett.*, vol. 33, pp. 1878-1880, 1997.
- <sup>40</sup> J. Boucart, C. Starck, A. Plais, E. Derouin, C. Fortin, F. Gaborit, A. Pinquier, L. Goldstein, D. Carpentier and J. Jacquet, "RT pulsed operation of metamorphic VCSEL at 1.55 $\mu$ m," *Electron. Lett.*, vol. 34, pp. 1508-1509, 1998.
- <sup>41</sup> H. Shoji, Y. Nakata, K. Mukai, Y. Sugiyama, M. Sugawara, N. Yokoyama, and H. Ishikawa, "Room temperature CW operation at the ground state of self-formed quantum dot lasers with multi-stacked dot layer," *Electron. Lett.*, vol. 32, pp. 2200-2202, 1994.

- 
- <sup>42</sup> H. Sato, K. Nishi, I. Ogura, S. Sugou, and Y. Sugimoto, "Room-temperature lasing of a quantum-dot vertical-cavity surface emitting laser," *Appl. Phys. Lett.*, vol. 69, pp. 3140-3142, 1996.
- <sup>43</sup> D. Huffaker, O. Bakienov, L. A. Graham, B. G. Streetman, and D. G. Deppe, "Quantum dot vertical-cavity surface-emitting laser with a dielectric aperture," *Appl. Phys. Lett.*, vol. 70, pp. 2356-2358, 1997.
- <sup>44</sup> M. Asada, and Y. Suematsu, *IEEE, Journ. of Quant. Elect.*, vol. 21, pp. 434, 1985.
- <sup>45</sup> M. Yamada, T. Anan, K. Kurihara, K. Nishi, K. Tokutome, A. Karrei, and S. Sugou, "Room temperature low-threshold CW operation of 1.23  $\mu\text{m}$  GaAsSb VCSELS on GaAs substrates," *Electron. Lett.*, vol. 36, pp. 637-638, 2000.
- <sup>46</sup> M. Yamada, T. Anan, K. Tokutome, A. Kamei, K. Nishi, and S. Sugou, "Low-Threshold Operation of 1.3  $\mu\text{m}$  GaAsSb Quantum-Well Lasers Directly Grown on GaAs Substrates," *IEEE Photon. Tech. Lett.*, vol. 12, pp. 774-776, 2000.
- <sup>47</sup> M. Kondow, T. Kitatani, S. Nakatsuka, M. C. Larson, K. Nakahara, Y. Yazawa, M. Okai and K. Uomi, "GaInNAs: A novel material for long wavelength semiconductor lasers," *IEEE J. Select. Topics Quantum Electron.*, vol. 3, pp. 719-730, June 1997.
- <sup>48</sup> H. Ho and G. B. Stringfellow, *Mat. Res. Soc. Symp. Proc* Vol. 449, 1997.
- <sup>49</sup> M. Sato and M. Weyers, "GaAsN Alloys: Growth and optical properties," *The 19th Int. Symp. GaAs and Related Compound Semiconductors*, Karuizawa, Japan, 1992; also in *Inst. Phys. Conf Ser.* Philadelphia, PA: Inst. of Physics, Ltd., 1993, vol. 129, pp. 555-560; also in M. Weyers, M. Sato, and H. Ando, *Jpn. J. Appl. Phys.* I 31, L853, 1992.
- <sup>50</sup> M. Weyer and M. Sato, "Growth of GaAsN alloys by low-pressure metal organic chemical vapor deposition using plasma-cracked  $\text{NH}_3$ ," *Appl. Phys. Lett.* Vol. 62, pp. 1396-1398, 1993.
- <sup>51</sup> S. Sakai and T. Abe, "Band lineup of nitride-alloy heterostructures," *The 41<sup>st</sup> Autumn Meeting of Japan Society of Applied Physics and Related Societies*, 28p-X-6, Tokyo, Mar. 1994, S. Sakai, Y. Ueta, and Y. Terauchi, "Band gap energy and band lineup of III-V alloy semiconductors incorporating nitrogen and boron," *Jpn. J. Appl. Phys.*, vol. 32, pp. 4413-4417, 1993.
- <sup>52</sup> J. A. Van Vechten, *Phys Rev.* vol. 187, pp. 1007, 1969.
- <sup>53</sup> J. C. Phillips, "Bonds and Bands in semiconductor," pp. 54, Academic Press Network, 1973.
- <sup>54</sup> M. Kondow and K. Uomi, *1st Pacific Rim Conf. Laser and Electro-Optics*, Chiba, pp. 48, 1995.
- <sup>55</sup> M. Kondow, K. Uomi, A. Niwa, T. Kitatani, S. Watahiki, and Y. Yazawa, "A novel material of GaInNAs for long-wavelength-range laser diodes with excellent high-temperature performance," *Proc. 1995 Solid State Device and Mater.*, pp. 1016-1018, Osaka, Japan, 1995.

- 
- <sup>56</sup> M. Kondow, K. Uomi, A. Niwa, T. Kitatani, S. Watahiki, and Y. Yazawa, "GaInNAs: A novel material for long-wavelength-range laser diodes with excellent high-temperature performance," *Jpn. J. Appl. Phys.*, vol. 35, pp. 1273-1275, Feb. 1996.
- <sup>57</sup> K. Iga, "Vertical cavity surface emitting lasers based on InP and related compounds--bottleneck and corkscrew," *Conf. Indium Phosphide and Related Materials*, ThA 1-1, Apr. 1996.
- <sup>58</sup> A. Cho, "Film Deposition by Molecular Beam Techniques," *J. Vac. Sci. Tech.*, vol. 8, pp.S31-S38, 1971.
- <sup>59</sup> A. Cho, J. Arthur, "Molecular Beam Epitaxy," *Prog. Solid-State Chem.*, vol. 10, pp. 157-192, 1975.
- <sup>60</sup> G. Turner, B. Nechay, S. Eglash, "Frequency-Domain Analysis of Time Dependent Reflection High-Energy Electron Diffraction Intensity Data," *J. Vac. Sci. Tech. B*, vol. 8, pp. 283-287, 1990.
- <sup>61</sup> R. Fernandez, A. Harwitt, D. Kinell, "Accurate Measurements of Transients and Intentional Rates of Change in Molecular Beam Epitaxy Growth Rate Calibrations," *J. Vac. Sci. Tech. B*, vol. 12, no. 2, pp.1023-1025, 1994.
- <sup>62</sup> T. Mattord, K. Sadra, A. Srinivasan, A. Tang, T. Block, Y. Shih, D. Neikirk, B. Streetman, "Real-Time Flux Monitoring and Feedback Control of a valved Arsenic Source," *J. Vac. Sci. and Tech. B*, vol. 11, no. 3, pp. 1050-1052, 1993.
- <sup>63</sup> Applied EPI, Valved Arsenic cracker manual.
- <sup>64</sup> C. T. Foxon, "MBE Growth of GaAs and III-V alloys," *J. Vac. Sci. and Tech. B*, vol. 1, no. 2, pp.293-297, 1983.
- <sup>65</sup> V. Kirchner, H. Heinke, U. Birkle, S. Einfeldt, D. Hommel, H. Selke, and P. L. Ryder, "Ion induced crystal damage during plasma-assisted MBE growth of GaN layers," *Phys. Rev. B*, vol. 58, p 15749-15755, 1998
- <sup>66</sup> V. Gambin, W. Ha, M. Wistey, S. Bank, H. Yuen, S. Kim, J. Harris, "High intensity 1.3-1.6mm luminescence from MBE Grown GaInNAsSb," MRS San Francisco, Spring 2002.
- <sup>67</sup> Sylvia Spruytte, Ph.D. Thesis, Stanford University, 2001
- <sup>68</sup> R. M. Park, "Low-resistivity p-type ZnSe:N grown by molecular beam epitaxy using a nitrogen free-radical source," *J. Vac. Sci. Technol. A*, vol. 10, pp. 701-704, 1992.
- <sup>69</sup> J. Harris, B. Joyce, P. Dobson, "Oscillations in the Surface Structure of Zn-Doped GaAs during Growth by MBE," *Surf. Sci.*, vol. 103, pp.L90-L96, 1981.
- <sup>70</sup> M. Ohring, *The Material Science of Thin Films*, Academic Press, 1992.
- <sup>71</sup> J. Neave, B. Joyce, P. Dobson, N. Norton, "Dynamics of Film Growth of GaAs by MBE from RHEED Observations," *Appl. Phys. A*, vol. 31, pp.1-8, 1983.

- 
- <sup>72</sup> P. Cohen, P. Pukite, J. van Hove, C. Lent, "Reflection High Energy Electron Diffraction Studies of Epitaxial Growth on Semiconductor Surfaces," *J. Vac. Sci. Tech. B*, vol. 3, pp. 1251-1258, 1986.
- <sup>73</sup> T. Block, K. Eyink, D. Neikirk, B. Streetman, "Diffraction Condition Dependence of RHEED Dampening During MBE Growth," *SPIE Proceedings, Epitaxial Growth Processes*, vol. 2140, pp. 10-24, 1994.
- <sup>74</sup> J. van der Wagt, J. Harris, "Reflection High Energy Electron Diffraction Intensity Oscillations during Molecular Beam Epitaxy on Rotating Substrates," *J. Vac. Sci. Tech. B*, vol. 12, no. 2, pp. 1236-1238, 1994.
- <sup>75</sup> R. Sacks, R. Sieg, S Ringel, "Investigation of the Accuracy of Pyrometric Interferometry in Determining  $\text{Al}_x\text{Ga}_{1-x}\text{As}$  Growth Rates and Compositions," *J. Vac. Sci. Tech. B*, vol. 12, no. 3, pp.2157-2162, 1996.
- <sup>76</sup> P. Pinsukanjana, A. Jackson, J. Tofte, K. Maranowski, S. Campbell, J. English, S. Chalmers, L. Coldren, A. Gossard, "Real-time Simultaneous Optical-Based Flux Monitoring of Al, Ga, and In using Atomic Absorption for Molecular Beam Epitaxy," *J. Vac. Sci. Tech. B*, vol. 14, no. 3, pp.2147-2150, 1996.
- <sup>77</sup> W. Gilmore III, D. Aspnes, "Performance Capabilities of Reflectometers and Ellipsometers for Compositional Analysis During  $\text{Al}_x\text{Ga}_{1-x}\text{As}$  Epitaxy," *Appl. Phys. Lett.*, vol. 66, no. 13, pp.1617-1619, 1995.
- <sup>78</sup> C. Kuo, M Boonzaayer, D. Schreder, G. Maracas, B. Jons, "Real Time *in-situ* Thickness Control of Fabry-Perot Cavities in MBE by 88 Wavelength Ellipsometry," *Ninth International Conference on Molecular Beam Epitaxy*, Malibu, CA, 1996.
- <sup>79</sup> W. Breiland, K. Kileen, "A Virtual Interface Method for Extracting Growth Rates and High Temperature Optical Constants from Thin Semiconductor Films using in situ Normal Incidence Reflectance," *J. Appl. Phys.*, vol. 78, no. 11, pp. 6726-6736, 1995.
- <sup>80</sup> G. Li, W. Yuen, K. Toh, L. Eng, S. Lim, C. Chang-Hasnain, "Accurate Molecular Beam Epitaxial growth of Vertical-Cavity Surface Emitting Laser Using Diode Laser Reflectometry," *IEEE Photon. Tech. Lett.*, vol. 7, pp. 971-973, 1995.
- <sup>81</sup> G. Li, W. Yuen, K. Toh, L. Eng, S. Lim, C. Chang-Hasnain, "Accurate Molecular Beam Epitaxial growth of Vertical-Cavity Surface Emitting Laser Using Diode Laser Reflectometry," *IEEE Photon. Tech. Letters*, vol. 7, pp. 971-973, 1995.
- <sup>82</sup> J. Arthur, "Interaction of Ga and  $\text{As}_2$  Molecular Beams with GaAs Surfaces," *J. Appl. Phys.*, vol. 39, pp. 4032-4033, 1968.
- <sup>83</sup> R. Fischer, J. Klem, T. Drummond, R. Thorne, W. Kopp, H. Morkoç, A. Cho, "Incorporation Rates of Gallium and Aluminum on GaAs During Molecular Beam Epitaxy at High Substrate Temperatures," *J. Appl. Phys.*, vol. 54, no. 5, pp. 2508-2510, 1983.

- 
- <sup>84</sup> E. Scott, D. Andrews, G. Davies, "The Influence of Molecular Beam Epitaxy Growth Conditions on the Ga-Al-In-As Ternary and Quaternary Systems," *J. Vac. Sci. Tech. B*, vol. 4, no. 2, pp. 534-535, 1986.
- <sup>85</sup> H. Morkoç, T. Drummond, R. Fischer, "Interfacial Properties of (Al,Ga As)/GaAs Structures: Effect of Substrate Temperature During Growth by Molecular Beam Epitaxy," *J. Appl. Phys.*, vol. 53, pp. 1030-1033, 1982.
- <sup>86</sup> H. Morkoç, T. Drummond, W. Kopp, R. Fischer, "Influence of Substrate Temperature on the Morphology of Al<sub>x</sub>Ga<sub>1-x</sub>As Grown by Molecular Beam Epitaxy," *J. Electrochem. Soc.*, vol. 129, pp. 824-826, 1982.
- <sup>87</sup> G. Metze, A. Calawa, "Effects of Very Low Growth Rates on GaAs Grown by Molecular Beam Epitaxy at Low Substrate Temperatures," *Appl. Phys. Lett.*, vol. 9, no. 1, pp. 818-820, 1983.
- <sup>88</sup> R. Kopf, E. Schubert, T. Harris, R. Becker, "Photoluminescence of GaAs Quantum Wells Grown by Molecular Beam Epitaxy with Growth Interruptions," *Appl. Phys. Lett.*, vol. 58, no. 6, pp. 631-633, 1991.
- <sup>89</sup> A. Madhukar, T. Lee, M. Yen, P. Chen, J. Kim, S. Ghaisas, P. Newman, "Role of Surface Kinetics and Interrupted Growth During Molecular Beam Epitaxial Growth of Normal and Inverted GaAs/AlGaAs (100) Interfaces: A Reflection High-Energy Electron Diffraction Intensity Dynamics Study," *Appl. Phys. Lett.*, vol. 46, no. 12, pp. 1148-1151, 1985.
- <sup>90</sup> Y. Horikoshi, M. Kawashima, H. Yamaguchi, "Migration Enhanced Epitaxy of GaAs and AlGaAs," *Jap. J. Appl. Phys.*, vol. 27, pp. 169-179, 1988.
- <sup>91</sup> N. Chand, S. Chu, "Origin and Improvement of Interface Roughness in AlGaAs/GaAs Heterostructures Grown by Molecular Beam Epitaxy," *Appl. Phys. Lett.*, vol. 57, pp. 1796-1798, 1990.
- <sup>92</sup> Jorg Neugebauer and Chris G. Van de Walle, "Electronic structure and phase stability of GaAs<sub>1-x</sub>N<sub>x</sub> alloy", *Phys. Rev. B.*, vol. 51, no. 16, pp. 10568-10571, 1995.
- <sup>93</sup> G. B. Stringfellow, *Phys Rev.* vol. 187, pp. 1007, 1977.
- <sup>94</sup> *Surface Sci. Lett.* vol. 541, pp. 274, 1992.
- <sup>95</sup> *J. Vac. Sci. Technol.* vol. A12, pp. 1932, 1994.
- <sup>96</sup> M. A. Herman, *Cryst. Res. Technol.* vol. 34, pp. 583-595, 1999.
- <sup>97</sup> W. F. Egelhoff Jr., D. A. Steigerwald, *Journal of Vacuum Science & Technology A (Vacuum, Surfaces, and Films)*, vol. 7, pp. 2167-73, 1989.
- <sup>98</sup> D. A. Steigerwald, I. Jacob, W. F. Egelhoff, Jr., *Surface Science*, vol. 202, pp. 472-92, 1988.
- <sup>99</sup> W. F. Egelhoff Jr., P. J. Chen, C. J. Powell, M. D. Stiles, R. D. McMichael, *Journal of Applied Physics*, vol. 79, pp. 2491-6, 1996.

- 
- <sup>100</sup> B. Poelsema, et al., *Applied Physics A (Solids and Surfaces)*, vol. A53, pp. 369-76, 1991.
- <sup>101</sup> S. Oppo, V. Fiorentini, M. Scheffler, *Physical Review Letters*, vol. 71, pp. 2437-40, 1993.
- <sup>102</sup> V. Fiorentini, S. Oppo, M. Scheffler, *Applied Physics A (Materials Science Processing)*, vol. A60, pp. 399-402, 1995.
- <sup>103</sup> G. Rosenfeld, B. Poelsema, G. Comsa, *Journal of Crystal Growth*, vol. 151, pp. 230-3, 1995.
- <sup>104</sup> B. Voigtlander, A. Zinner, *Surface Science*, vol. 292, pp. 775-80, 1993.
- <sup>105</sup> B. Voigtlander, A. Zinner, *Journal of Vacuum Science & Technology A (Vacuum, Surfaces, and Films)*, vol. 12, pp. 1932-7, 1994.
- <sup>106</sup> B. Voigtlander, A. Zinner, T. Weber, H. P. Bonzel, *Physical Review B (Condensed Matter)*, vol. 51, pp. 7583-91, 1995.
- <sup>107</sup> M. Horn-von Hoegen, *Applied Physics A (Solids and Surfaces)*, vol. A59, pp. 503-15, 1994.
- <sup>108</sup> M. Copel, M. C. Reuter, M. Horn von Hoegen, R. M. Tromp, *Physical Review B (Condensed Matter)*, vol. 42, pp. 11682-9, 1990.
- <sup>109</sup> M. Horn-von Hoegen, M. Pook, A. Al Falou, B. H. Muller, M. Henzler, *Surface Science*, vol. 284, pp. 53-66, 1993.
- <sup>110</sup> M. Horn-von Hoegen, M. Copel, J. C. Tsang, M. C. Reuter, R. M. Tromp, *Physical Review B (Condensed Matter)*, vol. 50, pp. 10811-22, 1994.
- <sup>111</sup> S. C. Wang, G. Ehrlich, *Physical Review Letters*, vol. 67, pp. 2509-12, 1991.
- <sup>112</sup> S. C. Wang, G. Ehrlich, *Physical Review Letters*, vol. 68, pp. 1160-3, 1992.
- <sup>113</sup> S. C. Wang, G. Ehrlich, *Physical Review Letters*, vol. 70, pp. 41-4 1993.
- <sup>114</sup> S. C. Wang, G. Ehrlich, *Physical Review Letters*, vol. 71, pp. 4174-7 1993.
- <sup>115</sup> S. C. Wang, G. Ehrlich, *Physical Review Letters*, vol. 75, pp. 2964-7 1995.
- <sup>116</sup> P. J. Feibelman, *Surface Science*, vol. 299-300, pp. 426-32, 1994.
- <sup>117</sup> I. Markov, *Physical Review B (Condensed Matter)*, vol. 50, pp. 11271-4, 1994.
- <sup>118</sup> I. Markov, *Physical Review B (Condensed Matter)*, vol. 53, pp. 4148-55, 1996.
- <sup>119</sup> I. Markov, *Physical Review B (Condensed Matter)*, vol. 54, pp. 17930-7, 1996.
- <sup>120</sup> G. P. Kothiyal and P. Bhattacharya, *J. Appl. Phys.*, vol. 63, pp. 2760, 1988
- <sup>121</sup> E. H. Li, *Quantum Electron.*, vol. 34, pp. 982, 1998
- <sup>122</sup> S. F. Yu and E. Herbert Li, "Semiconductor lasers using diffused quantum well structures," *J. of Select. Topics Quantum Electron.*, vol. 4, no. 4, p. 723-734, 1998.

- 
- <sup>123</sup> E. V. Rao, A. Ougazzaden, Y. Le Bellego, and M. Juhel, "Optical properties of low band gap GaAs<sub>1-x</sub>N<sub>x</sub> layers: Influence of post-growth treatments", *Appl. Phys. Lett.*, vol. 72, pp. 1409-1411, 1998
- <sup>124</sup> H. P. Xin, K. L. Kavanagh, M. Kondow, and C. W. Tu, "Effects of rapid thermal annealing on GaInNAs/GaAs multiple quantum wells", *J. Cryst. Growth*, vol. 201, pp. 419-422, 1999
- <sup>125</sup> O. M. Khreis, K. P. Homewood and W. P. Gillin, *J. Appl. Phys.*, vol. 84, pp. 232, 1998.
- <sup>126</sup> P. J. Klar, H. Grüning, J. Koch, S. Schäfer, K. Volz, W. Stolz, and W. Heimbrod, A. M. Kamal Saadi, A. Lindsay, and E. P. O'Reilly, "(Ga, In)(N, As)-fine structure of the band gap due to nearest-neighbor configurations of the isovalent nitrogen", *Phys. Rev. B*, vol. 64, no. 15, p. 121203, 2001.
- <sup>127</sup> P. J. Klar, H. Grüning, J. Koch, S. Schäfer, K. Volz, W. Stolz, and W. Heimbrod, "(Ga, In)(N, As)-fine structure of the band gap due to nearest-neighbor configurations of the isovalent nitrogen", *Phys. Rev. B.*, vol. 64, p. 121203, Sep. 2001.
- <sup>128</sup> K. Kim and A. Zunger, "Spatial Correlations in GaInNAs Alloys and their Effects on Band-Gap Enhancement and Electron Localization", *Phys. Rev. Lett.*, vol. 86, p. 2609, 2001.
- <sup>129</sup> S. Kurtz, J. Webb, L. Gedvilas, D. Friedman, J. Geisz, J. Olson, R. King, D. Joslin, and N. Karam, "Structural changes during annealing of GaInNAs", *Appl. Phys. Lett.*, vol. 78, p. 748, 2001.
- <sup>130</sup> S. H. Wei and A. Zunger, "Giant and composition-dependent optical bowing coefficient in GaAsN alloys," *Phys. Rev. Lett.*, vol. 76, pp. 664-667, 1996.
- <sup>131</sup> L. Bellaiche and A. Zunger, *Phys. Rev. B*, vol. 57, pp. 4425, 1998.
- <sup>132</sup> R.K. Willardson and A.C. Beer, "Semiconductors and semimetals vol. 8 Transport and optical phenomena," Academic press (1972), pp. 200-207, 229-238.
- <sup>133</sup> S. L. Chuang, "Physics of optoelectronic devices," John Wiley & Sons Inc., 1995.
- <sup>134</sup> D. A. Miller, "Course Note for EE243," Winter 1998, pp. 64.
- <sup>135</sup> K. T. Faber, and K. J. Malloy, "The mechanical properties of semiconductors, semiconductors, and semimetals Volume 37," Academic press, Inc., pp. 31, 1992.
- <sup>136</sup> J. Neugebauer, and C. G. Van de Walle, "Electronic structure and phase stability of GaAs<sub>1-x</sub>N<sub>x</sub> alloys", *Phys. Rev. B*, vol. 51, pp. 10568-10571, 1995,
- <sup>137</sup> P. F. Fewster and C. J. Curling, "Composition and lattice-mismatch measurements of thin semiconductor layers by x-ray diffraction", *J. Appl. Phys.*, vol. 62, pp. 4154-4158, 1987.
- <sup>138</sup> B. G. Yacobi and D. B. Holt: *J. Appl. Phys.*, vol. 59, no. 4, 1986.

- 
- <sup>139</sup> M. Takakura, S. Notoya, H. Takahashi, *Application note for Cathodoluminescence*, Electron Optics Division, JEOL Ltd.
- <sup>140</sup> C. Trager-Cowan et al., *Mat. Res. Soc. Symp. Proc.*, vol. 482, pp. 715, 1998.
- <sup>141</sup> Peter S. Zory, Jr. "Quantum Well Lasers," *Academic Press*, 1993.
- <sup>142</sup> O. Madelung, "Semiconductors group IV elements and III-V Compounds," *Springer*, 1991.
- <sup>143</sup> J.P. Reithmeier, R. Höger, H. Reichert, A. Heberle, G. Abstreiter, G. Weimann, "Band Offset in Elastically Strained GaInAs/GaAs Multiple Quantum Wells Determined by Optical Absorption and Electron Raman Scattering," *Appl. Phys. Lett.*, vol. 56, no. 6, pp. 536538, 1990.
- <sup>144</sup> D. J. Arent, K. Deneffe, C. Van Hoof, J. De Boak, G. Borghs, "Strain Effects and Band Offsets in GaAs/GaInAs Strained Layer Quantum Structures," *J. Appl. Phys.* vol. 66, no. 4, pp. 17391747, 1991.
- <sup>145</sup> X. Zhang, K. Onabe, Y. Nitta, B. Zhang, S. Fukatsu, Y. Shiraki, R. Ito, "Dependence of Band Offset on Elastic Strain in GaAs/GaAs<sub>1-x</sub>P<sub>x</sub> Strained-Layer Single Quantum Wells," *Jpn. J. Appl. Phys.*, vol. 30, no. 9B, pp. 1631-1634, 1991.
- <sup>146</sup> J. W. Matthews, A. E. Blakeslee, "Defects in Epitaxial Multilayers I," *J. Cryst. Growth*, vol. 27, pp. 118-125, 1974.
- <sup>147</sup> J. W. Matthews, A. E. Blakeslee, "Defects in Epitaxial Multilayers II," *J. Cryst. Growth*, vol. 29, pp. 273-280, 1975.
- <sup>148</sup> J. W. Matthews, A. E. Blakeslee, "Defects in Epitaxial Multilayers III," *J. Cryst. Growth*, vol. 32, pp. 265-273, 1976.
- <sup>149</sup> L. Bellaiche, S. H. Wei, and A. Zunger, "Localization and percolation in semiconductor alloys: GaAsN vs. GaAsP," *Phys. Rev. B*, vol. 54, pp. 17568-17576, 1996.
- <sup>150</sup> L. Bellaiche, S. H. Wei, and A. Zunger, "Composition dependence of inter-band transition intensities in GaPN, GaAsN, and GaPAs alloys" *Phys. Rev. B*, vol. 56, pp. 10233-10240, 1996.
- <sup>151</sup> C. Kittel, "Introduction to Solid State Physics," 7<sup>th</sup> edition, John Wiley & Sons, 1996.
- <sup>152</sup> S. Miyoshi, and K. Onabe, "Band structure of GaNP, (x=0.25, 0.5, 0.75) ordered alloys: semi-empirical tight binding calculation" *Jpn. J. Appl. Phys.*, vol. 37, pp. 4680-4686, 1998.
- <sup>153</sup> A. F. Wright and J. S. Nelson, *Appl. Phys. Lett.*, vol. 66, pp. 3051, 1995.
- <sup>154</sup> I. Vurgaftman, J. R. Meyer, L. R. Ram-Mohan, "Band parameters for III-V compound semiconductors and their alloys," *Appl. Phys. Rev.*, vol. 89, no. 11, pp. 5816, 2001.
- <sup>155</sup> W. G. Bi, C. W. Tu, *Appl. Phys. Lett.*, vol. 70, pp. 1608, 1997.
- <sup>156</sup> T. Yang, S. Nakajima, S. Sakai, *Jpn. J. Appl. Phys.*, Part 2, vol. 36, L320, 1997.

- 
- <sup>157</sup> J. Klern, D. Huang, H. Morkoc, Y. E. Ihm, N. Otsuka, *Appl. Phys. Lett.*, vol. 50, pp. 1364, 1987.
- <sup>158</sup> N. Bouarissa, N. Amrane, H. Aourag, *Infrared Phys. Tech.*, vol. 36, pp. 755, 1995.
- <sup>159</sup> S. H. Wei, A. Zunger, *Phys. Rev. B*, vol. 52, 12039, 1995.
- <sup>160</sup> S. A. Ding, S. R. Barma, K. Hom, H. Yang, B. Yang, O. Brandt, K. Ploog, "Valence band discontinuity at a cubic GaN/GaAs heterojunction measured by synchrotron-radiation photoemission spectroscopy," *Appl. Phys. Lett.*, vol. 70, pp. 2407-2409, May 1997.
- <sup>161</sup> R.M. Feenstra, J.M. Woodall, and G.D. Pettit, *Phys. Rev. Lett.* vol. **71**, pp. 1176, 1993.
- <sup>162</sup> J. S. Osinski, P. Grodzinski, Y. Zou, and P. D. Dapkus, "Threshold current analysis of compressive strain (0-1.8%) in low threshold, long wavelength quantum well lasers," *IEEE J. Quantum Electron.*, vol. 30, pp. 2245, 1994.
- <sup>163</sup> X. Yang, M. J. Jurkovic, J. B. Heroux, and W. I. Wang, "Molecular beam epitaxial growth of InGa<sub>N</sub>:Sb/GaAs quantum wells for long-wavelength semiconductor lasers," *Appl. Phys. Lett.* vol. 74, pp. 2337, July 1999.
- <sup>164</sup> H. Shimizu, K. Kumada, S. Uchiyama, and A. Kasukawa, "High performance CW 1.26  $\mu$ m GaInNAsSb-single quantum well and 1.2  $\mu$ m GaInAsSb-single quantum well ridge lasers", *Electron. Lett.* vol. 36, pp. 1701, 2000.
- <sup>165</sup> X. Yang, M. J. B. Heroux, and L. F. Mei, and W. I. Wang, "GaInAsNSb/GaAs quantum wells for 1.55  $\mu$ m lasers grown by molecular-beam epitaxy," *Appl. Phys. Lett.* vol. 78, pp. 4068, 2001.